BEHAVIOR OF LIQUID BRIGES BETWEEN NONPARALLEL SURFACES

MOHAMMADMEHDI ATAEI

A THESIS SUBMITTED TO
THE FACULTY OF GRADUATE STUDIES
IN PARTIAL FULFILLMENT OF THE REQUIREMENTS
FOR THE DEGREE OF
MASTER OF APPLIED SCIENCE

GRADUATE PROGRAM IN MECHANICAL ENGINEERING

YORK UNIVERSITY

TORONTO, ONTARIO

SEPTERMBER 2016

Abstract

Formation of liquid bridges between two solid surfaces is frequently observed in industry and nature, e.g. printing. When the two solid surfaces are not parallel (with dihedral angle ψ between them), two significant phenomena emerge in the bridge behavior: First, if ψ exceed a critical angle (ψ_c), the bridge is no longer stable and propel itself horizontally towards the cusp of the surfaces. Second, if a stable bridge is squeezed and stretched, a horizontal bulk motion of the bridge along the surfaces can be observed. Through both experimental and numerical studies, we demonstrated that ψ_c can be increased by increasing advancing contact angle (θ_a), and Contact Angle Hysteresis (CAH) of the surfaces. We also demonstrated that the magnitude of the bulk motion can be increased by increasing ψ, the amount of compressing and stretching, and/or by decreasing θ_a and CAH of the surfaces.

Acknowledgement

I like to express my sincere gratitude to my thesis advisors, Prof. Amirfazli, and Prof. Tang for their consistent support during the last two years and steering me in the right the direction. I could not imagine having better advisors. I will always owe them both a large debt of gratitude for this life-changing experience.

I must express my heartfelt gratitude to my parents and to my fiancé for providing me with consistent support and continuous encouragement throughout my study. This milestone would not have been possible without them. Thank you.

Finally, I thank my fellow lab-mates and friends in Mechanical Dept. of York University for their support during my studies: Huanchen Chen, Hossein Banitabaei, Ruth Milton, Hamed Almohammadi, Aysan Razzaghi, Ningli Chen, Amirhossein Seyedmehdi, Constantine Papakonstantinou and Bola Komolafe.

Table of Contents

List of Tables

List of Figures

Chapter One: Introduction

Drop motion is a process frequently observed in many applications; such as in microfluidics [1], DNA analysis [2], and fog collectors [3]. Generally, drops can be manipulated in different ways e.g., by gravity [4], electric field [5], temperature gradient [6], or by using liquid bridges [7-11]. Among these methods, liquid bridges have been extensively used in many applications to move droplets [7-11]. For example, in offset printing, drop inks are transferred from one surface to another by stretching and breaking a liquid bridge between the two rollers [11]. Many studies have been performed on liquid bridges formed between two parallel surfaces (e.g. see Refs. 9-11). However, when the surfaces are parallel, no bulk motion of the drop along the surfaces can be achieved. On the other hand, when the surfaces are not parallel, the liquid bridge can be moved along the surfaces in two different ways:

a) **Unstable spontaneous motion of the bridge:** If the dihedral angle between the surfaces (ψ) is larger than a critical value (ψ_c) (i.e. $\psi > \psi_c$), the drop spontaneously moves along the surfaces immediately after formation of the bridge (Figure 1.1a), until it reaches to the cusp of the two surfaces (Figure 1.1b).

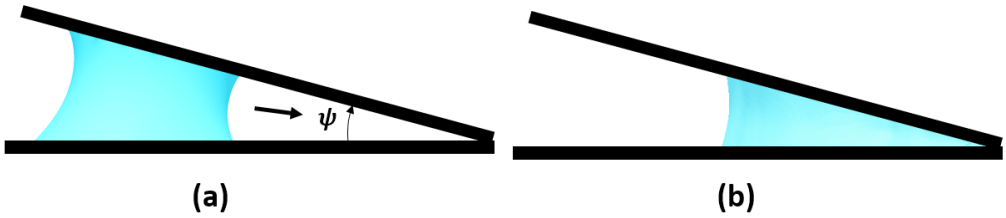

Figure 1.1 Schematics of an unstable liquid bridge moving towards the cusp. a) An unstable liquid bridge moves along the surfaces. b) The movement will continue until the bridge fills the space at the cusp of the surfaces.

b) **Controlled motion of the bridge:**) If $\psi < \psi_c$, the formed liquid bridge remains stable (i.e. without exhibiting any spontaneous motion). Yet, when it is squeezed and stretched between the surfaces, it would move horizontally. For instance, as shown in Figure 1.2, when the bridge is squeezed, it advances towards the cusp on its narrower side, while the wider side remains pinned (see Figure 1.2b). And when the bridge is stretched, the wider side recedes towards the cusp, while the narrower side remains pinned (see Figure 1.2c). Due to the asymmetric spreading/retreating of the contact lines, a horizontal bulk motion of the bridge can be observed. The bridge can undergo consecutive squeezing and stretching cycles (i.e. loading cycles) to achieve desired motion.

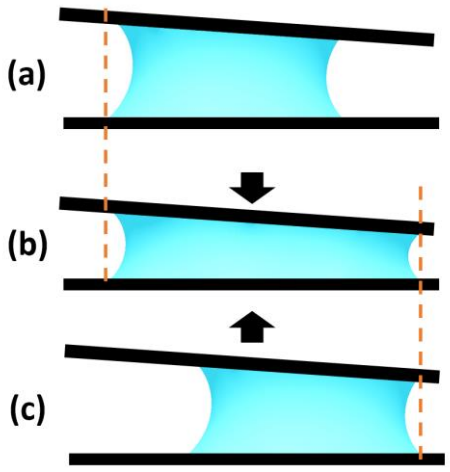

Figure 1.2 Schematics of liquid bridge movement by squeezing and stretching. a) The bridge before compression begins. b) when the bridge is compressed, the narrower side of the bridge advances towards the cusp while the wider side remain pinned. c) When the bridge is stretched, the wider side recede towards the cusp, while the narrower side remains pinned.

The process given in (a) allows one to move the drop effortlessly, but without control over the amount of drop movement. Whereas in the process given in (b), the motion needs actuation, but the amount of drop movement is controllable. These two methods of drop transfer also can be useful where, for example, it is not possible to have temperature gradient or electric field to manipulate droplets along the surfaces e.g. in biological applications.

Several studies were performed to manipulate drops using nonparallel surfaces in industrial applications [3, 12, 13]. For example, a type of plate-based fog collector uses the spontaneous motion of the bridge to collect water drops condensed on its plates (see Figure 1.3a) [3]. Drop motion between nonparallel surfaces also can be seen in nature [8]. For example, Phalarope's feeding mechanism rely on moving prey inside liquid bridges mouthwards, by squeezing and stretching the bridge between their long beaks (see Figure 1.3b) [8].

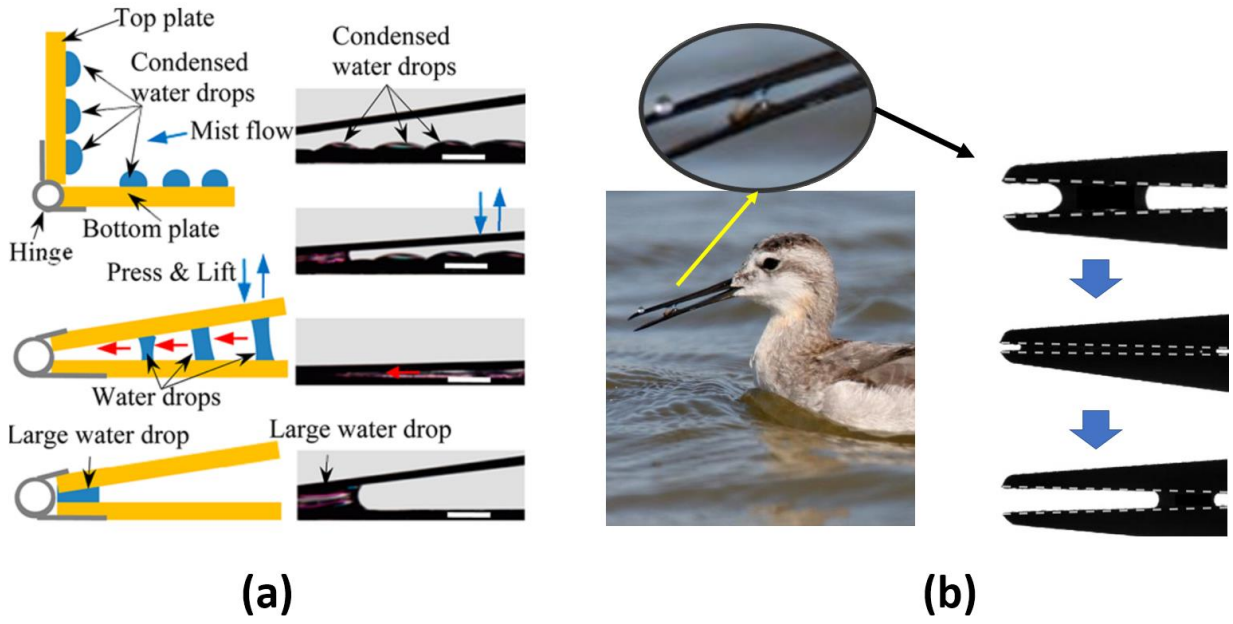

Figure 1.3 a) Process of collecting drops condensed on a fog collector's plates using spontaneous motion of liquid bridges between nonparallel surfaces. (Reprinted with permission from Heng, X. & Luo, C. Bioinspired plate-based fog collectors. ACS Appl. Mater. Interfaces 2014, 6, 16257–16266. Copyright 2016 American Chemical Society. b) Phalaropes uses squeezing and stretching a liquid bridge between their beaks to move preys trapped inside the bridge mouthwards (Images courtesy of John Bush, MIT [8]).

Given the capability of nonparallel surfaces in inducing drop motion, a number of previous studies were done to understand the mechanical characteristics of the phenomenon. Comprehensive literature reviews for the spontaneous and controlled motion of the bridge will be given in Chapters

Two and Three, respectively, as each chapter is organized as a paper for publication. In the next two subsections, a brief literature review on each of the subjects will be presented.

1.1 Literature Review: Spontaneous Motion of the Bridge

Spontaneous motion of the bridge typically occurs when the surfaces are hydrophilic (with contact angle (CA) $< 90°$) [7, 8, 14, 15]. In previous studies done by Concus *et al.* [14, 15], it was reported that the liquid bridge becomes unstable and move spontaneously, if both surfaces are hydrophilic. In these studies, it was assumed that surfaces are ideally smooth and homogeneous, such that the CA (θ) between the liquid and solid is of a single value. Under such a condition, θ can be calculated based on Young's equation:

$$\gamma_{lv} \cos\theta = \gamma_{sv} - \gamma_{sl} \tag{1.1}$$

where γ_{lv}, γ_{sv}, and γ_{sl} are, respectively, surface tensions of liquid-vapor, solid-vapor, and solid-liquid interfaces. However, in practice, due to the surface's roughness and heterogeneity (e.g. contamination), CAs can attain a variety of values as rather than a single one; ranging from a maximal value known as advancing CA (θ_a) to a minimal value, i.e. receding CA (θ_r). The contact line is allowed to move outward, only if $\theta = \theta_a$ (see Figure 1.4a), and is allowed to move inward only if $\theta = \theta_r$ (see Figure 1.4b). When $\theta_r < \theta < \theta_a$, the contact line of the liquid remains pinned to the surface. This phenomenon is known as Contact Angle Hysteresis (CAH) and the magnitude of CAH is defined as the difference between θ_a and θ_r (i.e. $CAH = \theta_a - \theta_r$) [4].

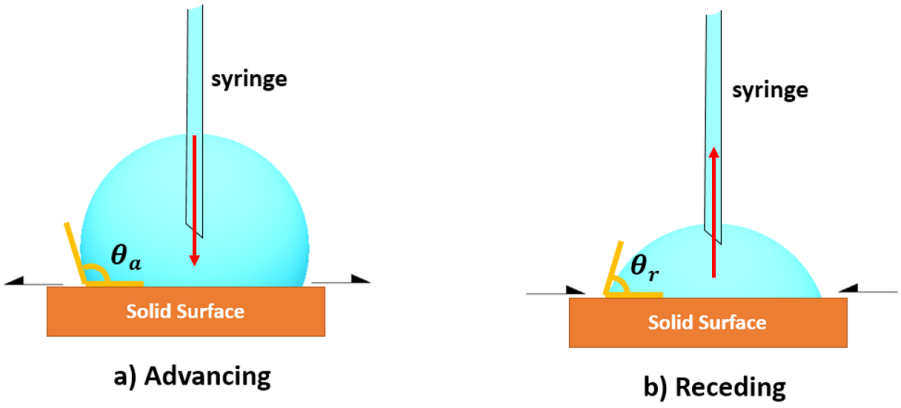

Figure 1.4 Illustrations for advancing contact angle (a) and receding contact angle (b).

While Concus *et al.* [14, 15] predicted instability of bridges between hydrophilic surfaces, without considering CAH, in recent works of Parakash *et al.* [8] and Luo *et al.* [7] it was shown that CAH would allow stabilization of a liquid bridge between two hydrophilic surfaces. The stability of the bridge was possible, only if ψ was less than a critical angle (ψ_c) [7, 8]. However, no systematic understanding of the governing parameters controlling the stability of a liquid bridge exists. As a result, no predictive tool has been provided to calculate ψ_c. In the work of Luo *et al.* [7], CAH was introduced as an upper bound for ψ_c, when the two surfaces are identical and hydrophilic (i.e. $\psi_c < CAH$) [7]. That is, if $\psi > CAH$, the liquid bridge is necessarily unstable. While having $\psi < CAH$ does not guarantee stability of the bridge, in our preliminary work we observed that the real value of ψ_c can be significantly smaller than CAH of surfaces (see Chapter Two), therefore, CAH is not a suitable upper bound for ψ_c. Additionally, the work of Luo *et al.* [7], was limited to only one type of hydrophilic surface, which cannot demonstrate the effect of CA and CAH on the bridge stability in a systematic way.

To enable spontaneous motion of drops using nonparallel surfaces, one should be able to calculate the critical angle of the system. Therefore, a study is required to provide a better evaluation of ψ_c

for different systems. Additionally, ψ_c draws the boundary between the two methods of moving the droplet, thus, knowing its value is necessary to achieve the desired motion.

1.2 Literature Review: Controlled Motion of the Liquid Bridge

Parakash *et al.* [8] highlighted the essential role of CAH on the horizontal motion of the bridge; it allows one side of the bridge to remain pinned by having CAs between θ_a and θ_r, while the other side is advancing (see Figure 1.2b), or receding (see Figure 12c). They designed an experimental setup analogous to Shorebird's beaks (see Figure 1.3b), which squeezed and stretched the bridge as a tweezer-like mechanism [8]. The motion was considered to be efficient, if the pinning during the movement occurred asymmetrically [8], that is, if the bridge is not advancing on the wider side during squeezing, and is not receding on the narrower side during stretching. Such asymmetric depinning prevents the liquid from regressing away from the cusp and uses the energy given to the liquid to move the bridge only in one direction [8]. Optimal beak opening and closing angles were obtained for the most efficient drop motion [8]. However, the system used was limited to a single model of Phalarope's beak, which could not generally represent all the liquid bridge systems with nonparallel surfaces. Another study by Wang *et al.* [16] was performed to further study the efficient drop motion. Instead of smooth surfaces, they hypothesized that using surfaces with lopsided saw-tooth structures would prevent the backward motion of the bridge. However, saw-tooth surfaces could not prevent the backwards motion when surfaces were hydrophilic [16]; the bridge motion towards the cusp was obstructed by the adsorption of liquid inside the saw-tooth cavities [16]. In another study, Luo *et al.* [7] provided a theoretical model that showed the traveled distance in one loading cycle increases, as the bridge gets closer to the cusp of surfaces after each loading cycle. Though, this conclusion appears to be in contradiction with Parakash *et al.* [8] experimental results, while no information on the cause of discrepancy was provided.

To enable this method of drop transfer in practical situations, several shortcomings in the literature needs to be addressed. First, no study has done a systematic work to fully understand the governing parameters controlling the motion of the bridge. Second, the reported results are for specific situations which are not applicable in many applications e.g., the results from Luo *et al.* [7] is valid only when using specific volumes of liquid, and the results from Parakash *et al.* [8] only works for Phalarope's beak model. And third, it is still unclear how one can achieve asymmetric depinning during the movement in a simple and general manner. Based on the discussion above, a systematic study of parameters affecting horizontal movement is needed, so that the bridge motion can be controlled as desired.

1.3 Knowledge Gap and Thesis Objectives

Due to the limitations in the literature, a comprehensive study on the drop motion using nonparallel surfaces is needed. Particularly, this thesis will focus on answering the following five questions to improve the understanding of the subject:

On the stability of the bridge:

1. What is the role of CA and CAH on the stability of the liquid bridge?

2. Based on the effects of physical parameters on the bridge stability, is it possible to predict the value of ψ_c only by knowing the specifications of the system?

On the motion of the bridge by compressing and stretching:

3. What parameters control the horizontal motion of the bridge in loading cycles? And how they affect the motion?

4. How can one achieve asymmetric depinning to enhance the motion?

5. What causes the inconsistent results in the literature [7, 8] about the behavior of a bridge when it undergoes sequential loading cycles?

1.4 Thesis Scope

In this thesis, we used experimental, analytical, and numerical approaches to answer the above questions based on the following scope:

- This thesis only studies the systems under quasi-static condition, where *Weber* number is sufficiently small for the effect of viscosity to be negligible.
- Only liquid drops with small volume (order of microliters) were considered. Systems with such small volumes of drops have small *Bond* number, and therefore the effect of gravity can be neglected.
- Only liquid bridges between two identical and hydrophilic surfaces were considered (surfaces with $\theta_a \leq 90°$ and $CAH \leq 90°$).

1.5 Thesis Outline

This paper is organized based on two papers: A version of Chapter Two has been submitted to Langmuir (ACS) publications and is currently under review, and a version of Chapter Three will be submitted in near future for publication. In Chapter two, an experimental, theoretical, and numerical study on stability of a liquid bridge between nonparallel surfaces will be provided. In this chapter, an empirical equation to calculate ψ_c of different systems will be proposed and validated. The supplementary information (SI) of this chapter can be found in Appendix A. In Chapter three, the mechanism of the bridge motion by squeezing and stretching is discussed. A comprehensive study was performed to understand the effect of governing parameters on the motion of the liquid bridge. SI of Chapter Three can be found in Appendix B. Conclusions and

future perspectives will be provided in Chapter four. Following Chapter Four, bibliography, simulations sample code (Appendix C), and details of the experimental process (Appendix D) will be provided, respectively.

Chapter Two: Stability of Liquid Bridges between Nonparallel Surfaces[1]

2.1 Introduction

Liquid bridges formed between two solid surfaces are commonly observed in many industries. For example, during offset printing, ink is transferred between rollers by stretching and breaking the ink bridges [9-11]. The stability of the liquid bridges has been the focus of various studies in the literature [17-19]. However, most of these studies mainly focused on axisymmetric liquid bridges between two parallel surfaces. In practice, liquid bridges also can be formed between nonparallel surfaces. For example, phalarope shorebirds trap preys inside liquid bridges formed between their nonparallel beaks [8]. When the two surfaces are not parallel (with a dihedral angle ψ between them) an instability may appear, i.e. the bridge may propel itself towards the most confined region (Figure 2.1a), and this motion can be continued (Figure 2.1b) until the liquid fills the space between the surfaces at the cusp of the two surfaces (Figure 2.1c) [7]. Such instability brings the opportunity to propel a drop spontaneously between two nonparallel surfaces, which can be used in many applications. For example, it can be applied to harvest condensed water drops [3], or generate drops in microfluidics systems [1] or to generate desired drop sizes [12].

[1] Chapter Two of this thesis has been submitted as M. Ataei, H. Chen, T. Tang and A. Amirfazli, "Stability of Liquid Bridges between Nonparallel Hydrophilic Surfaces" to Langmuir (ACS publications).

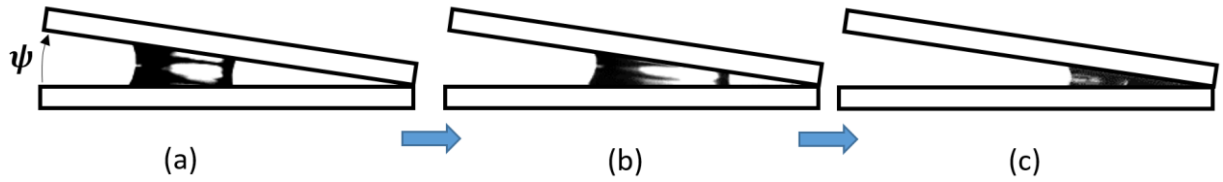

Figure 2.1 A liquid bridge between nonparallel surfaces can spontaneously move toward the most confined region. a) Bridge starts to move towards the cusp. b) Bridge continues its movement until it reaches the surfaces' cusp. c) The liquid creates a liquid blob at the cusp of the surfaces.

This self-propelled motion is usually observed for liquid bridges formed between nonparallel hydrophilic surfaces (with contact angle (CA) $< 90°$), but the underlying physical basis of such instability is not well understood. In previous studies [14, 15], an inequality for CA was proposed to predict whether the bridge experiences this instability or not. According to this inequality, the bridge is always unstable between two hydrophilic surfaces whether they are identical or different. This conclusion was derived from the assumption that the CA (θ) between the liquid and each solid has a single value. The constant θ forces the bridge to meet the surfaces with a different curvatures on its narrow and wide ends, causing the Laplace pressure to be different at the two ends, which in turn propels the bridge toward the cusp. However, in reality, CA between a liquid and a surface is not a constant, but takes a range of values. The upper and lower bounds of this range are known as advancing CA (θ_a) and receding CA (θ_r), respectively. The difference between θ_a and θ_r is called the Contact Angle Hysteresis (*CAH*) [4]. The presence of *CAH* can allow the bridge to maintain the Laplace pressure balance by obtaining different CAs on its narrow and wide ends [7, 8]. In fact, a stable bridge has been observed to exist between two nonparallel hydrophilic surfaces due to the effect of *CAH* [7, 8].

Despite the observed stability introduced by *CAH*, no study has been performed to investigate the effect of CA and CAH on the bridge stability in a systematic way. For example, in a recent study,

Luo *et al.* [7] proposed that between two hydrophilic surfaces, a stable bridge is not possible if $\psi > CAH$, but possible, if $\psi < CAH$. The conclusion was supported by four experiments which shared the same type of surface and liquid but differed by the drop volume and ψ. Because only one type of hydrophilic surface was used, this work was not yet able to provide a clear understanding regarding the effect of CA and CAH on the droplet stability.

Another limitation of the past studies is that they [7, 8, 12-15] have all used a 2D model to investigate the stability of the liquid bridge. Despite the mathematical convenience, such a model cannot capture many properties of a bridge that is naturally a 3D system; i.e. the shape of the contact lines, distribution of CA along the contact line, and the value of Laplace pressure. These properties are directly influenced by CAs and CAH. As such, to comprehensively understand the effect of CAs and CAH on bridge stability, a 3D model is needed.

In accordance to the objectives of the thesis (see Objectives 1-2 in Section 1.3), this chapter aims to provide answers to the following questions through experiments, numerical simulations, and theoretical reasoning,: How is the stability of the liquid bridge affected by the ψ, the CAs and the *CAH* of the surfaces? And what is the underlying mechanisms for the dependence on these variables? Answering these questions will help us to have a clear understanding of the governing parameters affecting the bridge stability and provide a predictive model for bridge stability. Here, we focus on liquid bridges formed between two identical hydrophilic (with $\theta_a < 90°$) nonparallel surfaces. The effect of CA and *CAH* on the stability of the liquid bridge is elucidated by using a wide range of hydrophilic surfaces with different θ_a and CAH. In addition, we use Surface Evolver to provide detailed information about the 3D shape of the liquid bridge (e.g. Laplace pressure, distribution of the CA, etc.), and to augment the number of systems studied through experiments.

2.2 Methods

2.2.1 Experimental

The experimental process is schematically depicted in Figure 2.2. First, a liquid drop was deposited on the bottom surface in a way that the initial contact angle (θ_{ini}) was close to θ_a of the surface. Then, the tilted top surface was moved down towards the drop at low speed ($0.005mm/s$) and stopped at the moment it touched the drop. If a stable liquid bridge was able to form (i.e. no spontaneous horizontal movement after the formation), the dihedral angle (ψ) was increased by $0.2°$ increment and the experiment was repeated. The ψ value was changed until at a certain dihedral angle the bridge became unstable by moving towards the cusp of the surfaces. That angle was noted as the critical angle, and denoted as ψ_c. The experiments at ψ_c was then repeated for four more times. If the bridge was unstable in at least three of the four experiments, the ψ_c value was considered as the critical angle, otherwise, the dihedral angle was increased by $0.2°$ again and the experiment was repeated for the new value. In each test $2\ \mu L$ distilled water drop was used, and all the experiments were performed at approximately $21°C$. Two perpendicular cameras (Phantom Miro M310 and Photon Focus DR1-D1312) were used to monitor the stability by recording the process with a resolution of 800x600 pixels and 30 fps. One camera view was faced toward ψ angle and referred to as side view, and the other was perpendicular to the side view camera referred to as front view (Figure 2.3). The bottom surface remained static during the experiments. Vertical motion of the top surface was provided by ILS100CC and XPS-C6 Motion Controllers from Newport as shown in Figure 2.3, which is capable of moving the top surface at very low speeds (minimum of $1x10^{-6}m/s$). The top surface was connected to a tilting stage capable of tilting the surface with a resolution of $0.2°$, up to $22.5°$, and the entire top stage was

connected to a leveling platform to ensure that the surface was only tilted in one direction. More details on the experimental process are given in Appendix D.

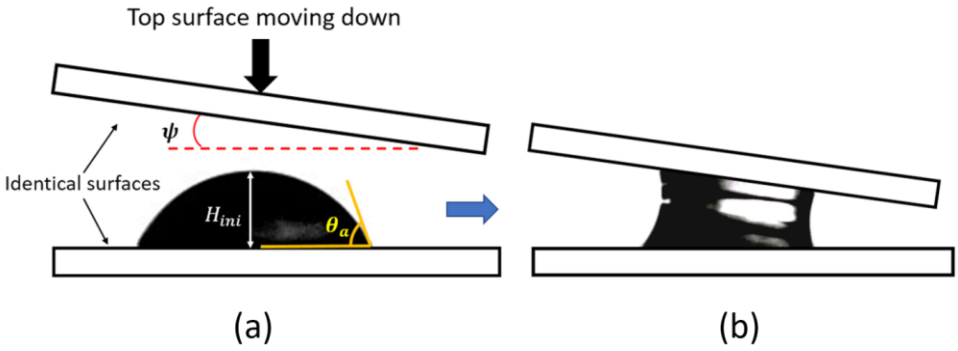

Figure 2.2 Experimental process (from side view). a) The drop was placed on the bottom surface, and an identical tilted surface was moved down; b) the movement of the top surface was stopped the moment the bridge was formed.

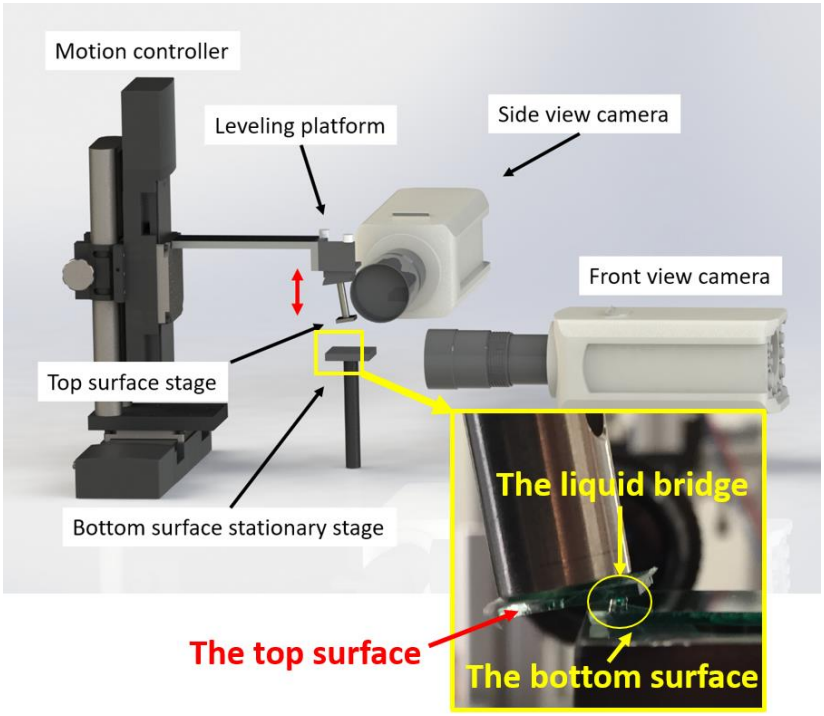

Figure 2.3 Experimental setup. A motion controller was used for moving the top surface, the tilting stage is able to tilt the surface with 0.2° increments, up to 22° degrees. Two perpendicular cameras monitor the stability of the liquid bridge. The inset picture shows how the surfaces were mounted in the experimental process.

Several surfaces with different wettabilities were fabricated as shown in Table 1. For fabricating the surfaces, poly(methyl methacrylate) (PMMA), polystyrene (PS), poly(ethyl methacrylate) (PEMA), and silicon were used. Spin coating was used as the fabrication method based on Chen *et al*. [20]. The values of θ_a and *CAH* were measured using the sessile drop method [21]. Detailed information about the fabrication procedure is given in Appendix Section A.1. In each experiment, the top and bottom surfaces were of the same type (e.g. both were silicon), therefore, their wettability was identical. As shown in Table 1, PMMA (2), PEMA, PS surfaces have a similar *CAH*, but different θ_a . PMMA (1) and PMMA (2) have similar θ_a but different *CAH*. Therefore, these surfaces allow us to address the effect of θ_a and *CAH* separately.

Table 2.1 Wettability parameters for the surfaces used in experiments with distilled water. The CAs were measured using the sessile drop method and the ImageJ open software. Measurements was repeated for nine times for each surface.

Case#	Surfaces	θ_a	*CAH*
1	Silicon	**45.2°±1.2°**	**22.6°±2.5°**
2	PMMA (1)	**72.4°±1.4°**	**15.4°±1.1°**
3	PMMA (2)	**72.7°±1.4°**	**11.1°±1.9°**
4	PEMA	**78.8°±0.3°**	**10.5°±0.5°**
5	PS	**89.6°±1.0°**	**10.7°±1.2°**

2.2.2 Simulation

Surface Evolver seeks an equilibrium geometry of a surface by minimizing the surface energy subjected to constraints [22, 23]; it has been used in many investigations to study the stability of liquid surfaces, e.g. see refs. 24-25. In Surface Evolver, the user describes an initial surface along with different constraints and conditions (e.g. surfaces, CAs, presence/absence of gravitational energy, surface tension, etc.) and the program evolves the surface towards the minimum energy by Gradient Descent Method [22, 23]. However, *CAH* is not considered in Surface Evolver as a natural constraint. A few methods are available to implement *CAH* in Surface Evolver [26, 27]. Here, a friction model based on Santos *et al.* [27] was used to implement *CAH*. In this method, a frictional force is applied on the contact line to keep it pinned when the contact angle is within the receding and advancing CA interval; the contact line is allowed to move when the contact angle reaches any of the boundary values.

Normally, earlier shapes of the liquid may not matter in finding the final equilibrium shape. However, in the presence of *CAH*, the equilibrium values of CAs and the location of contact lines are dependent on their evolution history during the dynamic process when the bridge is being formed. Using the Phantom camera at a high frame rate (35,000 fps) we observed that during this dynamic process, the liquid expanded on the top surface, while at the same time it shrank on the bottom surface. Since Surface Evolver is based on energy minimization, it can only predict the geometry of the final equilibrium bridge (if it exists), but it cannot simulate the dynamic process at the start of the bridge formation. To best mimic such an evolution history, the initial drop shape assigned at the beginning of the Surface Evolver minimization process had an asymmetric shape with smaller contact area on the top surface, and a larger contact area on the bottom surface (Figure 2.4a). In addition, θ_a and θ_r were assigned as the initial contact angles on the top and bottom

surfaces, respectively. This initial shape forced Surface Evolver to expand on the top surface (with θ_a) and shrink on bottom surface (with θ_r) at the beginning of the iteration process, which mimicked the process at the beginning of bridge formation (see Figure 2.4). This approach was validated by comparing the CAs and contact area width of the final equilibrium liquid bridge obtained from the experiments (from both camera views) and respected simulations. In addition, direct comparison of the shapes of stable liquid bridge between experiment and Surface evolver was conducted. These validations are presented in Appendix Section A.2 which showed decent agreement.

During the iterations, the uniformity of the mesh was controlled using "Equiangulation (u)" and "Vertex Averaging (V)" functions of Surface Evolver. To find the critical angle, ψ_c, from the simulations, the dihedral angle was increased gradually until at a certain angle (noted as ψ_c) no equilibrium shape could be found from energy minimization. In order to validate the ability of the Surface Evolver model in the prediction of bridge stability, the value of ψ_c obtained from the experiments were compared to identical simulations (see Appendix Section A.3).

An example of the code of the simulation can be found in Appendix Section C.1.

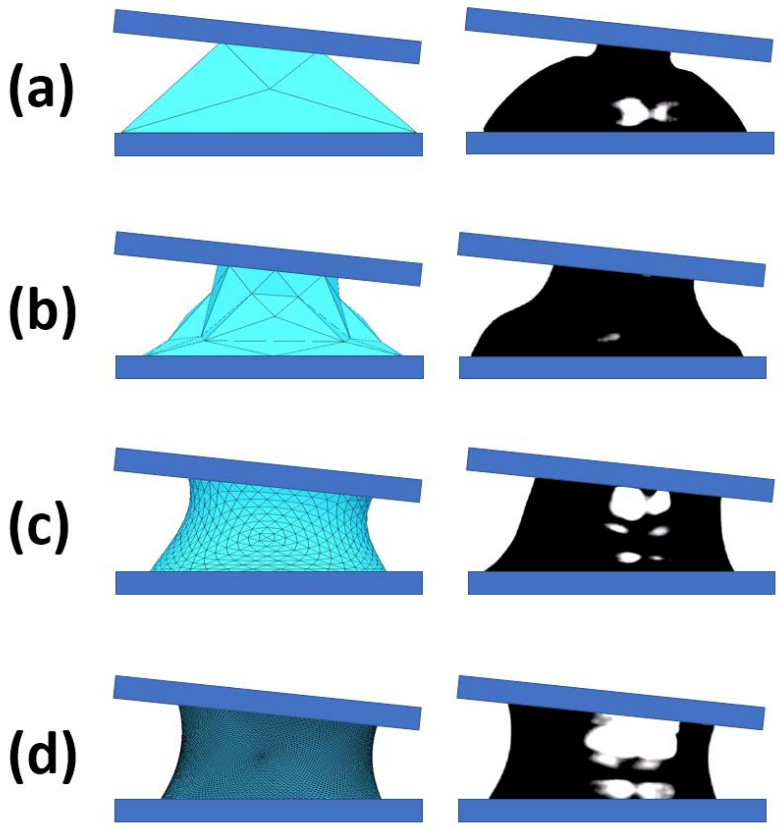

Figure 2.4 Snapshots from a typical Surface Evolver minimization (left panel), along with snapshots of the liquid bridge formation taken from the high-speed camera (right panel) for PMMA (1), $\psi = 6°$: a) Initial configuration. b) The initial shape forced Surface Evolver to mimic the process at the beginning of bridge formation, with contact area expanding on the top surface and shrinking on the bottom surface. c) The surface was continuously refined and evolved towards a minimum surface energy d) The final shape of the bridge was acquired at the end of the iteration process. Strictly speaking, it is incorrect to directly compare the refinement of bridge shape in SE iteration with the bridge formation process, since SE can only predict the final equilibrium shape of the bridge while the bridge formation is a dynamic process.

2.3 Theoretical Considerations

Preliminary stability concepts for liquid bridge will be discussed first from a theoretical perspective. A 3D model of the liquid bridge is considered in discussing the concepts (see Figure 2.5a). For a stable liquid bridge to form, it must be in a mechanical equilibrium state. Two

conditions necessary for the equilibrium of the bridge are: (1) global force balance; and (2) a uniform pressure within the liquid. These two conditions will be employed to explain the relations between ψ, CAs, CAH, and the stability of the bridge. The effect of gravity was considered to be small and neglected since the *Bond* number ($Bo = \rho g L^2/\gamma$) was found to be in the order of 10^{-2} for all of our systems, where L is the characteristic length, taken as the radius of the best fitted circle to the contact area when a stable liquid bridge was formed; and ρ, γ, g are, respectively, the density of the liquid, surface tension, and gravitational acceleration.

2.3.1 Global force balance

Figure 2.5b depicts the external forces acting on the liquid bridge. The pressure acting on the liquid-air interface (S_1) is the ambient pressure (P_∞), which differs from the pressure inside the bridge (P_{inside}) exerted on the solid-liquid interfaces (S_2). The difference between the two pressures is the Laplace pressure (P_L) which, according to the Young-Laplace equation, is given by $P_L = 2\gamma M$, where M is the mean curvature of the liquid-air interface. Laplace pressure was considered to be constant everywhere across S_1 (see detailed discussion in the next subsection). In addition to the pressures, there are surface tension forces (F_γ) along the contact lines (cl) on the liquid-solid interfaces. The outward normal of the interfaces (S_1 and S_2) is denoted as $\mathbf{e_n}$; the outward normal of the contact lines (cl) on S_2 is denoted as $\mathbf{t_n}$, and the contact angle as θ. The global force balance can then be written as:

$$-\int_{S_1} P_\infty \mathbf{e_n} dS - \int_{S_2} P_{inside} \mathbf{e_n}\, dS + \underbrace{\gamma \int_{cl} \cos\theta\, \mathbf{t_n} dl + \gamma \int_{cl} \sin\theta \mathbf{e_n} dl}_{F_\gamma} = 0 \tag{2.1}$$

Surface tension and pressure integrals are taken over differential elements of contact line (dl) and surface (dS), respectively. Replacing P_{inside} with $P_\infty + 2\gamma M$ (Young-Laplace Eqn.), one finds:

$$-\int_{S_1+S_2} P_\infty \mathbf{e_n} dS - 2\gamma \int_{S_2} M\mathbf{e_n}\, dS + \gamma \int_{cl.} \cos\theta\, \mathbf{t_n} dl + \gamma \int_{cl.} \sin\theta \mathbf{e_n} dl = 0 \qquad (2.2)$$

Based on Gauss's theorem, the integration of a constant (P_∞ here) over a closed surface is zero, therefore, the first term of Eqn. (2.2) is zero. Dividing Eqn. (2.2) by γ shows that for a liquid bridge with a given geometry, the global force balance is independent of the surface tension of the liquid, explicitly. However, it should be noted that the surface tension implicitly affects the CAs as well as the equilibrium shape of the bridge.

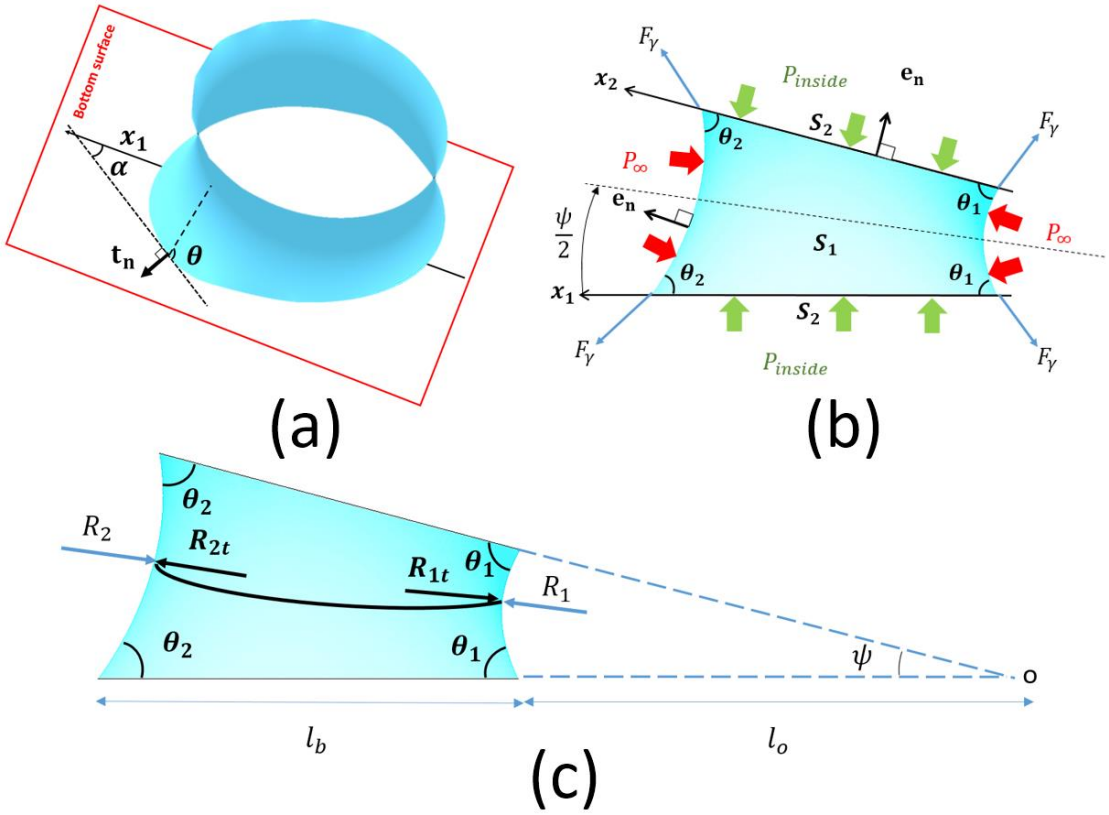

Figure 2.5 a) Perspective 3D view of the liquid bridge (top surface not shown) in contact with two identical surfaces ($\theta_a = 75°$, $CAH = 30°$, and $\psi = 15°$. b) Side view of the liquid bridge. Forces acting on the liquid bridge: surface tension forces (narrow blue arrows), pressure on the liquid-solid interface (fat green arrows), and ambient pressure on the liquid-air interface (fat red arrows) c) The menisci on the two sides of the liquid bridge: R_1 and R_2 are in-plane radii of curvatures, R_{1t} and R_{2t} are out-of-plane radii of curvatures; θ_1 and θ_2 are the CAs.

Because the bi-sector (black dotted line in Figure 2.5b) is a line of symmetry for the liquid bridge, forces perpendicular to the bi-sector form pairs with equal magnitude and opposite directions, so they naturally balance out and equilibrium in this direction is automatically satisfied. Along the bi-sector, force balance can be derived from Eqn. (2.2) by projecting each term onto the bi-sector, as:

$$\underbrace{\sin\frac{\psi}{2}2\gamma M\int_{S_2} dS}_{F_P}+\underbrace{\cos\frac{\psi}{2}\gamma\int_{cl}\cos\theta\sin\alpha\, dl}_{F_L}\underbrace{-\sin\frac{\psi}{2}\gamma\int_{cl}\sin\theta dl}_{F_n}=0 \qquad (2.3)$$

where α stands for the angle between the tangent of the contact line and the axis of symmetry on the plane of each solid surface (x_1 and x_2 in Figures 2.5a and 2.5b). Here, the direction pointing away from the cusp is assumed to be positive. The first term in Eqn. (2.3) is due to the net pressure and is denoted by F_P. Its direction depends on the sign of the bridge's mean curvature, i.e., if $M >$ 0, F_P points away from the cusp, and vice versa. The second term in Eqn. (2.3), F_L, is the projection of the lateral adhesion force (due to the surface tension force, parallel to S_2) onto the bi-sector. F_L only exists if the surfaces are not parallel. Otherwise, due to symmetry, the shape of the contact lines would be circular with a single CA along the contact line, and the net lateral force will be zero. The last term in Eqn. (2.3), F_n, is the projection of the normal adhesion force (perpendicular to S_2) onto the bi-sector. Regardless of the value of CA, the normal adhesion force is always in the same direction as $\mathbf{e_n}$; therefore, its projection on the bi-sector is always pointing towards the cusp, i.e., $F_n < 0$.

Equation (2.3) demonstrates the relation between the balance of forces along the bi-sector and the value of CAs and CAH. Both adhesion forces, F_n and F_L, are explicitly influenced by the values of CAs and CAH; also, CAs and CAH affect the shape of the contact lines, mean curvature (M), and the shape of the liquid, implicitly.

2.3.2 Constant Laplace pressure

In deriving the global force balance Eqn. (2.3), we have assumed that the pressure inside the liquid is uniform. This condition, however, should not be taken for granted, and must be satisfied by the geometry of the liquid bridge. Specifically, the Laplace pressure has to be constant, which can be met only if the mean curvature (M) is constant everywhere on the liquid-air interface. This is a very strong condition, and a general analytical model cannot be formulated to specify this condition in a closed form. However, a simplified model for the expression of curvatures can be developed with the following two simplifications: firstly, the in-plane geometry of each meniscus is assumed to be part of a circle, with R_1 and R_2 (see Figure 2.5c) being the radii of the circles on the narrow and wide sides of the bridge, respectively. Secondly, the out-of-plane radii of curvatures (R_{1t} and R_{2t}, see Figure 2.5c) are assumed to be equal; for the justification of this assumption see Section A.4 in Appendix. In Figure 2.5c, l_o and l_b stand for, respectively, the distance from the rightmost contact point of the bridge to the surfaces' cusp (o), and the width of the contact area. The Laplace pressures evaluated at the rightmost and leftmost menisci must be equal, leading to the following equation:

$$P_L = \gamma\left(\frac{1}{R_1} + \frac{1}{R_{1t}}\right) = \gamma\left(\frac{1}{R_2} + \frac{1}{R_{2t}}\right) \tag{2.4}$$

From geometry, R_1 and R_2 can be calculated as follows:

$$\frac{1}{R_1} = -\frac{\cos\left(\theta_1 - \frac{\psi}{2}\right)}{l_o \sin\frac{\psi}{2}} \tag{2.5}$$

$$\frac{1}{R_2} = -\frac{\cos\left(\theta_2 + \frac{\psi}{2}\right)}{(l_o + l_b)\sin\frac{\psi}{2}} \tag{2.6}$$

where θ_1 and θ_2 are defined in Figure 2.5c. Using the assumption that R_{1t}= R_{2t}, Eqn. (2.4) indicates that $R_1 = R_2$ must be satisfied, which ultimately corresponds to Eqn. (2.7), by setting Eqns. (2.5) and (2.6) to be equal.

$$\frac{l_o}{(l_o + l_b)} = \frac{\cos\left(\theta_1 - \frac{\psi}{2}\right)}{\cos\left(\theta_2 + \frac{\psi}{2}\right)} \tag{2.7}$$

Equation (2.7) is an additional condition to Eqn. (2.3) for bridge stability, which correlates the geometry of the liquid bridge (l_o and l_b) with θ_1, θ_2, and ψ. These two equations, establishes the interrelation between ψ, the CAs, and *CAH* of the surfaces, with stability conditions of a bridge, to allow one to understand the effect of each of CAs and CAH on the stability.

2.4 Results and Discussion

In this section, we present results on the stability of the liquid bridge. We will focus on examining the effect of θ_a and CAH on the critical angle ψ_c, and understanding the mechanisms behind. Prior to this discussion, it is prudent to point out that for the systems studied in this chapter, the stability of the bridge is independent of the liquid volume *V* and the initial placement of the droplet on the bottom surface. Specifically, if all lengths of the liquid bridge scale proportionally with cubic root of the liquid volume ($\sqrt[3]{V}$), the dimensionless quantities will remain the same across the systems with different volumes. Therefore, the critical angle, ψ_c, as a dimensionless quantity in the system, will be independent of V. For a liquid bridge between nonparallel surfaces, scaling with $\sqrt[3]{V}$ is only possible under certain conditions. These conditions are discussed in Appendix (Section A.5); there, we have shown that the experimental process and the assumption of small Bond number accommodated the conditions for the scaling of the system with $\sqrt[3]{V}$. Hence, the critical angle discussed below is independent of V. The independence of ψ_c from V was confirmed by both

experimental and numerical investigations for three different volumes (1, 2 and 3 μL), and the data will be presented later (in Figure 2.7). The systems studied in literature (e.g. Ref. 7) were not scaling, so, the findings were limited to specific volumes of liquid. Whereas in a scaled system, the results are not constrained by the liquid volume, and hence, are more general. Another consequence of scaling is that the initial location of the sessile drop on the bottom surface (see Figure 2.2a) does not affect the stability of the system; when changing the location of the sessile drop, the position of the cusp will change accordingly, so that the bridge will always form at the same location with respect to cusp of the surfaces (see Appendix Section A.5 for more details).

2.4.1 The roles of CAH and θ_a

The essential role of CAH in stabilizing the bridge can be clearly seen from the uniform pressure condition introduced in the previous section, i.e. Eqn. (2.7). Specifically, from Eqn. (2.7), since $l_o + l_b > l_o$, one has: $|cos\left(\theta_1 - \frac{\psi}{2}\right)| < |cos\left(\theta_2 + \frac{\psi}{2}\right)|$. Considering a subset of hydrophilic surfaces, i.e. when $\theta_a < \left(\frac{\pi}{2} - \frac{\psi}{2}\right)$, one can write $\theta_1 - \frac{\psi}{2} > \theta_2 + \frac{\psi}{2}$, or

$$\theta_1 - \theta_2 > \psi \tag{2.8}$$

The inequality given in Eqn. (2.8) shows that θ_1 has to be larger than θ_2 to have a uniform pressure. This is consistent with literature [7, 8, 28], as a condition for a stable bridge between hydrophilic surfaces. Given that at ψ_c, $\theta_1 = \theta_a$ and $\theta_2 = \theta_r$, Eqn. (2.8) can be written as:

$$CAH > \psi_c \tag{2.9}$$

which implies that ψ_c is bounded, and cannot be larger than CAH. As such, the bridge is necessarily unstable, if $\psi > CAH$. This finding is consistent with that in Luo et al. [7], however, inequality (2.9) does not have the ability to determine ψ_c. It only introduces CAH as a theoretical upper bound for ψ_c, which may not be reachable in many practical situations. For instance, for a bridge between

two silicon surfaces (case 1 in Table 1), ψ_c is only 3°, while the value of CAH is 22.6°. Another limitation of Eqn. (2.9) is that it resulted from the assumption that $\theta_a < \left(\frac{\pi}{2} - \frac{\psi}{2}\right)$, which may not be valid for all types of hydrophilic surfaces. For example, for the liquid bridge between the PS surfaces (with $\theta_a = 89.6°$), the critical angle is 9.6° which does not satisfy the $\theta_a < \left(\frac{\pi}{2} - \frac{\psi}{2}\right)$. Therefore, a study is needed to better evaluate ψ_c without being limited to the range of $\theta_a < \left(\frac{\pi}{2} - \frac{\psi}{2}\right)$.

The lack of understanding about the value of ψ_c comes from the fact that previous works treated all the bridges between surfaces with $\theta_a < 90°$ equally, without addressing the effect of θ_a on the stability. The role of θ_a can be most clearly understood from the global force balance, i.e. Eqn. (2.3). In Eqn. (2.3), the integrands in F_L and F_n explicitly depend on the CAs along the contact line, whose values are delimited by both CAH and θ_a. In addition, the integrals in F_L and F_n also implicitly depends on the shape of the bridge, which is significantly affected by θ_a. Therefore, the critical angle ψ_c is expected to be a function of not only CAH, but also θ_a.

To demonstrate the effect of *CAH* and θ_a on the value of ψ_c, the experimental data for ψ_c was supplemented by sixteen simulations with θ_a ranging from 40° to 90°, and CAH ranging from 10° to 30°. Figure 2.6 shows all the data from experiments and simulations. Several observations can be made. First, it is clear that the results from simulation are in agreement with experiments. Second, for a constant θ_a, increasing CAH increases the value of ψ_c. This finding shows that not only is CAH the theoretical upper bound for ψ_c, but also a direct correlation between ψ_c and CAH also exists. Such correlation has not been previously established in literature. While Luo *et al.* [7] introduced inequality in Eqn. (2.9), increase in CAH did not necessarily imply an increase in ψ_c.

Third, similar to the effect of CAH, for a constant CAH, as θ_a increases, a stable bridge can be formed for greater dihedral angles.

Finally, if the effects of θ_a and *CAH* were independent, the curves in Figure 2.6 would have been parallel straight lines, which is not the case. In fact, as *CAH* increases, the slope of the ψ_c versus θ_a curves increases, indicating stronger influence of θ_a on ψ_c than that of CAH. The increase of ψ_c with *CAH* is also more significant as θ_a increases. For instance, for a surface with $\theta_a = 40°$, 10° increase in CAH from 10° to 20° only increases ψ_c by 1°, whereas the same 10° increase in CAH results in 5.5° increase in ψ_c for a surface with $\theta_a = 78.8°$. These results demonstrate the complex nonlinear and interdependent influences of θ_a and *CAH* on the stability of the liquid bridge which was unknown prior to this study.

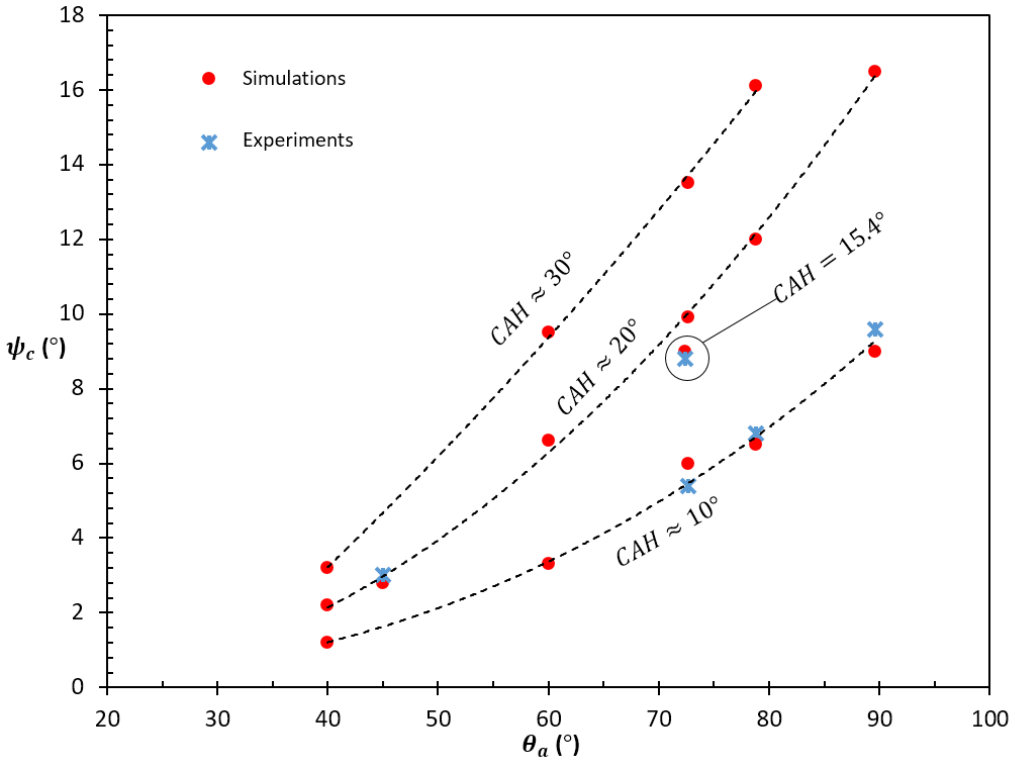

Figure 2.6 Simulation and experimental results to find the critical angle. The error in the experiments data are $\pm 0.2°$ (not shown). Dashed lines are to guide the eyes.

Considering the general trend of ψ_c as a function of CAH and θ_a, an empirical equation in the form of Eqn. (2.10) is proposed (a reasoning behind this form of equation is given in the next subsection).

$$\psi_c = 0.044\theta_a^{1.535}(\cos(\theta_a - CAH) - \cos(\theta_a)) \tag{2.10}$$

where the numerical constants (0.044 and 1.535) were found using Least Squares fitting to the simulation data in Figure 2.6, and all CAs are in degrees. The experimental data was not included in the fitting, so that they could be used as an independent set of data to test the viability of Eqn. (2.10). Equation (2.10) can be used for any drop volume, provided that the Bond number is sufficiently small for the gravity to be negligible. This is because as volume increases, all the lengths in the system change proportionally. The independency of Eqn. (2.10) on volume was further confirmed by performing additional simulations and experiments with various volumes (1, 2, and 3 μL); as shown in Figure 2.7. For all the volumes, the critical angles calculated from Eqn. (2.10) have excellent agreement with ψ_c from experiments and simulations.

Equation (2.10) can be used as a tool to predict whether a stable bridge can be formed between two identical hydrophilic surfaces (with $\theta_a \leq 90°$), by only knowing θ_a and CAH of the surfaces. In addition, according to Eqn. (2.10), in the range of hydrophilic surfaces, the actual maximum upper bound for ψ_c is $\approx 44°$, which is achieved when the surfaces have $\theta_a = CAH = 90°$. This maximum value also was verified with Surface Evolver (see Figure 2.7).

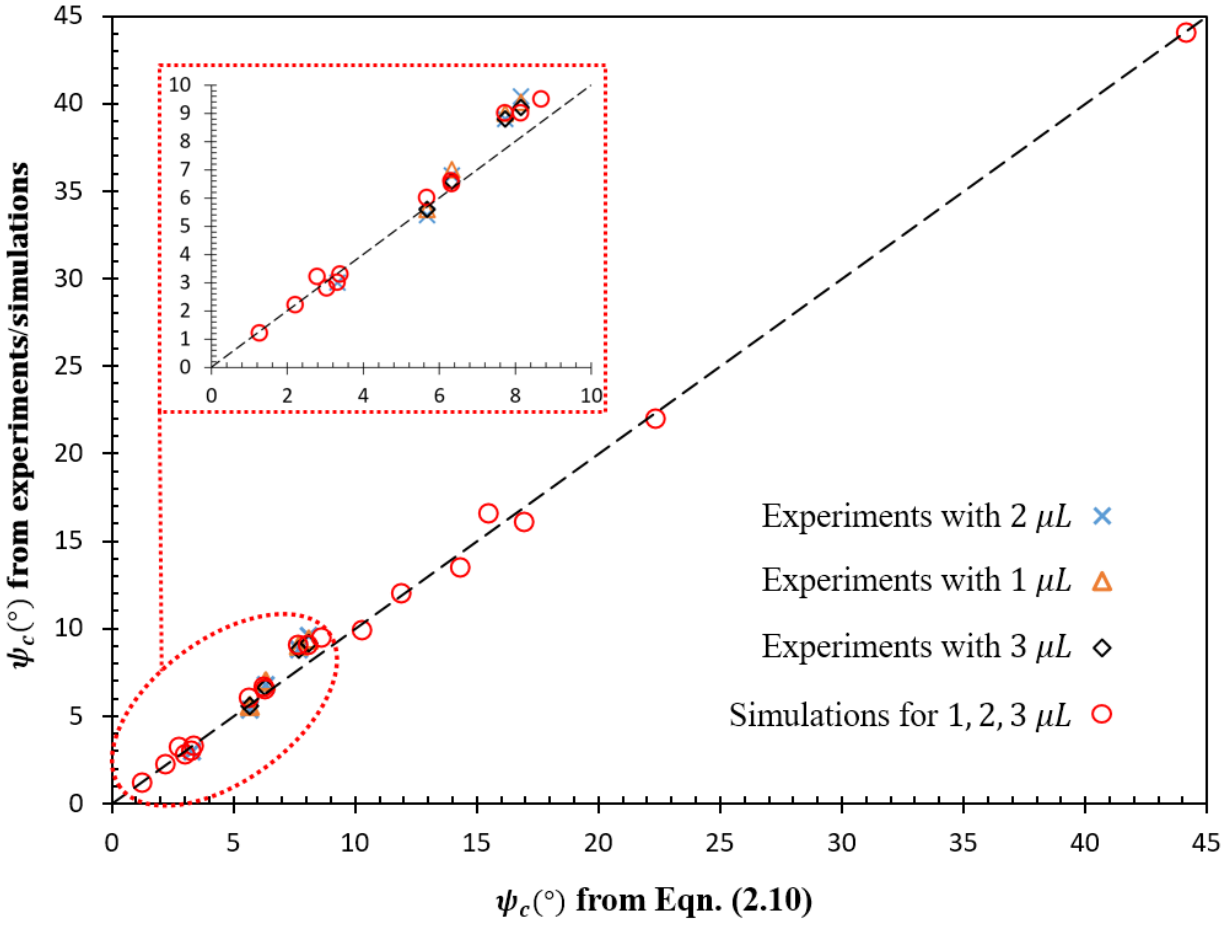

Figure 2.7 Comparison between ψ_c calculated from Eqn. (2.10) and the corresponding experimental and simulation data for three different volumes (1, 2 and 3 μL). The simulation results for different volumes were identical, hence, simulation data points for different volumes are shown with one symbol. The dashed line has a slope of one. The inset plot is a magnified view for ψ_c from 0 to 10°.

2.4.2 Understanding the effect of CAH and θ_a on ψ_c

Having observed the effect of CAH and θ_a on ψ_c, both qualitatively and quantitatively, next we use the formulation presented in the Section 2.4 to explain the physical basis of the observed dependence of ψ_c on θ_a and CAH.

First, we explain the physical basis for the effect of CAH on ψ_c. In Figure 2.8a, using Surface Evolver, the distribution of CAs along the contact line (i.e. versus azimuthal angle ϕ, see Figure

2.8b) on the bottom surface are shown for a system with $\theta_a = 75°$ and $CAH = 30°$. In this system, ψ_c is slightly larger than 15°. When $\psi = 7°$ (almost half the value of ψ_c), the CAs between the rightmost and leftmost of the bridge are monotonically distributed i.e., moving away from θ_2 at the wide side ($\phi = 0°$), CA continuously increases until at the narrow side ($\phi = 180°$) it reaches θ_1. At $\psi = 15°$, since the bridge is at the threshold of moving towards the cusp, the maximum difference between the CAs on the two sides of the bridge ($\Delta\theta = \theta_1 - \theta_2$) occurs: $\theta_1 = \theta_a$ and $\theta_2 = \theta_r$. At this point, a large portion of CAs on the wide side of bridge (ϕ from 0° to 83°) attain θ_r, then CAs increase rapidly to θ_a, and a large portion of CAs on the narrow side (ϕ from 117° to 180°) attain the θ_a value.

Due to such variation of CAs along the contact line, the local lateral adhesion force $dF_L = \gamma \cos\theta \sin\alpha \, dl$ on the wide side of the bridge are larger than that on the narrow side, e.g., see Figure 2.8b for the depiction of dF_L by scaled vectors on the bottom surface contact line when $\psi = 15°$. As a result of this non-uniform distribution, a net lateral adhesion force exerts on the bridge, pointing away from the cusp. The projection of the net lateral force onto the bi-sector is equal to the F_L term in Eqn. (2.3). Given a system with specified CA and *CAH*, maximum F_L (denoted hereafter as F_{Lmax}) is attained when $\Delta\theta = CAH$, and the dihedral angle reaches ψ_c. In other words, F_{Lmax} is bounded by the magnitude of CAH. A larger *CAH* would allow for larger range of CA differences, which creates larger differences between local lateral adhesion forces on the two sides of the bridge, leading to a greater F_{Lmax}. This increased F_{Lmax} can provide a larger force to stabilize the bridge, hence to increase ψ_c (a quantitative example is given in Appendix Section A.6).

Given the discussion above, F_{Lmax} is achieved when $\theta_1 = \theta_a$ and $\theta_2 = \theta_r$. In this limit, the projection of surface tension forces on the bi-sector scales with $\cos(\theta_a)$ at the narrow end of the

bridge while it scales with $\cos(\theta_r) = \cos(\theta_a - CAH)$ at the wide end. Therefore, it is expected that F_{Lmax} to correlate positively with $\cos(\theta_a - CAH) - \cos(\theta_a)$. Since the effect of CAH on ψ_c is manifested through F_{Lmax}, a term in the form of $\cos(\theta_a - CAH) - \cos(\theta_a)$ is a rational choice for Eqn. (2.10) to predict ψ_c.

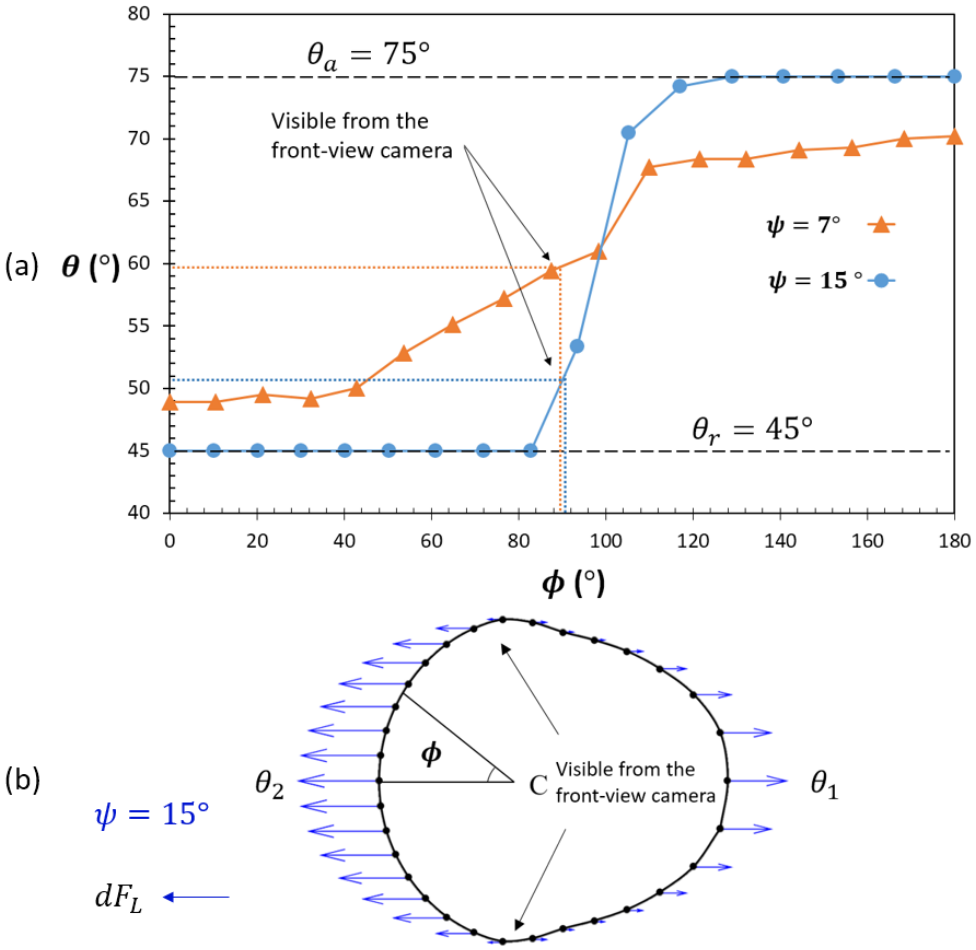

Figure 2.8 a) Value of contact angles along the contact line of a liquid bridge between two identical surfaces with $\theta_a = 75°$ and $CAH = 30°$, plotted against contact line azimuthal angle. CAs were calculated using Surface Evolver for two cases: $\psi = 7°$ and $15°$. b) Shape of the contact line on bottom surface of a liquid bridge between two identical surfaces, with $\theta_a = 75°$, $CAH = 30°$ and $\psi = 15°$ (calculated by Surface Evolver). The azimuthal angle (ϕ) is measured from the wide side of the bridge using the centroid of the contact line (C), i.e., $\phi(0°) = \theta_2$. On the contact line, the local lateral adhesion force dF_L are blue arrows (vectors) and are drawn to scale.

Whereas CAH promotes the stability of the liquid bridge by increasing F_{Lmax}, increasing θ_a reduces F_L that is required for the global force balance. To see this, the three terms on the LHS of Eqn. (2.3) were calculated numerically using Surface Evolver for several systems, where CAH and ψ were fixed at 10° and 3°, respectively; and θ_a ranged from 60° to 90°. Because $\sqrt[3]{V}$ is the characteristic length of system, all the force components were normalized by $\gamma\sqrt[3]{V}$ (the superscript (*) indicates that the force is normalized by $\gamma\sqrt[3]{V}$ and hence dimensionless). All the bridges are stable, so the force components can be compared for varying values of θ_a (Figure 2.9). Figure 2.9 shows that as θ_a increases, absolute value of F_P^* decreases to zero, first, then F_P^* changes sign from negative to positive, and continues to increase with θ_a afterwards. As a result, the F_L^* required to balance $F_P^* + F_n^*$ (see Figure 2.9) decreases continuously as F_L^* is always positive. This means that the need F_L^* to balance, can be generated with a smaller difference between the CAs on the two sides of the bridge (see $\Delta\theta$ in Figure 2.9). Consequently, for a system with larger θ_a, the maximum $\Delta\theta$ ($= CAH$), generating F_{Lmax}^*, occurs at a greater ψ compared to a system with smaller θ_a. That is, ψ_c increases as θ_a increases (this is found to be true for hydrophilic surfaces with $\theta_a < 90°$, see details in Section A.7 in Appendix).

Because F_P^* is directly calculated from the mean curvature of the liquid-air interface, M (see Eqn. (2.3)), the changes in the sign and value of F_P^* with θ_a can be explained by looking at how M changes with θ_a. The mean curvature is related to the two principle radii of curvature by $M = \left(\frac{1}{R} + \frac{1}{R_t}\right)^{-1}$, therefore its sign and magnitude is determined by the relative magnitude of R (in-plane principal radius of curvature, negative for $\theta_a < (\frac{\pi}{2} + \frac{\psi}{2})$, see Eqn. (2.5)) and R_t (out-of-plane principal radius of curvature, positive). The inset pictures in Figure 2.9 show the equilibrium shapes of the liquid bridge (to scale) at three θ_a values. When the surfaces have $\theta_a = 60°$, R

obtains a smaller magnitude than R_t , therefore, $M < 0$ and $F_P < 0$. As θ_a increases, $|R|$ grows larger until at $\theta_a = 70°$, it obtains a value equal to R_t, so that $M = 0$ and $F_P^* = 0$. The increase in $|R|$ continues, causing F_P^* to be more and more positive. Such continuous transformation of liquid bridge's curvatures with respect to the increase in θ_a are due to two effects: First, for a given volume, as θ_a increases, the drop sits higher on the lower surface (i.e. H_{ini} in Figure 2.2 increases); as such, when the top surface touches the drop, the average height of the formed bridge increases compared to a system with smaller θ_a. Second, since CAH is fixed, as θ_a increases, CAs obtain values closer to 90°. These two factors together cause $|R|$ to increase with θ_a.

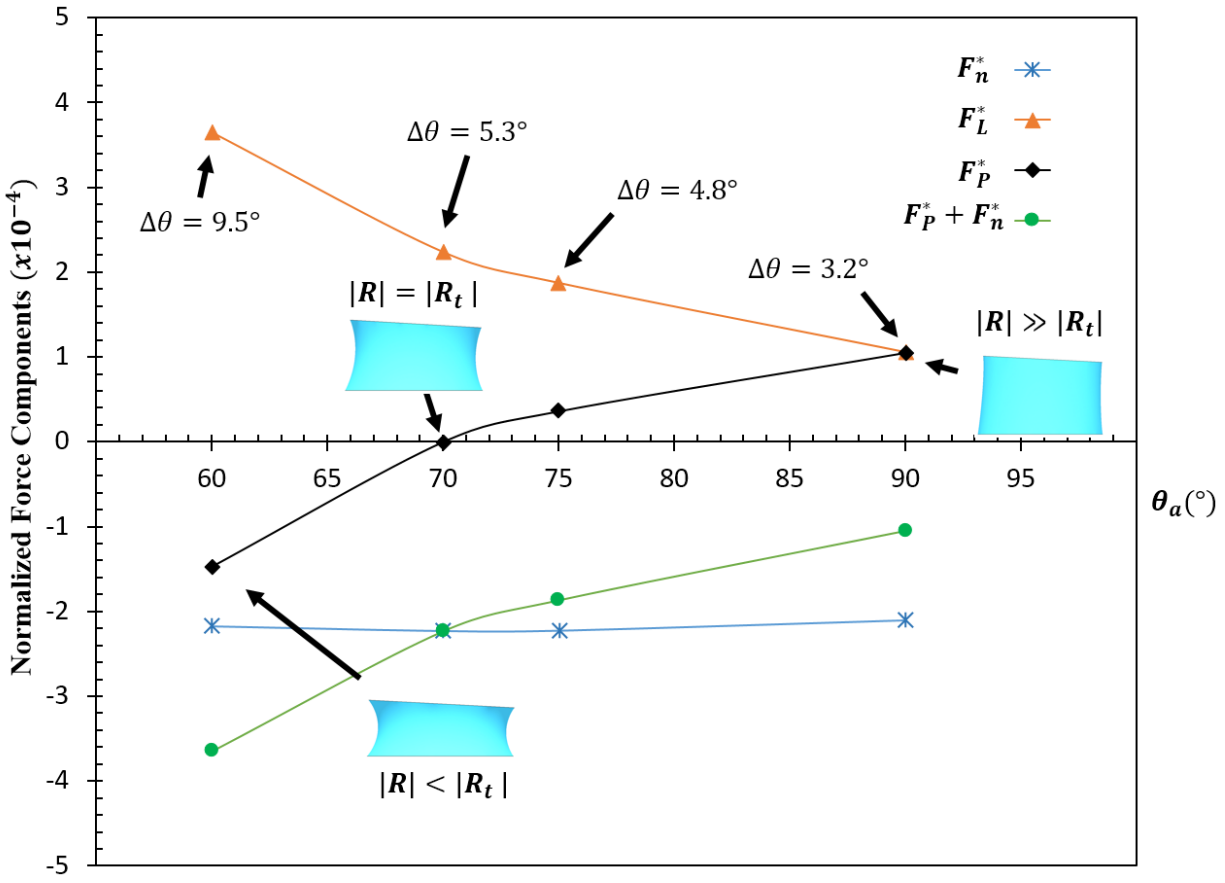

Figure 2.9 The force components from Eqn. (2.3), all normalized by $\gamma\sqrt[3]{V}$. CAH and ψ are fixed at 10° and 3°, respectively. $\psi = 3°$ is less than the critical angle in all cases, so all bridges are stable. The in-plane, and out-of-plane curvatures of the bridge are donated as R and R_t, respectively. Simulated shapes of the bridge are included to illustrate the change in curvatures. Inset images of the bridges are to scale (have the same volume). The value of $\Delta\theta$ was averaged on top and bottom surfaces. Lines are to guide the eyes.

To this point, we have used Eqn. (2.3) to explain the effects of θ_a and CAH on ψ_c. Similarly, these effects can be explained by examining the uniform pressure condition introduced in Eqn. (2.7). At $\psi \approx \psi_c$, Eqn. (2.7) can be written as:

$$\frac{l_o}{(l_o + l_b)} = \frac{\cos\left(\theta_a - \frac{\psi_c}{2}\right)}{\cos\left(\theta_a - CAH + \frac{\psi_c}{2}\right)} \tag{2.11}$$

It can be shown that in order to satisfy Eqn. (2.11), increase in θ_a or CAH must be accompanied by an increase in ψ_c. Details of the proof can be found in Section A.8 in Appendix.

2.4.3 Discussion on the effects of loading history and θ_{ini}

In the system studied in the previous sections, the top surface has a pre-determined dihedral angle when it is approaching the drop on the lower surface (see Figure 2.2). In the presence of CAH, it is expected that the equilibrium values of CAs and the location of contact lines can depend on their evolution history. To examine how the loading history might affect the prediction of ψ_c (Eqn. (2.10)), in Figure 2.10, we consider a different way of introducing the dihedral angle. In this case, the two surfaces are first parallel when the bridge is formed (having θ_a and θ_r as initial CA on the top and bottom surfaces, respectively), then the top surface pivots around its center and forms a dihedral angle with the lower surface. We used the Surface Evolver simulations to calculate ψ_c under such loading condition for the same surfaces studied in Figure 2.6. During the simulations, ψ was increased gradually (with 0.1° steps) from zero until at ψ_c no equilibrium shape could be found after evolving the surface. We found that the calculated ψ_c (Figure 2.11) are found to differ from the prediction in Eqn. (2.10) by is less than 10% in all cases. As such, Eqn. (2.10) can be thought of as a general practical formulation to calculate ψ_c regardless of the loading history.

However, Eqn. (2.10) holds, only if θ_{ini} is close to θ_a. It can be shown that, for example, if due to CAH, the value of θ_{ini} to be less than θ_a, the value of ψ_c becomes smaller. The effect of θ_{ini} on ψ_c is discussed extensively in Appendix Section A.9. For a system with given θ_a and CAH, the maximum of ψ_c is seen when $\theta_{ini} = \theta_a$ (i.e. $\psi_c|_{\theta_{ini}=\theta_a}$), which can be calculated from Eqn. (2.10). Therefore, Eqn. (2.10) can provide an upper bound for ψ_c of a system with $\theta_{ini} < \theta_a$ (i.e. $\psi_c|_{\theta_{ini}<\theta_a} < \psi_c|_{\theta_{ini}=\theta_a}$). It can be shown that in the range of hydrophilic surfaces ($\theta_a \leq 90°$ and

$CAH \leq 90°$), $\psi_c|_{\theta_{ini}=\theta_a} < CAH$. Hence, $\psi_c|_{\theta_{ini}<\theta_a} < \psi_c|_{\theta_{ini}=\theta_a} < CAH$, which means that $\psi_c|_{\theta_{ini}=\theta_a}$ is a better upper bound for $\psi_{c|\theta_{ini}<\theta_a}$ than CAH given by Eqn. (2.9).

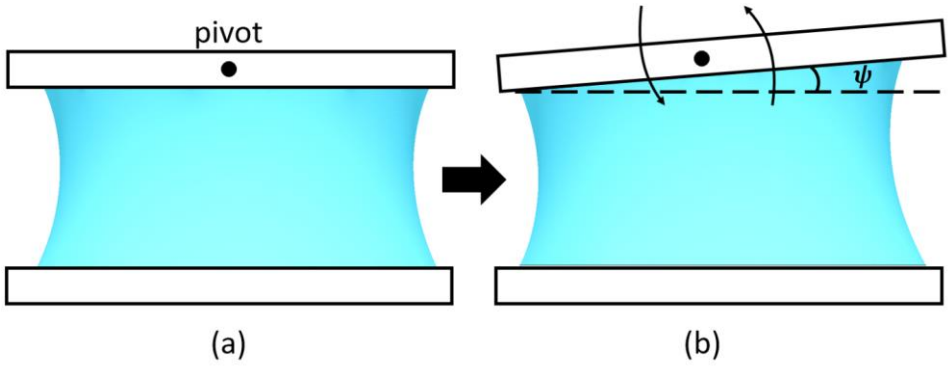

Figure 2.10 a) The bridge is formed with parallel surfaces. b) the top surface pivots around its center to form a dihedral angle ψ with the lower surface.

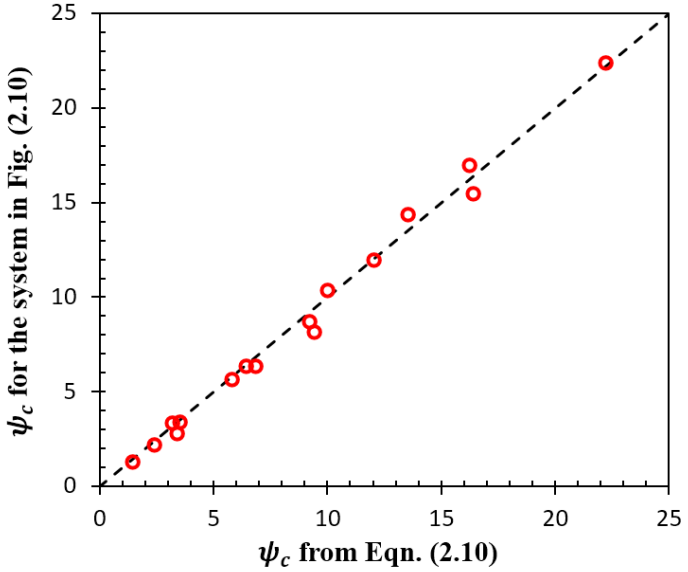

Figure 2.11 Comparison between ψ_c calculated from Eqn. (2.10) and the corresponding ψ_c from simulations for the system shown in Figure 2.10. Three different volumes were used (1,2, and 3 μL).

To conclude, we demonstrated that when ψ is above a critical value ψ_c, the bridge exhibits spontaneous movement towards the cusp of the surfaces. This movement can be used to induce effortless drop motion in practical applications e.g. microfluidics. We found that ψ_c can be increased by increasing CAH or θ_a, or both. Based on that, we proposed an empirical model to predict the stability of a bridge only by knowing θ_a and CAH of the surfaces. Although a stable bridge does not exhibit the spontaneous motion, still, it can be moved by mechanical actuations. Such movement is not effortless, but controllable. The movement of stable bridges due to mechanical actuations has been extensively discussed in Chapter Three.

Chapter Three: Motion of Liquid Bridges between Nonparallel Surfaces[1]

3.1 Introduction

Rapid rate of development for drop-based systems in technology (e.g. in microfluidics), has meant that more and more methods are being developed to control and employ droplets [1-17]. The dynamic behavior of a liquid bridge between two nonparallel surface has drawn much attention due to its potential applications in transferring small droplets [3, 7, 8, 12-16]. For instance, a drop forming a liquid bridge between two nonparallel hydrophilic surfaces will spontaneously move towards the cusp of the surfaces, if the dihedral angle between the surfaces (ψ) is larger than a critical value (ψ_c) [7, 8]. Such spontaneous movement has been used in practical applications such as plate-based fog collectors [3]. On the other hand, as shown in Chapter two, if $\psi < \psi_c$, the liquid bridge remains stable without exhibiting any horizontal movement. Still, the bridge can be influenced to move horizontally using mechanical actuations, e.g. by moving one of the surfaces vertically. For example, as shown in Figures 3.1a and 3.1b, the contact points on the wide side of the bridge remains pinned during the compressing, while the contact points on the narrow side advance towards the cusp of the surfaces, causing the bulk of liquid to move towards the cusp. Similarly, during the stretching phase, the contact points on the narrow side remains pinned while the ones on the wide side recede toward the cusp (sees Figures 3.1b and 3.1c). Due to the asymmetric spreading and retreating of the contact lines during the compressing and stretching phases, a net movement in the bulk liquid takes place. Unlike the spontaneous horizontal

[1] Chapter Three of this thesis will be submitted in future as M. Ataei, T. Tang and A. Amirfazli, "Motion of Liquid Bridges between Nonparallel Surfaces" for publication.

movement of the bridge when $\psi \geq \psi_c$, this method of drop actuation enables horizontal movement of the bridge in a controllable fashion.

The pinning of contact points is essential for such horizontal movement to exist; it allows one side of the bridge to remain pinned, while the other side is advancing or receding. Such pinning is a result of Contact Angle Hysteresis (CAH), which allows the contact points to move, only if their local contact angle (CA) attain certain values i.e., they are only allowed to advance, if their local CA attain a maximum value known as the advancing contact angle (θ_a), or recede, if their local CA attain a minimum value, known as the receding contact angle (θ_r). The difference between these two bounding values is known as CAH (i.e. $CAH = \theta_a - \theta_r$). For any value of CA inside the CAH range, the contact points remain pinned and are not allowed to move.

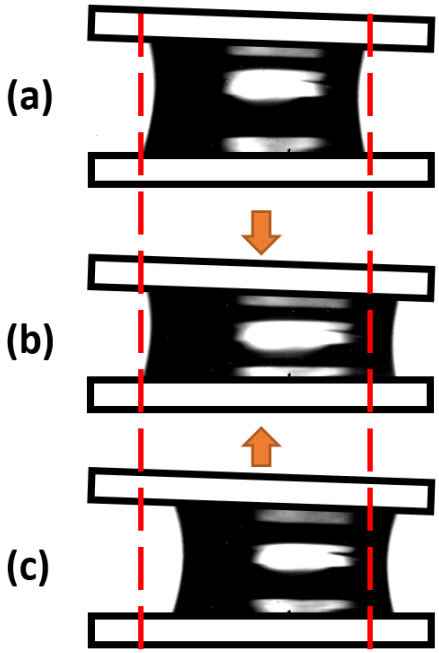

Figure 3.1 a) Liquid bridge is compressed between two identical nonparallel surfaces. b) The bridge spreads on its narrower side, while the contact points on the wider side remain pinned. c) In the stretching stage, the bridge recedes on its wider side while the contact points on the narrower side remain pinned, leading to bridge motion.

In the literature, such horizontal movement of a liquid bridge due to compressing and stretching has been reported in several studies [7, 8, 12, 16]. Prakash *et al.* [8] first reported that a certain type of Phalarope shorebirds uses this method to transfer their prey inside a bridge from their beak tips towards their month. They studied quasi-static movement of the bridge in the absence of gravity, where the pressure inside the bridge remains uniform during the movement. Accordingly, the radii of curvature on the narrower and wider sides of the bridge had to be equal, a condition that requires the CAs on the narrower side of the bridge to be larger than that on the wider side [8]. This explains the movement of the bridge with the principle discussed in Figure 3.1 i.e. in compressing, the CAs on narrower side of the bridge reach θ_a and their contact points advance earlier than that on the wider side, and in stretching, the CAs on the wider side reach θ_r and their contact points retreat first [8].

Despite the reported results on the horizontal movement of the bridge, there are several unsolved issues in the literature. First, there has not been any systematic understanding of the governing parameters controlling the horizontal movement. These governing parameters can be categorized into three claws: mechanical parameters, i.e. the amount of compressing and stretching of the bridge (Δh); geometrical parameters, i.e. the dihedral angle between the two surfaces (ψ); and material (wettability) parameters i.e. θ_a, θ_r, and CAH of the surfaces. To apply this method of drop manipulation in practice, one needs to understand how the horizontal movement is influenced by these parameters. In addition, several key elements of the horizontal movement have not been thoroughly studied. For example, if the amount of compressing or stretching are not sufficient, the pinning of contact lines cannot be overcome, so the bridge will not move [7, 8]. In studies to date the bridge was always amply squeezed and stretched that the pinning of contact lines was overcame [7, 8]. However, it is unclear what minimum amount of compressing and stretching causes motion.

Furthermore, in a favorable condition, depinning of the contact lines occur asymmetrically, as explained earlier for a definite motion in Figure 3.1. Still, the bridge may undesirably regress backwards by advancing on the wider side during compression, and/or receding on the narrower side during stretching [7, 8, 16]. Under such a condition, the mechanical energy given to the liquid is used to move the bulk of the liquid away from the cusp, which may not be desirable. Thus, the liquid motion is regarded more efficient if asymmetric depinning occurs in both compression and stretching stages. In one study [16], instead of smooth surfaces, lopsided saw-tooth surfaces were used to obstruct the inefficient backwards movement of the bridge.[12] Though, using saw-tooth surfaces only enhanced the movement, if the surfaces were hydrophobic. There has not been any understanding on how one can prevent backward movement of the bridge when the surfaces are hydrophilic.

There is the issue of seemingly contradictory experimental results in the literature. To move the drop to the desired position, the bridge can undergo several sequential compressing and stretching, i.e. loading cycles. Luo *et al.* [7] showed that, when the surfaces are hydrophilic (with CA < 90°), the traveled distance in one cycle increases, as the bridge gets closer to the cusp of surfaces after each loading cycle. This is in contradiction with the experimental results of Prakash *et al.* [8]; the distance traveled by the liquid bridge in each cycle became smaller as it got closer to the cusp of the hydrophilic surfaces. There is no explanation for what has caused the difference in the reported results.

This chapter aims to address the above issues in the literature, as in line with the objectives of the thesis (see Objectives 3-5 in Section 1.3) by answering the following questions: What are the effects of the governing parameters on the horizontal movement of a liquid bridge? What is the minimum amount of compressing and stretching that can guarantee the movement of a bridge?

How one can prevent backwards motion of a bridge (i.e. achieve asymmetric depinning)? What are the changes in the behavior of a bridge, when it undergoes multiple loading cycles? To answer these questions, we used both experimental and numerical investigations, and focused on liquid bridges between two identical nonparallel hydrophilic surfaces. Since CAH is the difference between θ_a and θ_r (i.e., $CAH = \theta_a - \theta_r$), θ_a and CAH were chosen as the two independent material (wettability) parameters. A wide range of surfaces with different wettabilities are needed to fully understand the material (wettability) effects. In practice, precisely controlling θ_a and CAH of surfaces is not easy. To overcome this difficulty, we used a numerical model based on Surface Evolver [22, 23] to augment our experimental results with a wide range of θ_a and CAH. In addition, Surface Evolver provided us with information about the 3D shape of the bridge during compressing and stretching (such as the evolution of contact angles and contact lines) which, due to the non-trivial geometry of a bridge between nonparallel surfaces, is not easy to acquire in experiments. The experimental data were used to examine the viability of the Surface Evolver model as well.

In the systems studied in literature, compressing and stretching of the bridge was achieved by varying ψ with respect to the cusp of the surfaces as a tweezer-like mechanism (i.e. by pivoting the top surface with respect to the surfaces' cusp (S), see Figure 3.2a). However, in this work, compressing and stretching was achieved by direct vertical motion of the top surface, while ψ remained fixed (see Figure 3.2b). This can help us to decouple the effect of Δh and ψ on the horizontal movement, and study their effects individually. Under certain conditions, these two systems can be equivalent, which they have been explained in Appendix Section B.1, where we have shown that most of the systems studied here (e.g. systems in Figures 3.4-10) satisfies those conditions.

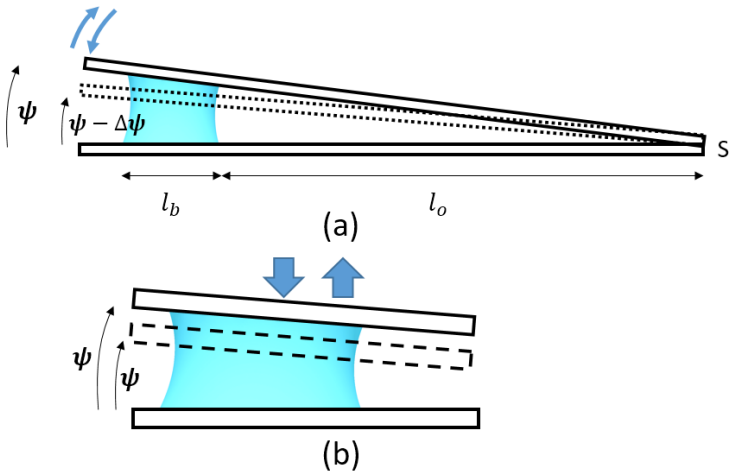

Figure 3.2 a) Schematic of the system studied in refs. 7, 8 and 16. The compressing and stretching of the bridge was provided by varying ψ around S. b) The compressing and stretching of the bridge studied here was provided by direct vertical motion of the top surface, while ψ remained fixed.

3.2 Methods and Materials

3.2.1 Experimental

The experimental process is depicted in Figure 3.3 schematically. In each experiment, a distilled water drop (1, 2, and 3 μL) was placed on a stationary flat surface, having θ_a as the initial contact angle (Figure 3.3a). Next, a tilted surface from top was vertically moved down slowly ($0.05 mm/s$) to form a bridge. Afterwards, the bridge was compressed for a distance of Δh, and then stretched for the same amount. The compressing and stretching process was repeated for five cycles (see Figure 3.3). The height of the top surface was measured from an axis perpendicular to the bottom surface and passing through the apex of the initial sessile drop (see Figure 3.3a). Horizontal location of the liquid was measured using the coordinate X (See Figure 3.3b) from the middle point of the contact line on the bottom surface (point C in Figure 3.3b). The origin for X was placed at C after bridge formation and prior to the start of the first cycle. The horizontal movement of the drop in the nth cycle can then be described by $\Delta X_n = X_n - X_{n-1}$, where X_n is the position of C

after the nth cycle (note: $X_0 = 0$). Movement towards the surfaces' cusp is considered positive ($\Delta X > 0$).

In each experiment, the top and bottom surfaces were identical. Their wettability properties are listed in Table 3.1, as well as the value of Δh and ψ used for each pair of surfaces. Poly(methyl methacrylate) (PMMA) and poly(ethyl methacrylate) (PEMA) were used to fabricate hydrophilic surfaces, by means of spin coating based on Chen *et al.* [20] guidelines. The values of θ_a and *CAH* were measured using the sessile drop method. The surface fabrication details were similar to Chapter two (see Appendix Section A.1). As shown in Table 3.1, PMMA and PEMA have a similar θ_a, but different CAH. This allows us to address the effect of *CAH* on horizontal movement independently. On the other hand, to address the effects of θ_a, surfaces with similar CAH but different θ_a were used in the simulations (see Section 3.2.2).

The experimental setup was similar to the one in Chapter Two. (see Section 2.3.1, additional details on the experimental process are given in Appendix D). All the experiments were done in ambient temperature (21°), and pressure (988 mBar). Very small capillary number Ca = $\mu U/\gamma \sim O\,(10^{-6})$ and Weber number We = $\rho U^2 \sqrt[3]{V}/\gamma \sim O\,(10^{-8})$ were found; U is the velocity of the top surface; $\sqrt[3]{V}$ is the cubic root of the liquid volume, which is a characteristic length in the system; and γ, μ, and ρ are, respectively, the surface tension, viscosity and density of the liquid. Given the small Ca and We numbers, the whole process can be treated as quasi-static. The effect of gravity was also negligible, due to the small Bond number Bo = $g\rho R^2/\gamma \sim O\,(10^{-2})$ in the experiments; g is the gravitational acceleration and R is taken to be the radius of the best fitted cycle to the contact line of the bridge on the bottom surface. Finally, the effect of evaporation was considered to be negligible, with the maximum and average evaporation during the experiments being 10% and 6%, respectively. Each experiment was repeated four times.

In Chapter two, we have shown that, as long as the initial contact angle of the sessile drop with the bottom surface (θ_{ini}, see Figure 3.3a) and ψ remain the same in the experimental process, one can take $\sqrt[3]{V}$ as the characteristic length of the system (see detailed discussion in Appendix Section A.5). These two conditions of fixed θ_{ini} and ψ were met in the experimental process; when changing the volume (1, 2 or 3 μL) the experiment was repeated with the same ψ, and because of the method of drop deposition on the surface θ_{ini} was always close to θ_a. Therefore, all the lengths in the system (h, Δh X, ΔX_n) scale proportionally with $\sqrt[3]{V}$. Accordingly, the following normalization was introduced: $h^* = h/\sqrt[3]{V}$, $\Delta h^* = \Delta h/\sqrt[3]{V}$, $X^* = X/\sqrt[3]{V}$, and $\Delta {X_n}^* = \Delta X_n/\sqrt[3]{V}$, i.e., the superscript (*) indicates that the quantity is normalized by $\sqrt[3]{V}$, and hence dimensionless. A consequence of scaling of the system is that the initial horizontal location of the bridge relative to the cusp of the surfaces, as well as the initial height of the bridge are only functions of ψ and θ_{ini} ($\approx \theta_a$ here), thus, they are not independent parameters (see Appendix Section A.5).

Having larger ψ or Δh than that of table 3.1 were not feasible because the surfaces made contact at the cusp e.g. having $\Delta h = 0.4mm$ at $\psi = 4°$ was not possible with the experimental setup.

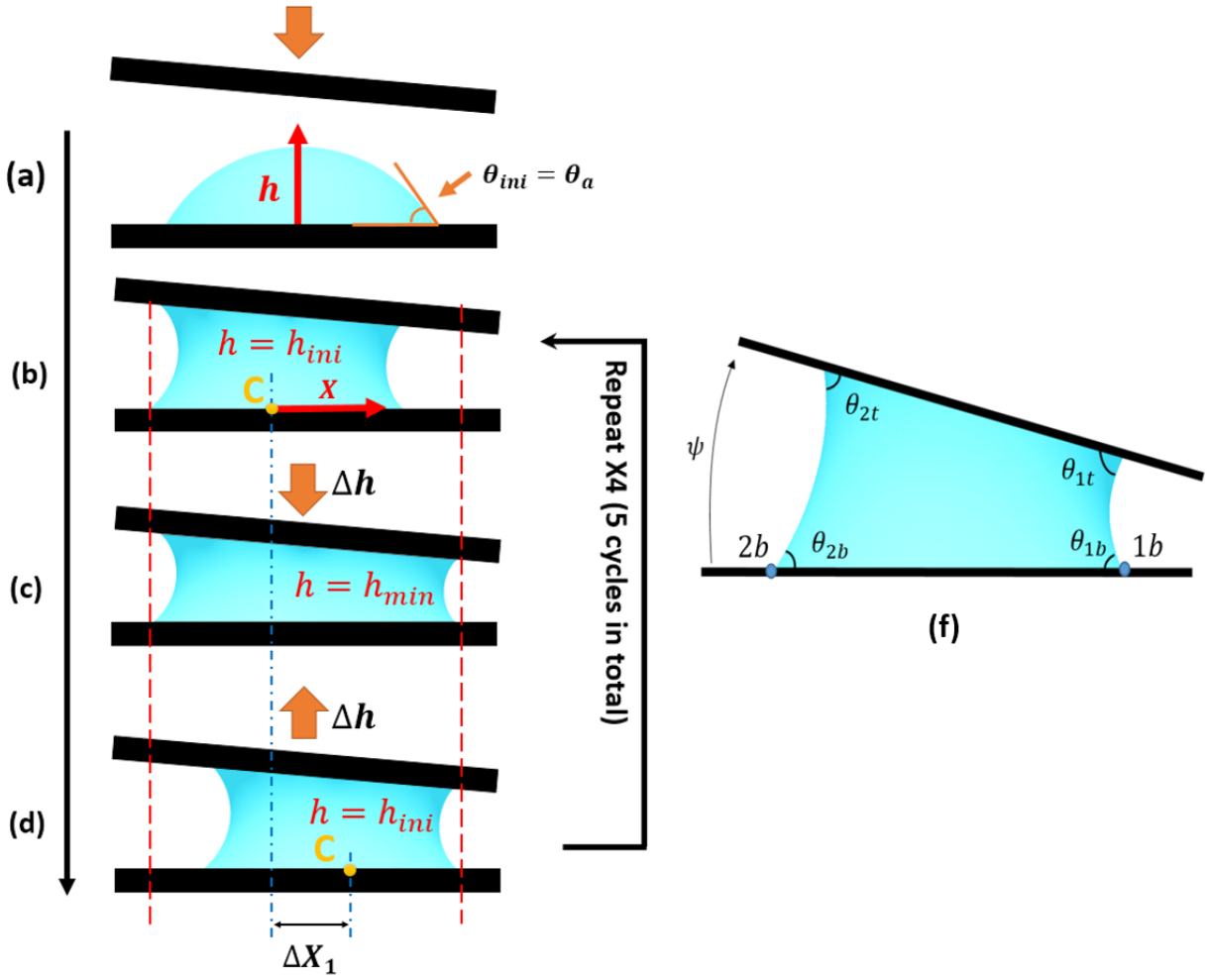

Figure 3.3 a) Tilted top surface was moved down to form the bridge. *h* is measured perpendicular to the bottom surface at the drop apex. b) The bridge is stabilized before any compressing starts. Horizontal axis is towards surfaces' cusp. c) The bridge is compressed for Δh; the height of the bridge at this point is denoted as h_{min}. d) The compressed bridge was then stretched for Δh to return to h_{ini}. f) The bridge contact points on the wider side and the narrower side of the bridge bottom surface are denoted as 2b and 1b, respectively on the bottom surface) Similar notation is used for the contact points on the top surface. The CAs are therefore denoted as θ_{1b} *and* θ_{2b} (on the bottom surface), and θ_{1t} *and* θ_{2t} (on the top surface).

Table 3.1 Wettability properties of the surfaces used in the experiments (three measurements for each surface) as well as the value of ψ and Δh for the corresponding experiments. The maximum ψ used ($= 4°$) is smaller than ψ_c of the systems.

Case#	Surfaces	θ_a	CAH	ψ	Δh
1	PMMA	80.1°±0.7°	19.6°±1.2°	2, 3 °	0.2, and 0.4 mm for each ψ
				4°	0.2 mm
2	PEMA	81.2°±0.4°	12.1°±0.6°	2, 3 °	0.2, and 0.4 mm for each ψ
				4°	0.2 mm

3.2.2 Simulations

Surface Evolver is a powerful tool to find the equilibrium shape of a surface subject to constraints [22, 23]. Because the experimental process in this study can be treated as quasi-static, it is possible to use Surface Evolver. Though, CAH is not included in Surface Evolver by default, we have implemented CAH by applying the Santos *et al.* [27] friction model. In this model, a friction force is introduced on the contact line. This force keeps any points on the contact line pinned when their local CA (θ) is between the advancing CA (θ_a) and receding CA (θ_r), and allows any contact points to advance or retreat when θ reaches θ_a or θ_r, respectively.

Since the bridge was formed between identical surfaces, ideally, it should possess a symmetrical profile about the bi-sector of the surfaces. However, in the presence of CAH, multiple equilibrium shapes for the liquid bridge may exist and the bridge may not necessarily be symmetrical about the bi-sector. In fact, the CAs may lie anywhere between θ_a and θ_r depending on the evolution history of CAs, and contact lines, during the formation of the liquid bridge. In our experiments,

when the top surface touches the sessile drop on the bottom surface, the liquid expands on the top surface with θ_a, while recedes on the bottom surface with θ_r. Because of this, the final equilibrium CAs on the top surface ($\theta_{1t}\ and\ \theta_{2t}$ in Figure 3.3f) are close to θ_a while those on the bottom surface ($\theta_{1b}\ and\ \theta_{2b}$ in Figure 3.3f) are close to θ_r. In addition, the CAs on the narrower side of the bridge are larger than those on the wider side. For example, for the liquid bridge between two PMMA surfaces (case #1 in Table 1) with $\theta_a = 80.1°$ and $\theta_r = 60.5°$, at $\psi = 2°$, the final equilibrium CAs of the formed bridge are: $\theta_{1t} = 79.1°$, $\theta_{2t} = 74.2°$, and $\theta_{1b} = 65.2°$, $\theta_{2b} = 62.5°$ (see details in Appendix Section B.3). The effect of the evolution history of CAs and contact lines during the formation of the liquid bridge was included in the Surface Evolver model using the process introduced in Chapter two. This process allowed us to initiate the compressing stage with a configuration where the CAs and contact lines close to real systems in experiments, instead of an ideal symmetrical geometry about the bi-sector of the surfaces.

After finding the equilibrium shape of the formed bridge, the top surface was moved vertically to compress the bridge with 0.01mm increments. The new equilibrium shape of the liquid bridge was determined again subjected to the change in height of the top surface. The equilibrium shape of the bridge in the preceding evolving step (before the 0.01mm compressing) was used as the new initial condition for the next evolving step. After completing the compressing stage, a similar procedure was applied for the stretching stage, where the top surface was lifted in 0.01mm increments and the system was evolved again at each step. These processes were then repeated for the subsequent loading cycles.

Simulations were done using surfaces with θ_a ranging from 60° to 90°, CAH from 10° to 30°, Δh from 0.1 to 0.4 mm, ψ from 0.5° to 4° and volume from 1 to 3 μL. All of the simulation cases are

tabulated in Appendix Bn B.2. It will be shown that a good agreement between the simulation and experimental data exists (see Figures 3.4, 3.5, 3.10).

For the simulations, a similar code to the one in Chapter Two was used (see Section C.1). Additionally, several parameters and functions were added to SE to simulate the compressing and stretching of the bridge. These additions are given in Appendix C.2.

3.3 Results and Discussions

An example of typical horizontal movement of the liquid bridge during the first loading cycle, from simulation and experiment, is provided in Figure 3.4. The surfaces have $\theta_a = 80.1°$, $CAH = 19.6°$, and $\psi = 2°$. The bridge is compressed and stretched for $\Delta h^* = 0.16$. In Figure 3.4a and 3.4b, respectively, the location of point C (X^*), and the evolution of θ_{1b} and θ_{2b} are shown versus h^*. Since ψ is smaller than ψ_c of the system ($\sim 12°$), the bridge is stable and its initial CAs are between θ_a and θ_r (Point A in Figure 3.4b). Four stages can be seen in Figure 3.4: first, at the beginning of compressing, the contact line remains pinned while θ_{1b} and θ_{2b} are increasing (from A-B). At this stage, since θ_{1b} and θ_{2b} are within the CAH interval, no horizontal movement of the contact line can be observed (X^* stays constant in Figure 3.4a). Second, θ_{1b} reaches θ_a earlier than θ_{2b}, and the bridge starts to move horizontally on its narrower end towards the cusp (B-C). In this stage, θ_{2b} remains less than θ_a, consequently, the contact line on the wider side of the bridge remains pinned while the narrower side is advancing (X^* increases in Figure 3.4a). Third, the bridge is stretched and the CAs decreases (C-D). Similar to the beginning of compressing, due to CAH, no horizontal movement occurs. And forth, when θ_{2b} reaches θ_r, the bridge starts to recede towards the surfaces' cusp, while the narrower side remains pinned (X^* increases again in Figure 3.4a).

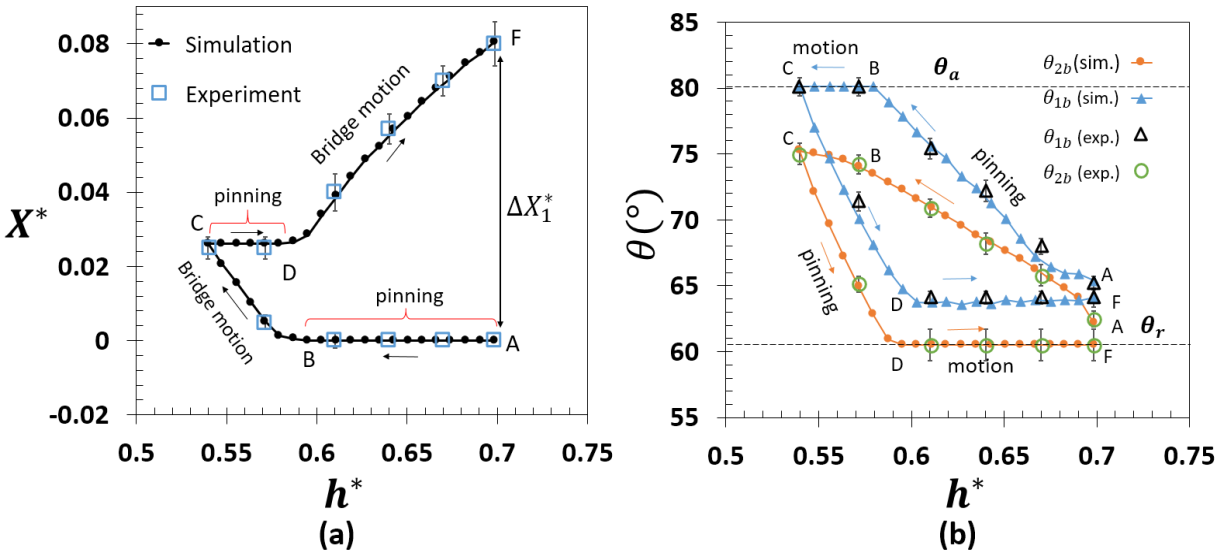

Figure 3.4 a) X^* versus h^* in the first loading cycle for a system with $\theta_a = 80.1°$, $CAH = 19.6°$, $\psi = 2°$, and $\Delta h^* = 0.16$. b) The evolution of θ_{1b} and θ_{2b} with h^* for the system in (a). Lines are to guide the eyes.

From the above example, we can see several key elements that govern the horizontal movement of the liquid bridge in a complete cycle. First, the range of h^* that corresponds to contact line pinning (i.e. A-B and C-D in Figure 3.4a, referred to as "pinning period" afterwards) can significantly influence the amount of horizontal motion the liquid bridge has in each loading cycle. Specifically, Δh^* needs to reach a certain minimum in order to depin the contact line and enable the horizontal motion. As such, the horizontal movement lags behind changes in the height at the beginning of compression (A-B), and at the beginning of stretching (C-D) stages. The lag is induced by CAH of the system. Next, in the period of horizontal movement (B-C and D-F), the sensitivity of the horizontal movement to the changes in the height (i.e. $|dX^*/dh^*|$) has two implications: First, a larger $|dX^*/dh^*|$ results in a larger amount of bridge movement. Second, for fixed incremental changes in h^*, a smaller $|dX^*/dh^*|$ reduces the size of X^* increments i.e., the

bridge can be moved with a higher precision when $|dX^*/dh^*|$ is smaller. Additionally, in the example in Figure 3.4, the depinning of the contact line is asymmetric, i.e., there is no advancing on the wider side, or receding on the narrower side. Such asymmetric depinning, however, is achievable only for a certain combinations of θ_a ,CAH, ψ and Δh^* values. Finally, while Figure 3.4 only shows the first loading cycle, the net movement of the liquid bridge in the subsequent loading cycles (ΔX_n^*) is also governed by these physical parameters.

To have good control of ΔX_n^* in practical applications, one needs to understand how ΔX_n^* is influenced by θ_a, CAH, ψ, and Δh^*. Several questions therefore arise: What is the minimum value of Δh^* required to initiate the horizontal movement (denoted as Δh_o^* hereafter), and how is Δh_o^* affected by θ_a, CAH, and ψ? How can $|dX^*/dh^*|$ be increased to enhance ΔX_n^*, or decreased to enhance the precision of movement? How can one prevent the liquid from advancing on the wider side, and receding on the narrower side? We start by addressing the effect of individual parameters on the horizontal movement during the first loading cycle. Potential implications of the findings in practical applications will be also discussed. An empirical equation for predicting Δh_o^* will be proposed, and the bridge motion during subsequent loading cycles will be provided at the end of the discussions.

3.3.1 Effects of the material parameters (CAH and θ_a) on ΔX_1^*

In the following discussion, we will show that using θ_a and CAH, one can influence the pinning period at the beginning of compressing and stretching stages, as well as $|dX^*/dh^*|$ during the period of movement. Consequently, the combination of these two factors allows for adjustment of ΔX_1^* (movement in the first loading cycle).

First, we will address the effect of CAH on ΔX_1^*. In Figure 3.5, the value of X^* versus h^* is plotted for the same system as in Figure 3.4, but with four different values of CAH (from simulation and experiments). All other parameters are fixed, so that the effect of CAH can be observed separately. It can be seen that, as CAH increases, it increases the pinning periods, in both compressing and stretching stages, and as a result, ΔX_1^* significantly decreases. Such increase in the pinning periods can be explained by looking at the distribution of CAs along the contact line at the beginning of the compressing and stretching stages. In Figure 3.6a, the distribution of CAs along the contact line of the bottom surface (versus the azimuthal angle, see Figure 3.6b) is shown just after the liquid bridge is formed. It can be seen that, as CAH is increased (i.e. θ_r is decreased), the local CAs of the bridge take values farther from θ_a ($= 80.1°$). Consequently, the amount of compression needed to push the CAs on the narrower side to θ_a increases. Similarly, at the beginning of stretching, with larger CAH the CAs lie farther from the receding angle, which increases the difficulty of depinning in the stretching stage as well (data is shown in Appendix Section B.4). Overall, one can reduce the pinning periods at the beginning of both compressing and stretching stages by reducing CAH, which consequently increases ΔX_1^*.

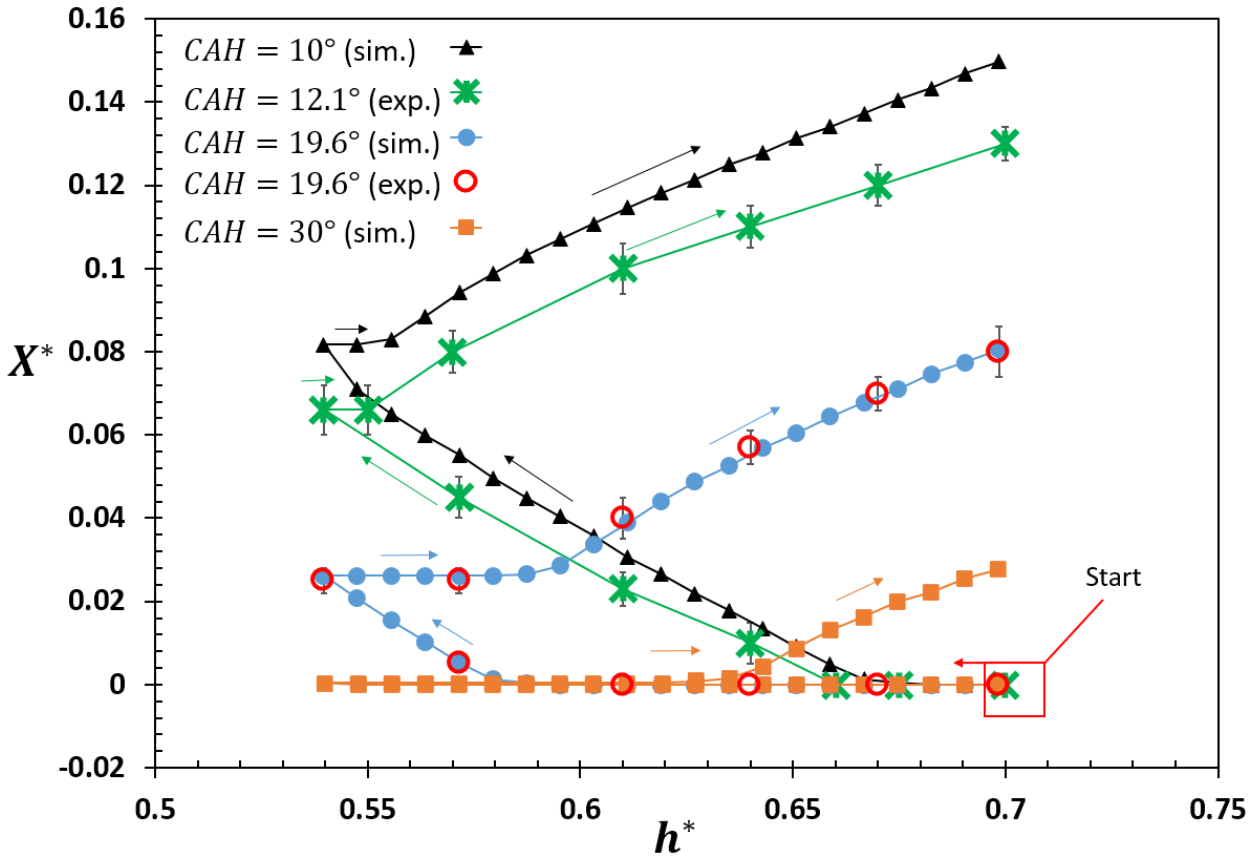

Figure 3.5 X^* versus h^* in the first loading cycle, for three systems with common $\theta_a = 80.1°$, $\psi = 2°$, and $\Delta h^* = 0.16$, but different CAH from 10° to 30° as well as a system with PEMA surfaces with $\psi = 2°$ and $\Delta h^* = 0.16$. Lines are to guide the eyes.

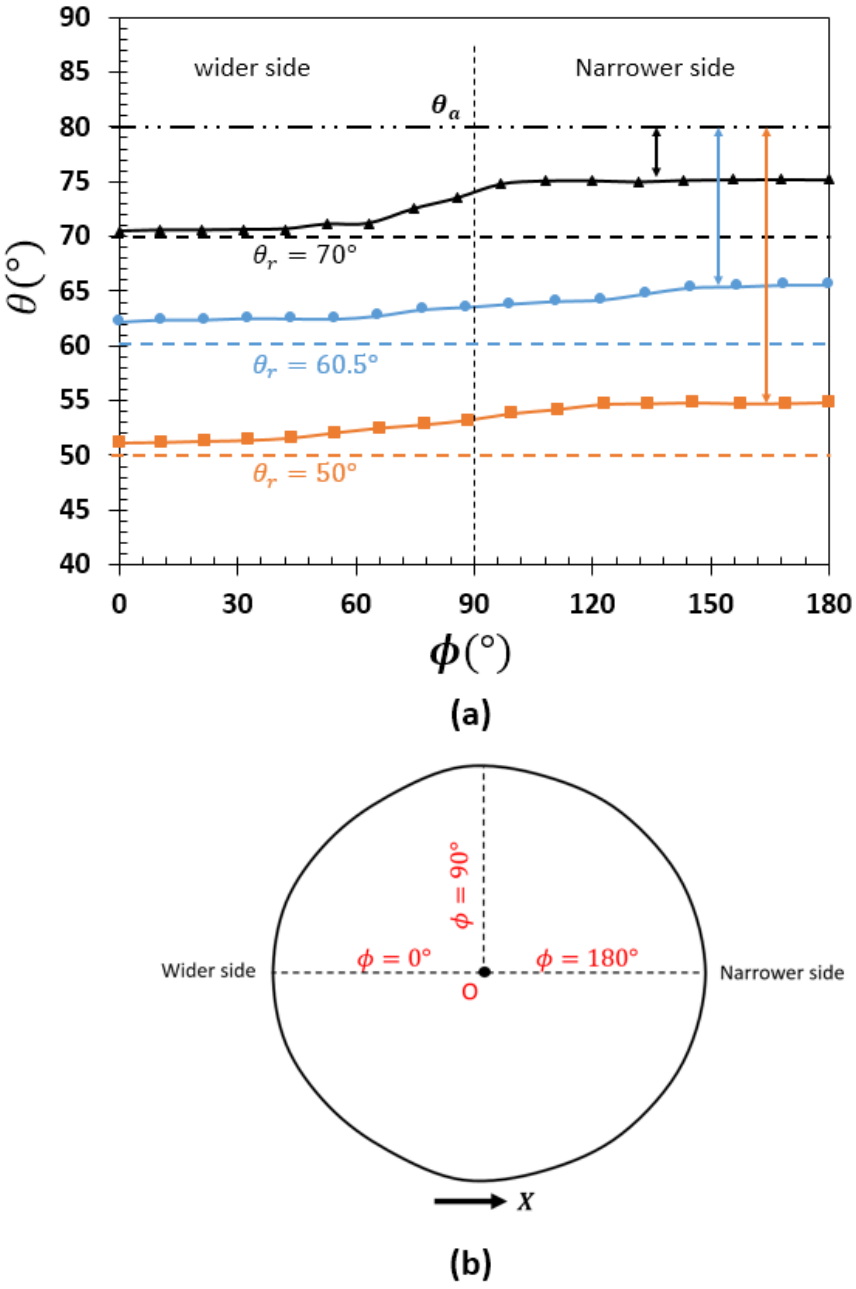

Figure 3.6 a) The value of CAs along the contact line on the bottom surface versus the azimuthal angle for the system in Figure 3.5, prior to the beginning of compression. Lines are to guide the eyes. b) The shape of the contact line on the bottom surface (simulation result for the system with $CAH = 20°$) prior to the start of compression. The azimuthal angle (ϕ) is measured from the wider side of the bridge using the centroid of the contact area as origin (O), i.e., $\phi(0°) = \theta_{2b}$.

It is clear from the discussion above that the depinning behavior depends on the value and distribution of the CAs along the contact line, which are not only controlled by CAH, but also by θ_a. In chapter two, it was shown that when θ_a is decreased while ψ and CAH are fixed, a larger difference between the CAs on the wider and narrower sides of the bridge (e.g. $\Delta\theta = \theta_{1b} - \theta_{2b}$ on the bottom surface) is needed for the bridge to maintain global force balance. The larger $\Delta\theta$ causes the CAs on the two sides to be closer to the boundary values (θ_r and/or θ_a); this will decrease the pinning period in the beginning of compression and stretching, leading to an increase in ΔX_1^*. For example, in Figure 3.7, X^* is plotted for three different systems (from simulation) with equal ψ, Δh^* and CAH, but different θ_a. As shown, decreasing θ_a,decreases the pinning period in both compressing and stretching stages, which leads to increase in ΔX_1^*.

Decreasing θ_a not only decreases the pinning periods, but also increases $|dX^*/dh^*|$ during the period of movement in both compressing and stretching (comparing the slopes of dash lines in Figure 3.7), which also promotes the increase in ΔX_1^*. This is because as θ_a decreases, the sessile drop forming the bridge sits lower on the bottom surface, which results in a smaller h_{ini} (see Figure 3.3a). Therefore, for a constant Δh^*, a liquid bridge formed between surfaces with smaller θ_a experiences a more confined space, compared to a bridge between surfaces with a larger θ_a. To comply with the constant volume constraint, the advancing and receding of the contact lines are hence more sensitive to the changes in height.

Given the discussion above, θ_a can be thought of as a parameter that can be used to modulate $|dX^*/dh^*|$ of the system. For example, if a smaller $|dX^*/dh^*|$ is desired to move the bridge with greater precision, θ_a can be increased to decrease $|dX^*/dh^*|$. However, as a byproduct, the pinning period will also increase. The increase in the pinning period can be compensated by decreasing the CAH of the surfaces, without affecting $|dX^*/dh^*|$ of the system (consulting Figure

3.5, where the slope of the curves is not affected by changes in CAH). This demonstrates the practicality of modifying the material parameters in controlling the horizontal movement.

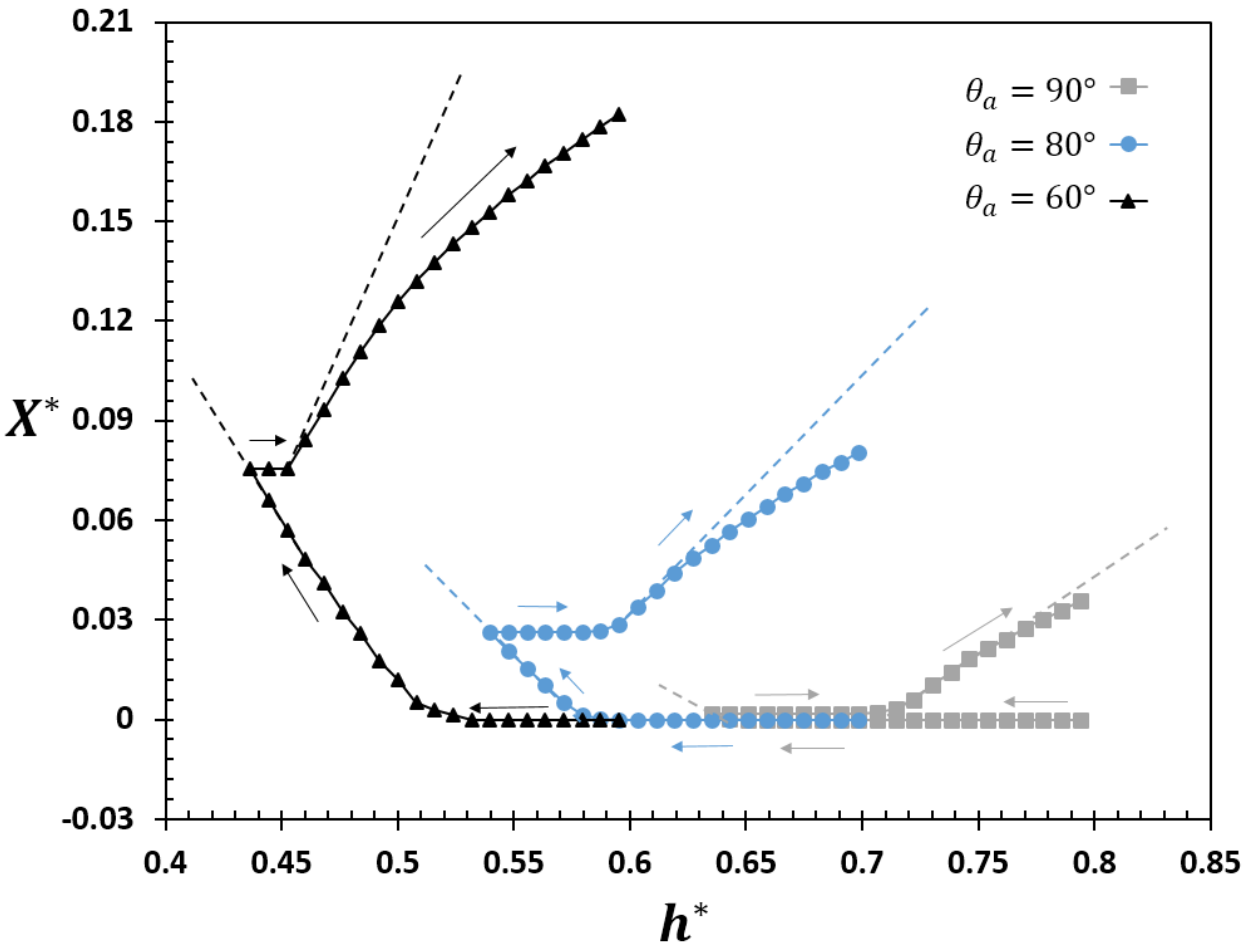

Figure 3.7 X^* versus h^* in the first loading cycle for three systems with common $CAH = 20°$, $\psi = 2°$ and $\Delta h^* = 0.16$, but different $\theta_a = 60, 80,$ and $90°$ (from simulations). Lines are to guide the eyes.

3.3.2 Effects of geometrical and mechanical parameters (ψ and Δh^*) on ΔX_1^*

Controlling the material parameters (θ_a and CAH) can be difficult in practice, and may not be practical in all applications. One can also influence the horizontal movement by varying ψ and Δh^*. Varying ψ has two main effects on the horizontal movement: First, it affects ΔX_1^* mainly by influencing the pinning periods, and second, it can be used to prevent the bridge from unfavorably

regressing backwards during the horizontal movement (i.e. advancing on the wider side in compressing, and/or receding on the narrower side in stretching). The effect of Δh^* on ΔX_1^* is also evident: it has to reach a minimum value to guarantee horizontal movement of the bridge during compressing and stretching. The influence of these two parameters are discussed below.

The effects of ψ will be addressed first. In Figure 3.8a, X^* versus h^* is plotted for three systems with equal θ_a, CAH and Δh^*, but different ψ between 2° and 4°. It can be seen that ΔX_1^* increases as ψ increases, mainly due to the reduction in the pinning period in both compressing and stretching stages. The effect of ψ on pinning can be explained by examining the distribution of CAs prior to the beginning of compression and stretching. For instance, in Figure 3.8b, the distribution of CAs along the contact line is shown for the same systems in Figure 3.8a (before any compressing). As ψ is increased, the gap between θ_a and the CAs on the narrow side decreases. This reduction decreases the needed Δh^* to push the contact angles on the narrower side to reach θ_a. Similarly, increasing ψ reduces the gap between θ_r and the CAs on the wide side of the bridge, which reduces the pinning period at the beginning of stretching stage (data shown in Appendix Section B.5).

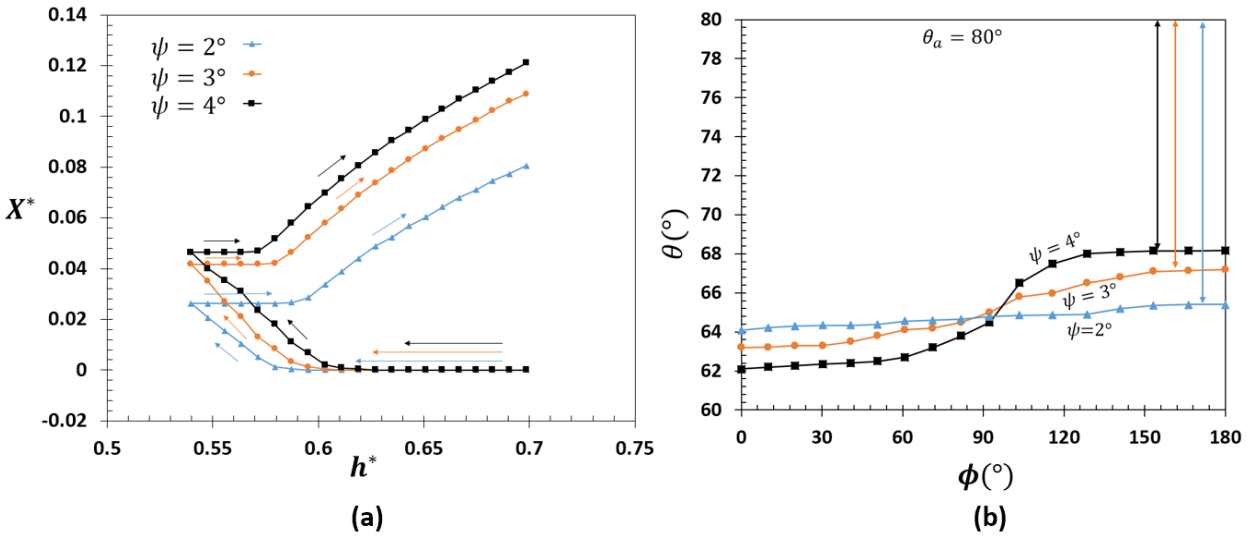

Figure 3.8 a) X^* versus h^* in the first loading cycle for three systems with common $\theta_a = 80°$, $CAH = 20°$ and $\Delta h^* = 0.16$, but different $\psi = 2°, 3°$, and 4°. b) the value of CAs along the contact line (versus ϕ) for the system in (a), prior to the beginning of compression stage. The critical angle of the system is $\psi_c \sim 12°$. Lines are to guide the eyes.

Increasing ψ also helps to prevent the bridge from regressing backward. Figures 3.9a and 3.9b show the evolution of the bridge's contact points on the wider and the narrower sides ($2b$ and $1b$ in Figure 3.3f), respectively. The system has $\theta_a = 60°$, $CAH = 20°$, and $\Delta h^* = 0.16$. At $\psi = 0.5°$, the bridge starts to undesirably advance away from the cusp on its wider side in the compression stage, and recede away from the cusp in the stretching stage. While, at $\psi = 2°$, the wider side remains pinned in the compression stage, and the narrower side remains pinned in the stretching stage. Considering the limiting case where $\psi = 0°$, the bridge is entirely axisymmetric, and the contact points on the two sides will have to advance or recede together during the loading cycle. Larger ψ brings greater asymmetry, i.e., more difference in CAs on the two sides (e.g. see Figure 3.8b) , so that one side can start moving well before the CA on the other side reaches the boundary values. This shows that increasing ψ can prevent backwards motion of bridge in loading cycles.

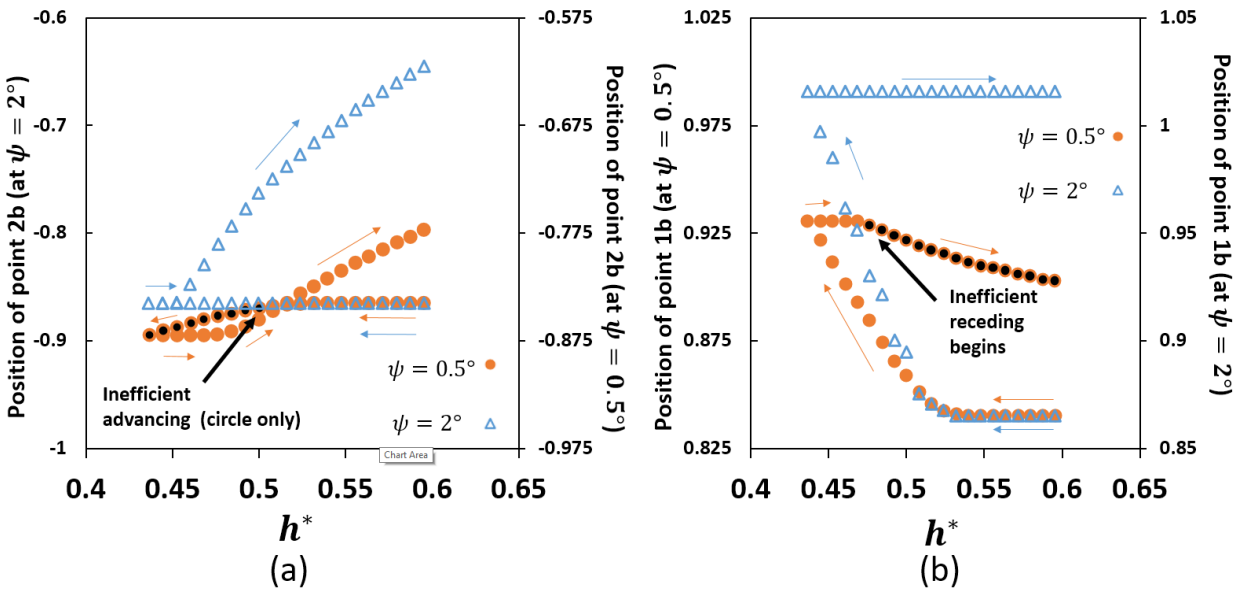

Figure 3.9 a) The evolution of contact point on the bottom surface for the wider side of the bridge in the first loading cycle (2b in Figure 3.3f). b) The evolution of contact point on the bottom surface for the narrower side of the bridge in the first loading cycle (2b in Figure 3.3f). The system has $\theta_a = 60°$, $CAH = 20°$, $\Delta h^* = 0.16$ (data from simulation). One system has $\psi = 0.5°$ (filled circles), and the other has $\psi = 2°$ (hollow triangles). The positive direction of X^* is towards right. To aid comparison, the X^* axis of both cases were shifted to have the same starting point. The cycles were filled with black when the inefficient advancing/receding occurred.

To understand the effect of Δh^* on ΔX_1^*, in Figure 3.10, for the same system in Figure 3.4, Δh^* was varied from 0.16 to 0.31 (results from both simulations and experiments). As Δh^* increases, ΔX_1^* increases for two main reasons. First, in the compression stage, the pinning period is equal for all the cases, hence the bridge with larger Δh^* will advance more towards the cusp after the movement is initiated. Second, due to larger confinement (i.e. reduction of h_{min}^*, see Figure 3.3c), the retreat of the contact line is more sensitive to the increase in height (i.e., $|dX^*/dh^*|$ increases, see the slopes of dash lines in Figure 3.10). This higher sensitivity also causes reduction in the pinning period at the beginning of the stretching stage, which also promotes the increase in ΔX_1^*.

Given the effects of ψ and Δh^* on the horizontal movement, the required Δh^* to achieve ΔX_1^* reduces, if ψ increases. Assume a situation where the horizontal motion of the bridge occurs with symmetrical depinning (i.e. having backwards motion). If ψ is sufficiently increased, first, it would prevent the backward motion of the bridge. Second, the pinning periods at the beginning of compressing and stretching stages decreases as ψ increases. These two factors reduce the required Δh^* to achieve ΔX_1^*.

So far we have addressed the effect of governing parameters on ΔX_1^* by changing only one of the parameters while keeping the others fixed. However, it should be emphasized that the effects of the parameters are not isolated, but rather interdependent (details can be found in Appendix Section B.6). For example, we have shown that the effect of ψ on ΔX_1^* is larger, when θ_a and/or CAH are smaller. Therefore, to maximize ΔX_1^*, one should reduce θ_a and CAH of the surfaces, (i.e. resulting in a larger $|dX^*/dh^*|$, smaller pinning periods, and a larger effect of ψ on ΔX_1^*) while increasing ψ and Δh^* in the system.

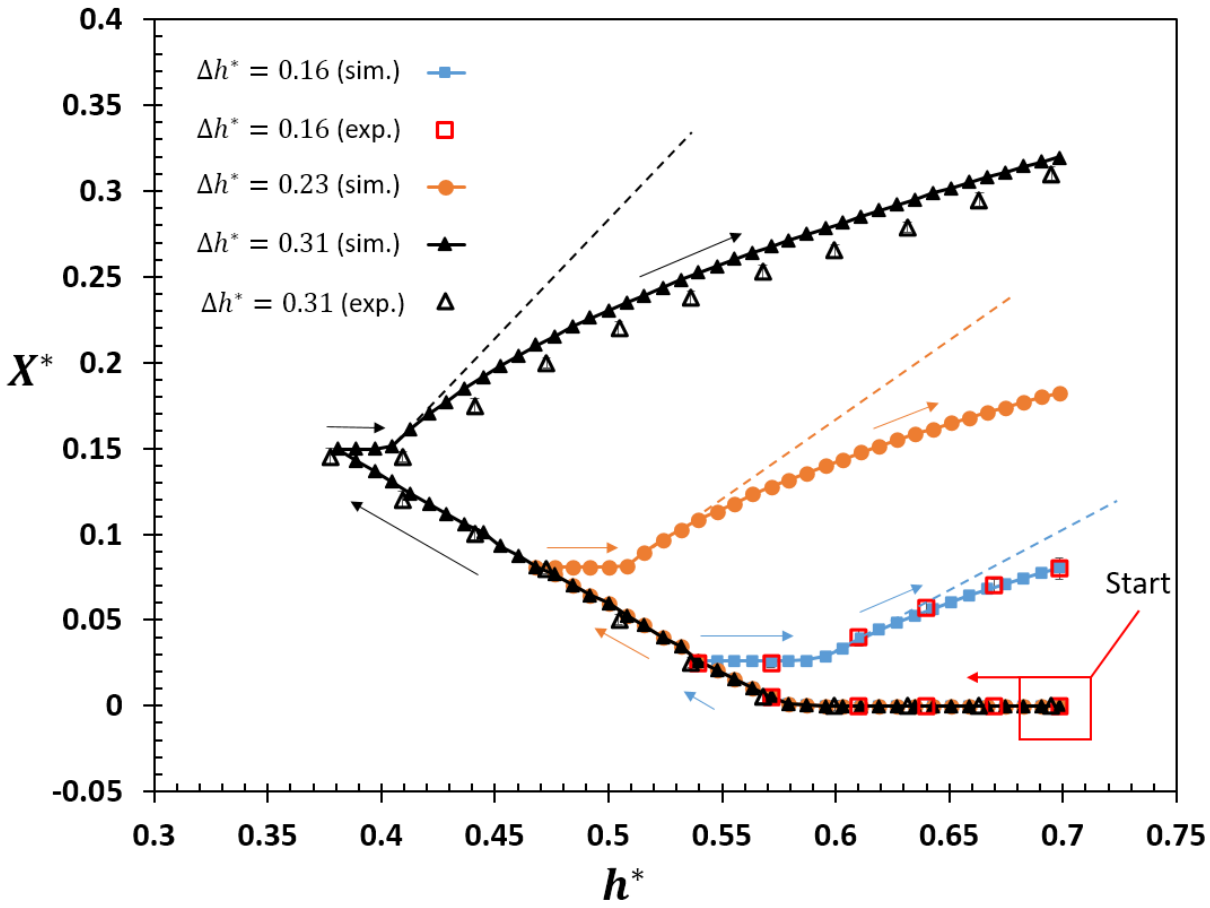

Figure 3.10 X^* versus h^* in the first loading cycle for the same system in Figure 3.4 but with three different $\Delta h^* = 0.16, 0.23$, and 0.31. Error bars for the experimental data are small and may not be visible. Lines are to guide the eyes.

3.3.3 Estimating Δh_o^*

As mentioned before, compressing and stretching the bridge causes motion, only if Δh^* reaches a certain minimum (Δh_o^*) to depin the contact lines. In a proper bridge motion, the depinning occurs on both top and bottom surfaces, and in both compressing and stretching stages. To achieve depinning in all of these situations, two considerations will be made on the definition of Δh_o^*: First, as mentioned earlier in "Methods and Materials", before the compression starts, the CAs on the bottom surface are smaller than that on the top surface, as a result, during compression the contact line depins earlier on the top surface compared to the bottom surface (see details in Appendix

Section B.3). Second, through the discussions, it became clear that the displacement of the top surface during contact line pinning is always smaller in the stretching stage than in the compressing stage (for example, see Figures 3.4-3.10). Considering these two points, Δh_o^* will be calculated only for the depinning of the contact line at the beginning of the compressing stage on the bottom surface (e.g. A-B in Figure 3.4). The calculated value will be a lower bound for Δh^* which also guarantees the depinning on the top surface and in stretching stage as well.

Mechanistically, the influences of wettability parameters on depinning of the liquid bridge share many similarities with their effect on the spontaneous (unstable) motion of the liquid bridge when $\psi > \psi_c$. Specifically, the resistance to the spontaneous motion towards the cusp is provided by CAH, which can be overcome when ψ is increased to the critical angle ψ_c of the system. Similarly, when $\psi < \psi_c$, the contact line pinning before liquid movement is also a result of CAH, and it can be overcome by compressing the bridge for Δh_o^*. Hence, $\psi_c - \psi$ can be thought of as a measure of resistance that needs to be compensated by Δh_o^*. Base on this, we hypothesize that, Δh_o^* should correlate positively with $\psi_c - \psi$. That is, θ_a and CAH are assumed to influence Δh_o^* through the value of $\psi_c - \psi$.

To test this hypothesis, we considered all the simulation data and found that a linear relationship between Δh_o^* and $\psi_c - \psi$ exists, which can be described by the empirical equation given in Eqn. (3.1). To test the viability of Eqn. (3.1), values of Δh_o^* from the experimental data were not included in the fitting of Eqn. (3.1), so that they can be used as independent tests for Eqn. (3.1). In Figure 3.11, the values of Δh_o^* from the experiments were compared to the corresponding ones calculated from Eqn. (3.1). Data points calculated from Eqn. (3.1) (i.e. the $45°$ line) fall within the standard error (i.e. shown with error bars) of the experimental data. This implies that there is a good agreement between Δh_o^* calculated from Eqn. (3.1) and the experimental data.

$$\Delta h_o^* = 0.011(\psi_c - \psi) \tag{3.1}$$

The value of ψ_c in Eqn. (3.1) can be calculated from the empirical equation given in Eqn. (3.2). All the angles in Eqns. (3.1) and (3.2) are in degrees.

$$\psi_c = 0.044\theta_a^{1.535}(\cos(\theta_a - CAH) - \cos(\theta_a)) \tag{3.2}$$

In practice, ψ should be less than ψ_c calculated from Eqn. (2) to maintain stability of the liquid bridge. Additionally, systems should satisfy $\Delta h^* > \Delta h_o^* = 0.011(\psi - \psi_c)$ to ensure that the bridge can be moved in both compressing and stretching stages, and on both top and bottom surfaces.

Since equation (1) calculates the amount of the pinning period at the beginning of the compressing stage, it in fact quantifies the initial lag of the motion in response to the change in h^*. Therefore, Eqn. (1) can be thought as a tool that allows one to gauge the initial lag of the motion as well.

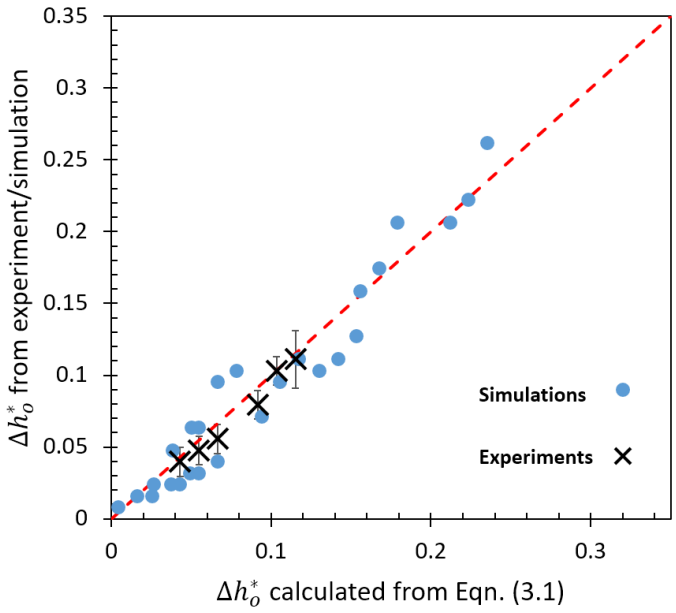

Figure 3.11 Comparison between ψ_c calculated from Eqn. (3.1) (horizontal axis) and the corresponding simulation and experimental data (vertical axis). The red dashed-line is the 45° line.

3.3.4 Multiple Loading Cycles

So far we have focused on discussing the horizontal movement of the bridge during the first loading cycle. In Figure 3.12, values of ΔX_n^* (for $n = 1$ to 5) are given for a bridge between PMMA surfaces with $\psi = 2°$, and $\Delta h^* = 0.31$. Results are from experiment and simulation. At each data point, if asymmetric depinning occurs, it will be labeled with A.D.; if depinning occurs on both sides of the bridge, it will be labeled with S.D. (symmetric depinning). Two observations can be made here. First, for small Δh^*, as n increases the bridge progresses from having A.D. to having S.D. Secondly, together with the change in the depinning characteristics, the trend of ΔX_n^* also varies: with A.D. ΔX_n^* increases as n increases, while it starts to decrease with n in presence of S.D.

The two observations can be explained by noting that as the bridge moves horizontally, it gets closer to the cusp of the surfaces and therefore becomes more confined. Thus, while it is possible

to achieve A.D. in the first few cycles, for the same Δh^*, the bridge in the later cycles has been squeezed so much that S.D. starts to take place. In the case of A.D., considering that the bridge only expands and retreat in one direction, the closer the bridge gets to the cusp, the further it has to move towards the cusp in one loading cycle to accommodate the same amount of liquid between the surfaces. Thus, ΔX_n^* increases as n increases. This is not necessarily true, if the horizontal movement becomes S.D.; the liquid also regress away from the cusp in S.D. which causes ΔX_n^* to decrease as n further increases.

A similar trend can also be seen for systems with different wettability parameters. For example, in Figure 3.13a, values of ΔX_n^* (for $n = 1$ to 5) are given for three systems with common $\theta_a = 60°$, $CAH = 20°$, $\psi = 2°$, and different Δh^* ($= 0.16$ to 0.31), where results are from simulation. Similarly, the two observations explained above can be seen in Figure 3.13a. Furthermore, it can be understood that as Δh^* increases, the number of cycles with A.D. decreases. To explain this observation, one should consider that the horizontal movement of the bridge is much larger when Δh^* is larger, hence the bridge gets closer to the cusp and experiences more confinement with smaller number of cycles. For example, from Figure 3.13b, it can be seen that, for the system with $\Delta h^* = 0.16$, the value of $\sum_1^n X_n^*$ (total distance traveled after *n* cycles) at $n = 3$ is still smaller than ΔX_1^* of the system with $\Delta h^* = 0.31$. The system with smaller Δh^* remains efficient (presence of A.D.) for a larger number of cycles, at the price of moving for a smaller distance.

As it was mentioned in Section 3.1, Luo *et al.* [7] showed that after each loading cycle, ΔX_n continuously increases. This is true before the transition of the horizontal movement from A.D. to S.D. However, as S.D. appears, the distance traveled by the bridge decreases as n increases. This also explains the experimental results of Prakash *et al.* [8]; in their system, the bridge movement occurred with S.D., hence, ΔX_n was decreased as n was increased.

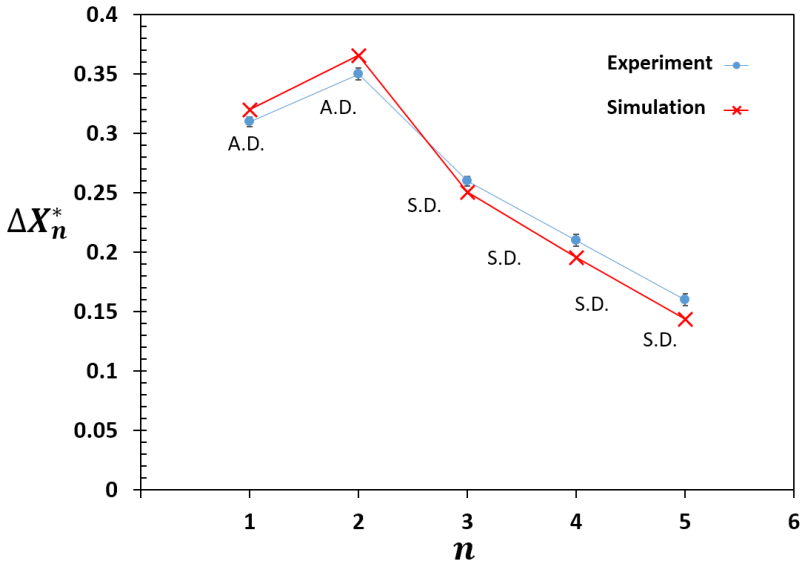

Figure 3.12 The net movement of a bridge between PMMA surfaces ($\theta_a = 80.1°$ and $CAH = 19.6°$) in each loading cycle (i.e. ΔX_n^*) with $\psi = 2°$ and $\Delta h^* = 0.31$. Data from experiment and simulation.

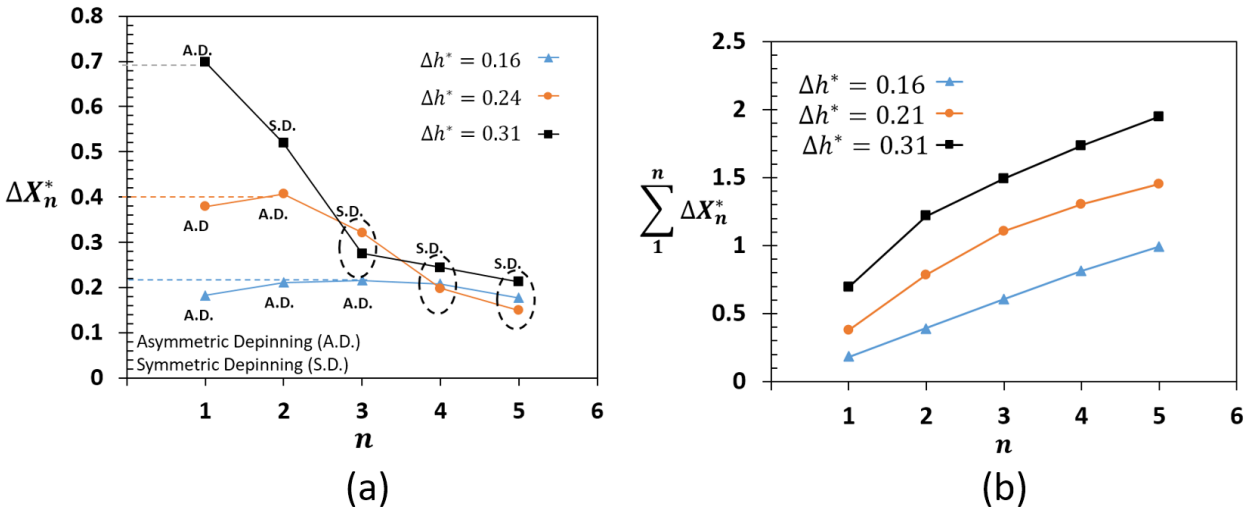

Figure 3.13 a) The net movement of the bridge in each loading cycle (i.e. ΔX_n^*) for three systems with common $\theta_a = 60°$, $CAH = 20°$ and $\psi = 2°$ but three different Δh^* from 0.16 to 0.31. b) The total movement of the bridge in loading cycles for the systems in Figure 3.12a. Lines are to guide the eyes.

Chapter Four: Conclusions and Future Prospects

4.1 Conclusions

Experimental and numerical approaches as well as theoretical reasoning were used to study the stability of liquid bridges between two identical nonparallel hydrophilic surfaces. When the dihedral angle between the two surfaces (ψ) is above a critical value ψ_c, the bridge exhibits spontaneous movement towards the cusp of the surfaces after its formation. It was shown that the critical angle only depends on θ_a, CAH and the initial contact angle of the sessile drop (θ_{ini}), such that it can be increased by increasing each of these parameters. Under the condition that $\theta_{ini} = \theta_a$, it was shown that the influence of CAH on ψ_c is stronger at larger θ_a, and the influence of θ_a on ψ_c is also stronger at larger CAH. An empirical equation in the form of $\psi_c = 0.044\theta_a^{1.535}(\cos(\theta_a - CAH) - \cos(\theta_a))$ was proposed to predict the stability of a bridge with $\theta_{ini} = \theta_a$. The equation is applicable for bridges formed by moving down a top surface toward a sessile drop; whether the top surface is pre-tilted, or parallel when the bridge is formed, and then tilted around its center. If $\theta_{ini} < \theta_a$, the empirical function provides an upper bound for ψ_c.

Bulk motion of a liquid bridge between nonparallel hydrophilic surfaces undergoing cyclic compressing and stretching was investigated numerically and experimentally. The effects of the amount of compressing and stretching (Δh), ψ, θ_a and CAH on the bulk motion were investigated. We found that the magnitude of motion can be increased by increasing ψ and Δh and/or by decreasing θ_a and CAH and the precision of the motion can be controlled by θ_a and CAH. The minimum amount of Δh needed to initiate the horizontal motion in both compressing and stretching stages, and on both top and bottom surfaces (i.e. Δh_o^*) was found to be linearly dependent on $\psi - \psi_c$. An empirical equation in the form of $\Delta h_o^* = f(\psi, \psi_c)$ was proposed to calculate Δh_o^* .

The behavior of the liquid bridge under multiple compressing and stretching loading cycles was studied as well. The magnitude of the motion (in one loading cycle) was seen to increase after each loading cycle, if the contact lines depinned only on the narrower side during compressing, and on the wider side during stretching (asymmetric depinning). If the depinning occurred on both side of the bridge (symmetric depinning), the magnitude of bridge motion in one cycle decreased after each loading cycle. A symmetric depinning situation can be turned into a more desirable asymmetric depinning (preventing backwards motion of the bridge) by increasing ψ in the system.

4.2 Future Prospects

In this thesis, the reported results were based on using two identical hydrophilic surfaces e.g., the empirical equation $\psi_c = f(\theta_a, CAH)$ is only useful when the surfaces are identical and hydrophilic. This condition may not be applicable in all situations. Therefore, it is recommended to expand the results to cover the behavior of liquid bridges between identical hydrophobic (surfaces with $\theta_a > 90°$) surfaces, and also between non-identical surfaces which may be hydrophobic or hydrophilic.

In the quasi-static regime, one can still use the same Surface Evolver simulation given in this work to cover the behavior of the bridge between non-identical surfaces. This can be done by only changing the contact angle parameters for one of the surfaces (i.e. see Section C.1). The Surface Evolver simulation can also be used to study the behavior of the bridge when surfaces are hydrophobic, as there is no restriction on using surfaces with $\theta_a > 90°$ in the simulation. However, the simulation results have to be revalidated by doing experiments for the new studies. We recommend to study the behavior of the bridge between identical hydrophobic surfaces first, before expanding the study to non-identical surfaces. Once the behavior of the bridge between identical hydrophobic surfaces is understood, one can better understand the behavior of the bridge between

non-identical surfaces (hydrophilic or hydrophobic) based on the bridge behavior between identical surfaces.

Bibliography

(1) R. Dangla, S. C. Kayi C.; N. Baroud, Droplet Microfluidics Driven by Gradients of Confinement, Proc. Natl. Acad. Sci., **2013**, 110, 853–858.

(2) Burns MA, Mastrangelo CH, Sammarco TS, et al. Microfabricated structures for integrated DNA analysis. Proc. Natl. Acad. Sci., **1996**, 93, 5556-5561.

(3) Heng, X. & Luo, C. Bioinspired plate-based fog collectors. *ACS* Appl. Mater. Interfaces **2014**, 6, 16257–16266.

(4) E. Pierce, F. J. Carmona, A. Amirfazli, "Understanding of Sliding and Contact Angle Results in Tilted Plate Experiments", Colloids Surfaces A, **2008**, 323, 73-82.

(5) Velev O.D., Prevo B.G., Bhatt K.H. On-chip manipulation of free droplets. Nature **2003,** 426, 515–516.

(6) Chen, Z. H. & Utaka, Y. Characteristics of condensate drop movement with application of bulk surface temperature gradient in Marangoni dropwise condensation. Int. J. Heat Mass Tran. **2011**, 54, 5049–5059.

(7) Luo, C., Heng, X. & Xiang, M. M. Behavior of a liquid drop between two nonparallel plates. Langmuir **2014**, 30, 8373–8380.

(8) Prakash, M., Quéré, D. & Bush, J. W. M. Surface tension transport of prey by feeding shorebirds-the capillary ratchet. *Science* **2008**, 320, 931–934.

(9) Chen, H.; Tang, T.; Amirfazli, A. Fast Liquid Transfer between Surfaces: Breakup of Stretched Liquid Bridges. Langmuir **2015**, 31, 11470–11476.

(10) Chen, H.; Tang, T.; Amirfazli, a. Liquid Transfer Mechanism between Two Surfaces and the Role of Contact Angles. Soft Matter **2014**, 10, 2503–2507.

(11) Chen H., Tang T., Amirfazli A. Effects of Surface Wettability on Fast Liquid Transfer. Phys. Fluids **2015**, 27, 112102.

(12) Xu, W.; Lan, Z.; Peng, B.; Wen, R.; Chen, Y.; Ma, X. Directional Movement of Droplets in Grooves: Suspended or Immersed? Sci. Rep. **2016**, 6, 18836.

(13) Baratian, D.; Cavalli, A.; van den Ende, D.; Mugele, F. On the Shape of a Droplet in a Wedge: New Insight from Electrowetting. Soft Matter **2015**, 11, 7717–7721.

(14) Concus, P.; Finn, R. On the Behaviour of Capillary Shapes in the Wedge. Proc. Natl. Acad. Sci. **1969**, 63, 292–299.

(15) Concus, P.; Finn, R. Discontinuous Behavior of Liquids between Parallel and Tilted Plates. Phys. Fluids **1998**, 10, 39-43.

(16) Wang, L., Wu, H., Wang, F. Efficient transport of droplet sandwiched between saw-tooth plates, J. of Colloid and Interface Sci. **2016,** 462, 280-287.

(17) Fortes, M. Axisymmetric Liquid Bridges between Parallel Plates. J. Colloid Interface Sci. **1982**, 88, 338-352.

(18) Prabhala, B. R.; Panchagnula, M. V.; Vedantam, S. Three-Dimensional Equilibrium Shapes of Drops on Hysteretic Surfaces. Colloid Polym. Sci. **2012**, 291, 279–289.

(19) Buckingham, E. On Physically Similar Systems; Illustrations of the Use of Dimensional Equations. Phys. Rev. **1914**, 4, 345–376.

(20) Chen, H.; Tang, T.; Amirfazli, A. Fabrication of Polymeric Surfaces with Similar Contact Angles but Dissimilar Contact Angle Hysteresis. Colloids Surfaces A. **2012**, 408, 17–21.

(21) Chau, T. A Review of Techniques for Measurement of Contact Angles and Their Applicability on Mineral Surfaces. Miner. Eng. **2009**, 22, 213–219.

(22) Brakke, K. The Surface Evolver. Exp. Math. **1992**, 1, 141-165.

(23) Brakke, K. Surface Evolver Manual. Math. Dep. Susquehanna University, **1994**.

(24) Collicott, S.; Weislogel, M. Computing Existence and Stability of Capillary Surfaces Using Surface Evolver. AIAA J. **2004**, 42, 289-295.

(25) Brakke, K. The Surface Evolver and the Stability of Liquid Surfaces. Trans. R. Soc. **1996**, 354, 2143-2157.

(26) Prabhala, B. R.; Panchagnula, M. V.; Vedantam, S. Three-Dimensional Equilibrium Shapes of Drops on Hysteretic Surfaces. Colloid Polym. Sci. **2012**, 291, 279–289.

(27) Santos, M. J.; White, J. A. Theory and Simulation of Angular Hysteresis on Planar Surfaces. Langmuir **2011**, 27, 14868–14875.

(28) Chen, T.; Tsamopoulos, J. A.; Robert, J. G. Capillary bridges between parallel and non-parallel surfaces and their stability. J. Colloid Interface Sci. **1992**, 151, 49-69.

Appendices

A: Supporting Information for Chapter Two

A.1: Surface fabrication methods

Table A.1 shows the details of the materials and methods used to fabricate each of the surfaces specified in Table 2.1. Except silicon, Fisher microscope glass slides were used as the substrate in spin coating. Before the coating process, the glass slides were cleaned by ultrasonic cleaning (in water). After ultrasonic cleaning, the glass slides were cleaned with distilled water and Acetone.

Table A.1 Technical information on the fabrication of surfaces.

Surface	Fabrication Method	Material used
Silicon	N/A	100mm (orientation) Silicon wafer from Silicon Valley Microelectronics, Inc.
PMMA(1)	Spin coat Spin speed: 1000 RPM Spin duration: 60s	Solution used: 2wt% of PMMA (Aldrich Mw~120000), toluene was used as the solvent
PMMA(2)	Spin coat Spin speed: 2000 RPM Spin duration: 60s	Solution used: 0.2wt% of PMMA (Aldrich Mw~120000), toluene was used as the solvent
PEMA	Spin coat Spin speed: 2000 RPM Spin duration: 60s	Solution used: 1wt% solution of Poly (ethyl methacrylate), (Aldrich Mw~515,000), toluene was used as the solvent
PS	Spin coat Spin speed: 2000 RPM Spin duration: 60s	Solution used: 1wt% solution of Polystyrene, (Aldrich Mw~35,000), toluene was used as the solvent

A.2: Comparing the shapes of the liquid bridge obtained from the experiments and from simulations

Figure A.1 shows the ten parameters (six contact angles (CA) and four contact line widths) measured from the experiments by the front view (Figure A.1a) and side view (Figure A.1b) cameras.

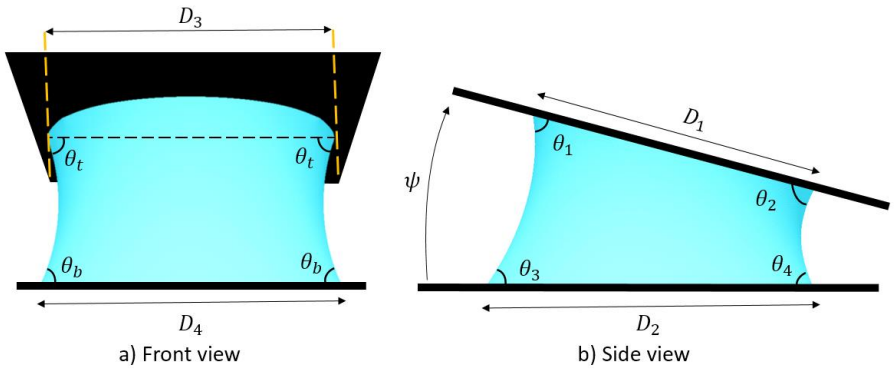

Figure A.1 a) Parameters measured from the front view camera: D_3 and D_4 are contact line widths on the top and bottom surfaces, respectively; θ_t and θ_b are the CAs on the top and bottom surfaces, respectively. b) Parameters measured from the side view camera: D_1 and D_2 are contact line widths on the top and bottom surfaces, respectively; θ_1 and θ_2 are respectively the CAs at the wide and narrow ends on the top surface. Similarly, θ_3, and θ_4 are respectively the CAs at the wide and narrow ends on the bottom surface.

The percentage error between the data measured from the experiments and the simulations data is calculated according to Eqn. (A.1), where X is the "true" value taken to be the average obtained from three experiments, and X' is the value obtained from simulation. The value of error was compared to the percentage coefficient of variation (C.V.) (i.e. relative standard deviation) of the three experiments which allows us to examine if the discrepancy between simulation and experimental results is reasonable.

$$error = \frac{|X - X'|}{X} * 100 \quad \text{(A.1)}$$

Tables A.2 and A.3 compare the calculated percentage error and C.V. of the variables from the side view and front view cameras, respectively. It can be seen that for all the variables, the errors of the simulation data from the experimental mean have the same order of magnitude as the percentage C.V. of the experiments. Therefore, the experimental and simulation data agree well.

Table A.2 Calculated percentage error of the simulations (the first row, white, for each surface) and percentage C.V. of the three identical experiments (the second row, shaded, for each surface), for each of the variables observable from the side view camera.

#	Surface	ψ	θ_1 error %	θ_2 error %	θ_3 error %	θ_4 error %	D_1 error %	D_2 error %
			θ_1 C.V. %	θ_3 C.V. %	θ_5 C.V. %	θ_7 C.V. %	D_1 C.V. %	D_2 C.V. %
1	Silicon	3	3.2%	1.2%	1.6%	2.2%	1.6%	1.8%
			3.7%	3.8%	3.5%	5.6%	5.8%	6.7%
2	PMMA 1	3	0.4%	2.6%	2.8%	2.1%	0.0%	3.9%
			1.8%	3.7%	3.4%	4.8%	1.5%	4.2%
3	PMMA 1	5	1.5%	3.5%	1.8%	2.5%	1.8%	6.2%
			5.5%	5.7%	3.5%	4.6%	4.1%	4.5%
4	PMMA 2	3	1.3%	2.5%	5.2%	6.8%	7.6%	5.5%
			3.7%	3.4%	3.6%	4.2%	6.1%	4.4%
5	PEMA	3	4.5%	2.0%	5.2%	1.7%	2.2%	6.8%
			2.1%	4.6%	3.8%	3.6%	3.1%	3.5%
6	PS	3	0.2%	2.4%	1.2%	0.9%	13.0%	8.5%
			2.7%	2.3%	2.0%	4.5%	4.5%	6.6%
7	PS	6	8.3%	1.9%	5.0%	0.2%	1.8%	11.7%
			3.7%	3.7%	3.5%	4.4%	3.5%	2.6%
8	PS	8.8	2.4%	1.6%	2.2%	1.0%	1.1%	9.1%
			1.5%	5.6%	4.5%	3.9%	2.9%	4.1%

Table A.3 Calculated percentage error of the simulations (the first row, white, for each surface) and percentage C.V. of the three identical experiments (the second row, shaded, for each surface), for each of the variables observable from the front view camera.

#	Surface	ψ	θ_t error %	θ_b error %	D_3 error %	D_4 error %
			θ_t C.V.%	θ_b C.V.%	D_3 C.V.%	D_4 C.V.%
1	Silicon	3	1.6%	2.2%	1.5%	2.8%
			2.1%	1.3%	2.5%	1.1%
2	PMMA 1	3	0.1%	2.6%	2.1%	3.9%
			3.6%	2.4%	3.3%	3.0%
3	PMMA 1	5	0.7%	0.8%	4.6%	4.0%
			2.8%	2.7%	2.7%	3.1%
4	PMMA 2	3	1.6%	0.9%	3.5%	3.5%
			2.8%	3.4%	3.7%	3.6%
5	PEMA	3	0.5%	1.1%	2.5%	5.8%
			2.0%	2.1%	3.4%	2.6%
6	PS	3	3.1%	0.8%	5.3%	9.9%
			2.4%	2.5%	3.2%	3.6%
7	PS	6	5.5%	0.6%	1.2%	9.8%
			3.7%	2.6%	2.9%	3.5%
8	PS	8.8	0.5%	1.8%	3.2%	8.1%
			3.9%	4.2%	4.5%	2.6%

In addition to the error values given in Tables A.2 and A.3, Figure A.2 shows a direct comparison between the shapes of the bridge obtained from the experiments (from both side-view and front-view cameras) and those from identical simulations, for cases 4, 5 and 8 in Table A.2 and A.3. The comparisons were done by overlaying a semi-transparent image of the bridge from the simulation (blue colored) on the image of the bridge obtained from the experiments. A very good agreement between the SE and the experimental results can be seen from Figure A.2.

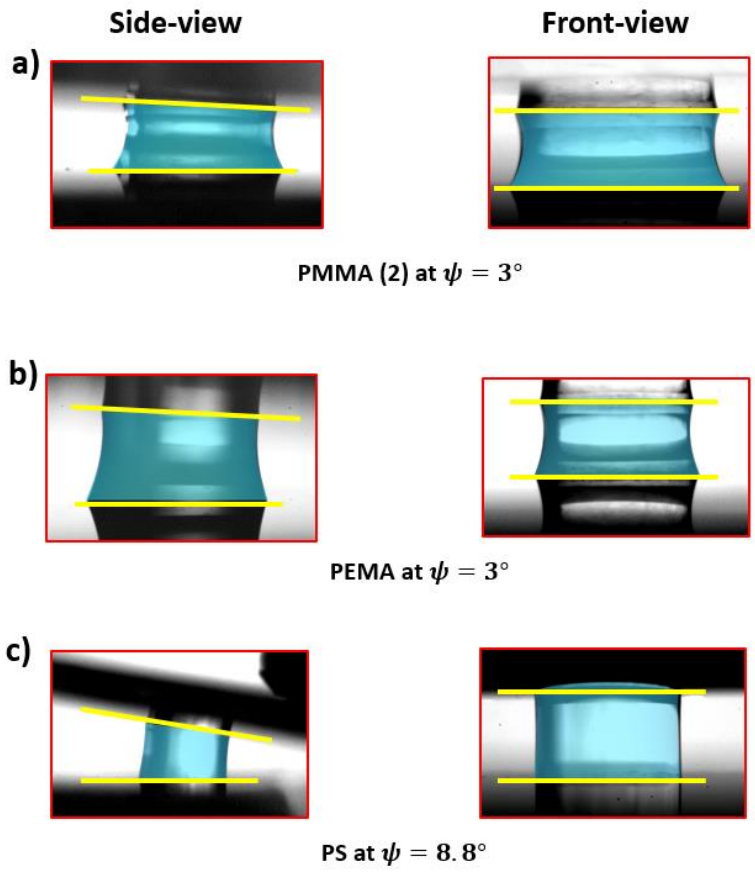

Figure A.2 Direct comparison between the shapes of the bridge obtained from simulations (blue semi-transparent) and those from the experiments (experiment images in the background). Left panel: side-view images, Right panel: front-view images.

A.3: Comparison between ψ_c obtained from experiments and from simulations

The comparison between ψ_c obtained from experiments and from identical simulations is shown in Figure A.3. Each case number refers to the surface numbered in Table 2.1. The error in the experimental data are $\pm 0.2°$ for each data point. As can be seen, the results from the simulations and experiments are in good agreement.

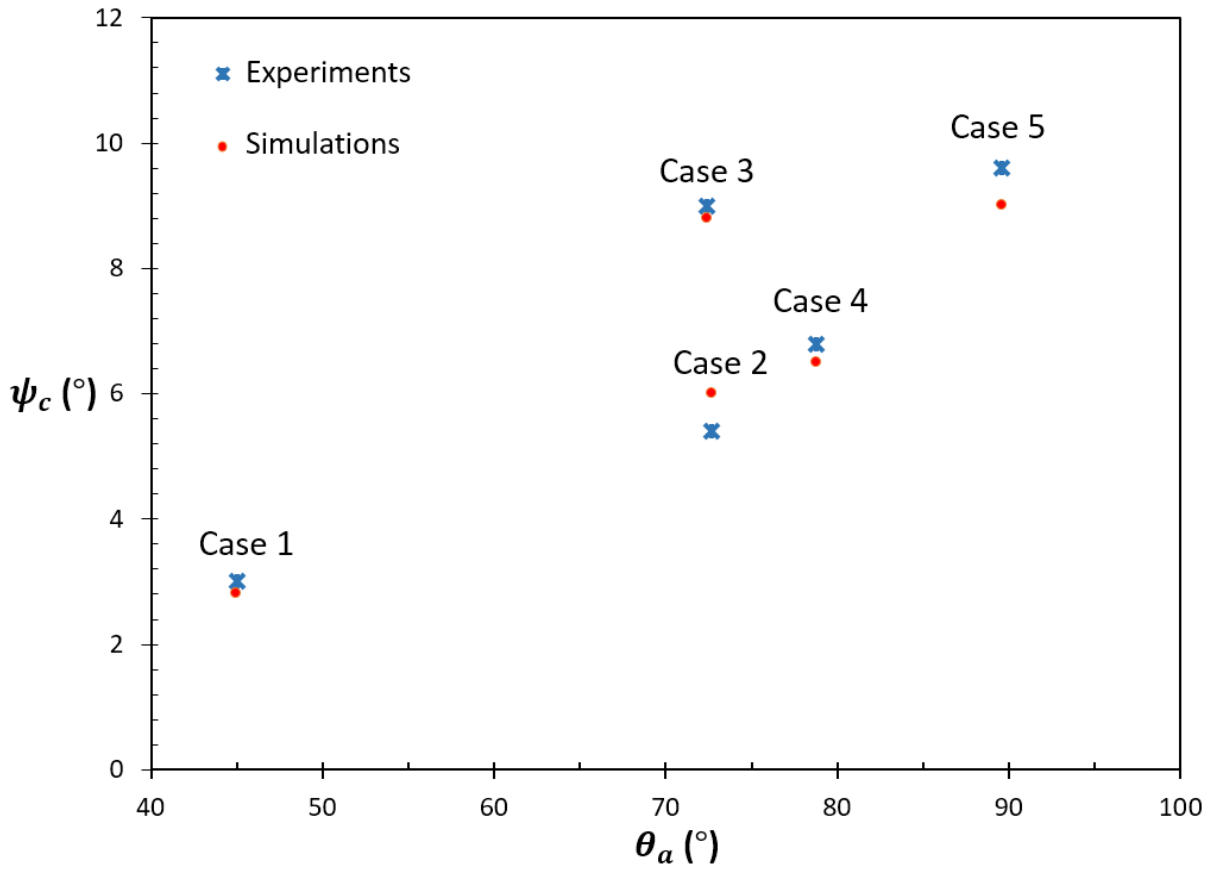

Figure A.3 Comparison between simulation and experimental results. The errors in the experimental data are $\pm 0.2°$.

A.4: Justifying the assumption that $R_{1t} = R_{2t}$

To illustrate the viability of the assumption that $R_{1t} = R_{2t}$, the out-of-plane curvatures were calculated using Surface Evolver for two pairs of surfaces at $\psi = 3°$ and $6°$. System S1 has $\theta_a = 60°$ and $CAH = 20°$, and system S2 has $\theta_a = 90°$ and $CAH = 10°$. The out-of-plane curvatures were calculated at points a_1 and a_2 which are, respectively, the intersection points of the rightmost and the leftmost menisci with a line passing through the surfaces' cusp and having an angle of ω with the bottom surface (see Figure A.4). In Figure A.5, the ratio of $\varepsilon = R_{2t}/R_{1t}$ versus ω are shown. It can be seen that for all ω, ε differs from one by less than 10%, hence, assuming $R_{1t} = R_{2t}$ is reasonable. This is also confirmed for all the bridges studied in the paper (data not shown).

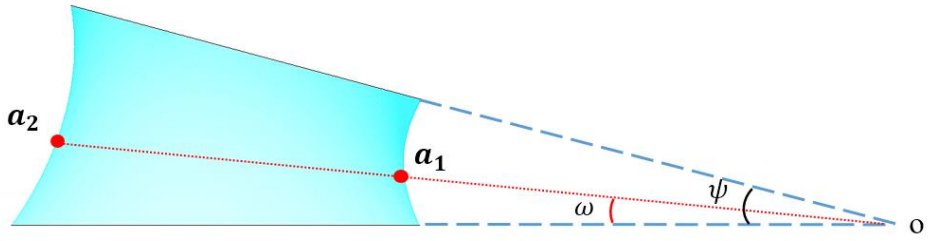

Figure A.4 Points a_1 and a_2 are, respectively, the intersection points of the rightmost and leftmost menisci with the dotted red line passing through the surfaces' cusp and having an angle of ω with the bottom surface.

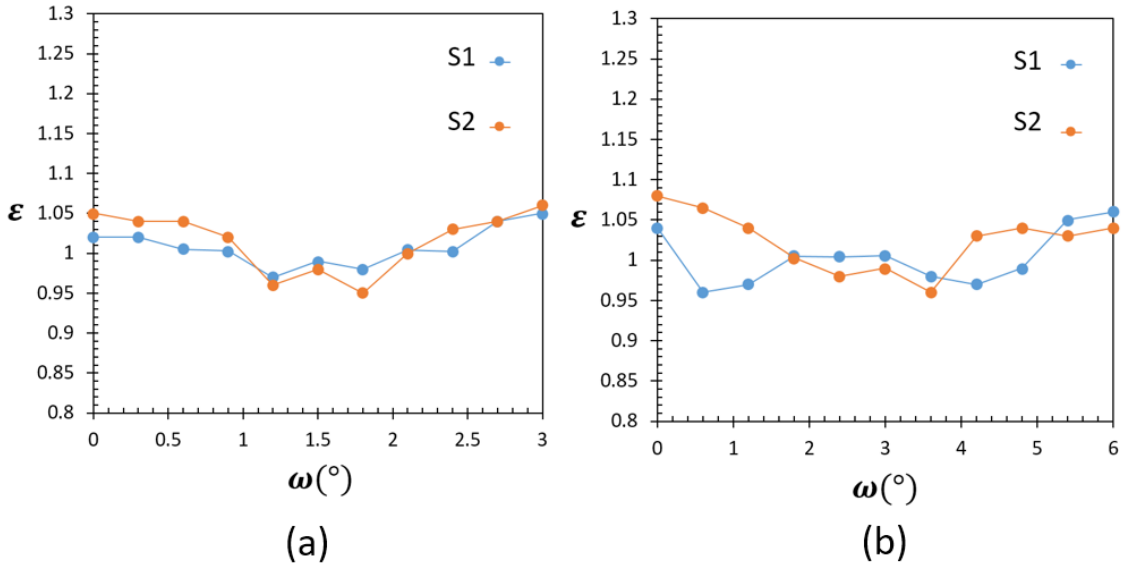

Figure A.5 a) $\varepsilon = R_{1t}/R_{2t}$ versus ω for systems S1 and S2 at $\psi = 3°$. b) ε versus ω for systems S1 and S2 at $\psi = 6°$.

A.5: Scaling of lengths with respect to liquid volume

A system is said to scale with liquid volume (V), if $\sqrt[3]{V}$ can be considered as the characteristic length of the system and all the lengths in the system are proportional to it. Such linear scaling preserves angles and proportions as V varies. A bridge system that scales will behave the same independent of V. Below, we will present the conditions required for the lengths of the liquid

bridge to scale with $\sqrt[3]{V}$. In the discussion, we will assume the Bond number to be sufficiently small for the gravity to be negligible.

Consider the system just before formation of the bridge in Figure A.6, where the top surface is about to touch the sessile drop at point P_o. The CA of the sessile drop with the bottom surface is denoted as θ_{ini}. The vertical distance between the surfaces is represented by the distance of P_o from the bottom surface (H_o, in Figure A.6). The location of the drop with respect to the cusp is represented by the distance from P_o to the intersection of the surfaces (o) horizontally (L is Figure A.6). H_o and L are two determining parameters that define the height and location of the bridge. In a scaled system, H_o and L are proportional to $\sqrt[3]{V}$.

Due to small Bond number $O(10^{-2})$, the sessile drop on the bottom surface can be approximated by a truncated sphere; as such, H_o and L can be calculated in terms of θ_{ini}, ψ and V, as given in Eqns. (A.2) and (A.3), respectively.

$$\frac{H_o}{\sqrt[3]{V}} = \frac{\sqrt[3]{\frac{3}{\pi}}(cos(\psi) - cos(\theta_{ini}))}{\sqrt[3]{cos^3(\theta_{ini}) - 3\,cos(\theta_{ini}) + 2}} \tag{A.2}$$

$$\frac{L}{\sqrt[3]{V}} = \frac{H_o}{\sqrt[3]{V}}cot(\psi) = \frac{\sqrt[3]{\frac{3}{\pi}}(cos(\psi) - cos(\theta_{ini}))\,cot(\psi)}{\sqrt[3]{cos^3(\theta_{ini}) - 3\,cos(\theta_{ini}) + 2}} \tag{A.3}$$

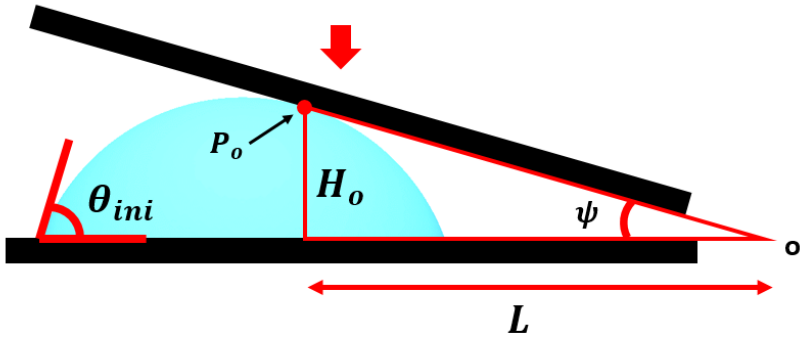

Figure A.6 The system just before bridge formation. The top surface is about to touch the sessile drop at point P_o. The CA of the sessile drop with the surface is denoted as θ_{ini}. The distance from P_o to the bottom surface is denoted as H_o, and L is the distance from P_o to the cusp (o) of the surfaces horizontally.

Equations (A.2) and (A.3) show that L and H_o are proportional to $\sqrt[3]{V}$, if two conditions are met: constant θ_{ini} and constant ψ. This is regardless of where the sessile drop is first placed on the bottom surface; when changing the initial location of the sessile drop, the position of the cusp will change accordingly, so that the bridge will always be at constant L and H_o. These two conditions are indeed met in our experimental process. First, the change in the volume was done by repeating the experiment with a new volume of sessile drop, and top surface was moved down with the same ψ to form the bridge. Also, due to the method of drop deposition on the bottom surface, θ_{ini} was always close to θ_a and did not vary with the liquid volume. Hence, the scaling of lengths with $\sqrt[3]{V}$ should be satisfied.

Both experimentally and numerically, we confirmed the scaling of all lengths of the bridge with $\sqrt[3]{V}$. For instance, consider the three lengths illustrated in Figure A.7, where D_2 is the contact line width on the bottom surface, and h_1 and h_2 are, respectively, the distances from the rightmost contact point on the top surface to the bottom surface, and the corresponding distance for the leftmost contact point. Table A.4 shows the value of D_2, h_1 and h_2 for three liquid bridges with

different volumes, all normalized by $\sqrt[3]{V}$. The data were obtained from the experiments, and the surfaces were PMMA (2) with $\psi = 3°$. It can be seen that the normalized lengths are independent of the liquid volume. We have also examined and confirmed the linear scaling of other lengths in the system with $\sqrt[3]{V}$ both experimentally and numerically (data not shown).

Working with a scaled system means that all the dimensionless quantities remain the same across systems with different volume. Therefore the critical angle ψ_c, as a dimensionless quantity in the system, will be independent of V. Physically, this means that all liquid bridge systems that obey the scaling will behave the same regardless of the volume of the bridge. The systems that are not obeying the scaling will have a behavior that will depend on the volume of the bridge e.g., see the results in Ref. 7 in comparison to the data here. The scaling was confirmed in our work by both experimental and numerical examinations for three different volumes (1, 2 and 3μL), and the data has been presented in Figure 2.7 in the main text.

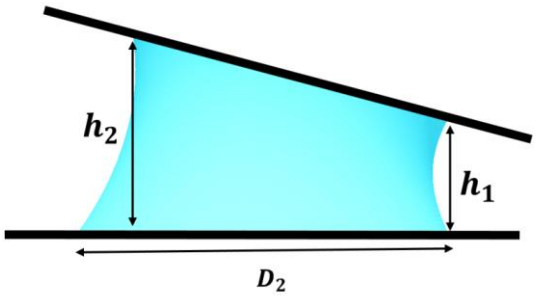

Figure A.7 Examples of lengths in the formed liquid bridge.

Table A.4 Values of D_2, h_1, and h_2 (see definitions in Figure A.7), normalized by $\sqrt[3]{V}$, for three different volumes.

Volume	$D_2/\sqrt[3]{V}$	$h_1/\sqrt[3]{V}$	$h_2/\sqrt[3]{V}$
$V = 1\mu L$	$\frac{1.50mm}{\sqrt[3]{1\mu L}} = 1.50$	$\frac{0.60mm}{\sqrt[3]{1\mu L}} = 0.60$	$\frac{0.70mm}{\sqrt[3]{1\mu L}} = 0.70$
$V = 2\mu L$	$\frac{1.91mm}{\sqrt[3]{2\mu L}} = 1.515$	$\frac{0.77mm}{\sqrt[3]{2\mu L}} = 0.611$	$\frac{0.86mm}{\sqrt[3]{2\mu L}} = 0.682$
$V = 3\mu L$	$\frac{2.19mm}{\sqrt[3]{3\mu L}} = 1.518$	$\frac{0.9mm}{\sqrt[3]{3\mu L}} = 0.624$	$\frac{1mm}{\sqrt[3]{3\mu L}} = 0.693$

A.6: An example for the effect of CAH on F_{Lmax}

In Figure A.8, the value of F^*_{Lmax} (F_{max} normalized by $\gamma\sqrt[3]{V}$) is shown for three systems with a common $\theta_a = 75°$ but different CAH from 10° to 30. When CAH is increased, F^*_{Lmax} increases as well, and as a result, the bridge can remain stable at larger dihedral angles (ψ_c is labeled on each data point).

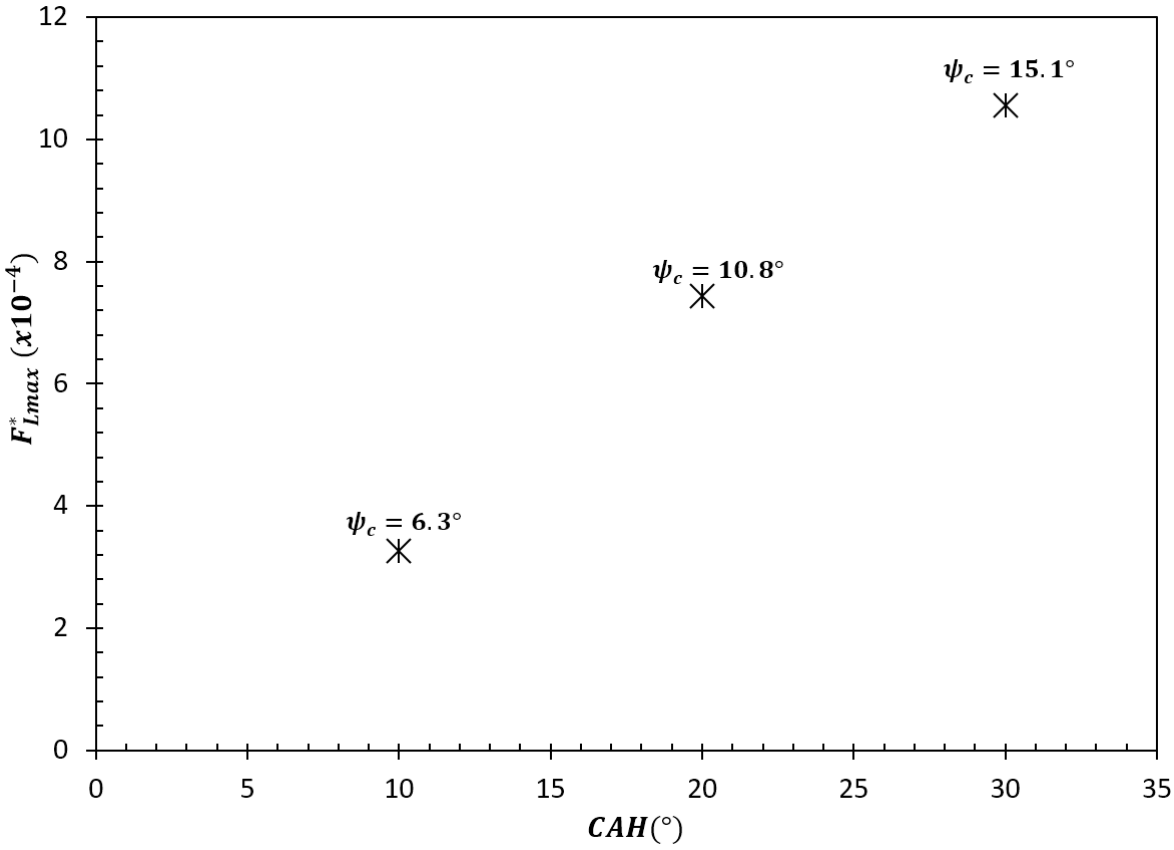

Figure A.8 F^*_{Lmax} versus CAH for three systems with $CAH = 10°, 20°$ and $30°$. All systems have the common $\theta_a = 75°$. The values of F^*_{Lmax} were calculated at a dihedral angle very close to ψ_c ($\psi_c - 0.01^{\circ}$). For each system, ψ_c is labeled on the data point.

A.7: $|F^*_P + F^*_n|$ versus ψ for three systems with common CAH but different θ_a.

In Figure A.9, $|F^*_P + F^*_n|$ versus ψ for three systems with the same *CAH* but different θ_a (from 60° to 90°) is shown. Again, the superscript * represents quantities normalized by $\gamma\sqrt[3]{V}$. It can be seen that at a given ψ, as θ_a is increased, $|F^*_P + F^*_n|$ decreases. Hence, F^*_L required to balance these forces decreases. Such decrease, means a smaller difference between the CAs on the two sides of the bridge ($\Delta\theta$) is needed to generate the needed F_L to balance. Thus, maximum of $\Delta\theta$ ($= CAH$), and F^*_{Lmax} occurs at a larger ψ, and ψ_c increases.

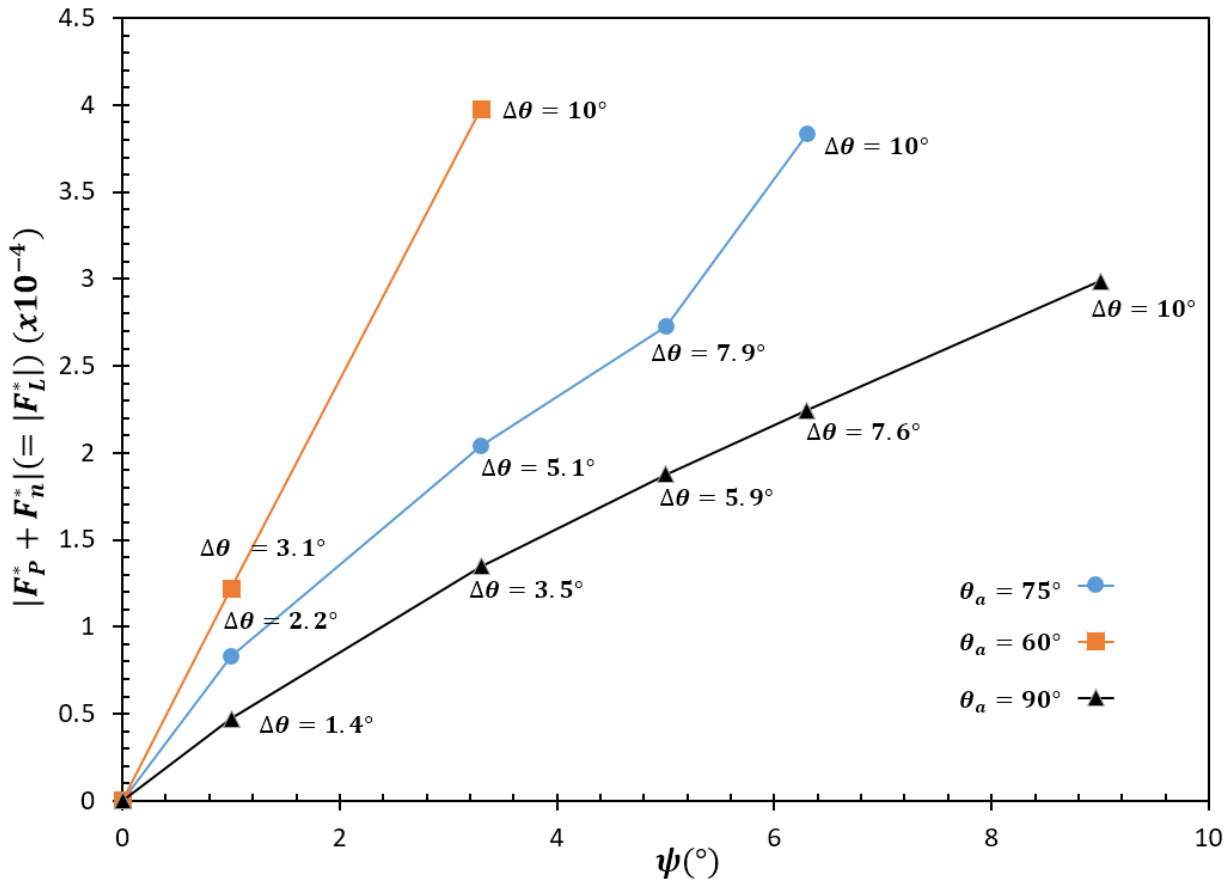

Figure A.9 The value of $|F_P^* + F_n^*|(= |F_L^*|)$ versus ψ for three systems with $\theta_a = 60°, 75°\ and\ 90°$. The CAH for all the systems is 10°. At $\psi = 0°$, F_L is zero as there is no lateral force when surfaces are parallel. The value of $\Delta\theta$ was averaged on top and bottom surfaces. Lines are to guide the eye.

A.8: Validating the effect of θ_a and CAH on ψ_c using Equation (2.7)

We start with proving that increasing θ_a increases ψ_c. For this purpose, we show that assuming an increase in θ_a reduces or does not change ψ_c will lead to contradiction in the geometry of the system. Consider two surfaces A and B with the same CAH, but surface A's advancing CA is larger than that of surface B ($\theta_{a,A} > \theta_{a,B}$). First assume the critical angles in both cases are equal ($\psi_{c,A} = \psi_{c,B}$). Since the initial sessile drop CA is equal to θ_a, as $\theta_{a,A} > \theta_{a,B}$, for a constant volume, the

sessile droplet on surface B has a lower H_{ini} compared to the droplet on surface A (see Figure A.10). Due to the difference in H_{ini}, the distance between the rightmost contact points of the bridge with the top and bottom surfaces (h_o in Figure A.10) is smaller for the surface with smaller θ_a (i.e. surface B). Because $l_o = (h_o \csc\psi/2)/2$, at an equal $\psi_{c,A} = \psi_{c,B}$, the bridge between surfaces of type B forms closer to the cusp, leading to $l_{o,A} > l_{o,B}$. In addition, because of the constant volume constraint, the bridge with smaller h_o acquires larger l_b i.e., $l_{b,B} > l_{b,A}$. Subsequently, using the LHS of Eqn. (2.7), one can write:

$$\frac{l_{o,B}}{(l_{o,B} + l_{b,B})} < \frac{l_{o,A}}{(l_{o,A} + l_{b,A})} \tag{A.4}$$

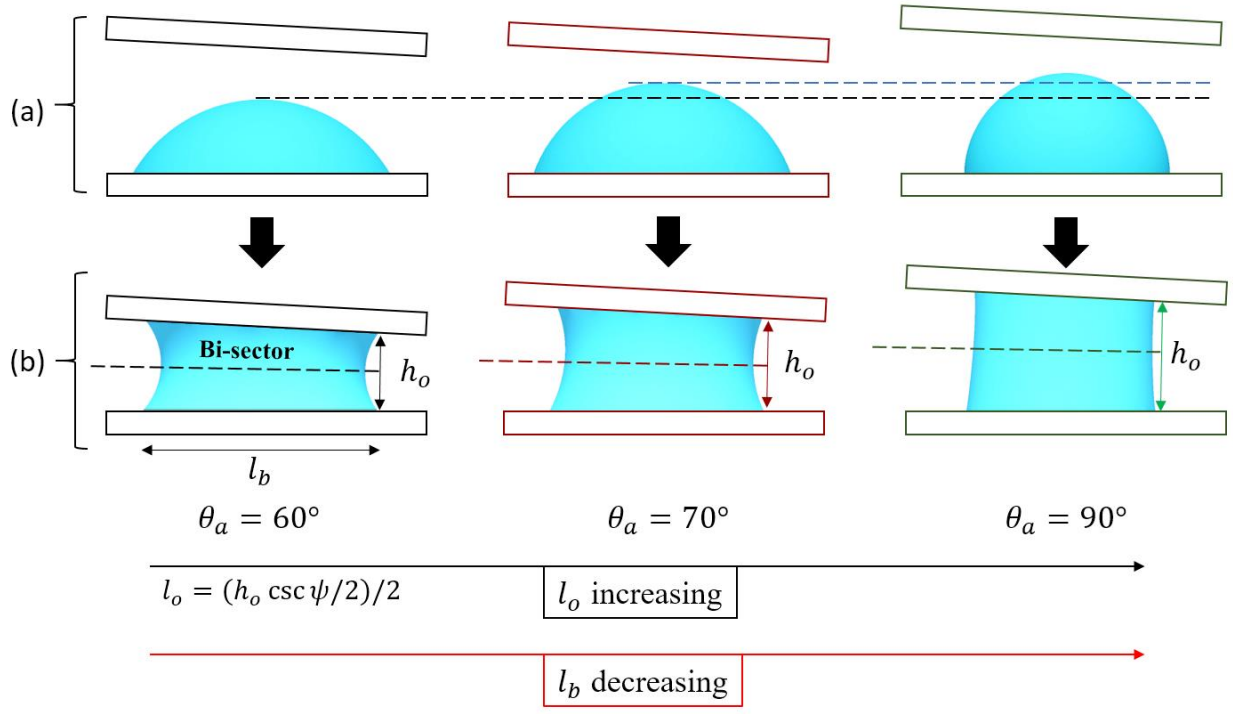

Figure A.10 a) The increase in H_{ini} with respect to θ_a is shown for three systems with $\theta_a = 60°$, 70°, and 90°. The volume is the same for all of the systems. b) The distance between the rightmost contact points of the bridge on top and bottom surfaces is denoted as h_o. For a constant ψ, as θ_a is increasing, h_o is also increased, leading to increase in l_o, and decrease in l_b.

However, it can be easily shown that if the RHS of Eqn. (2.7) for surfaces A and B was compared, it would contradict Inequality (A.4). To show this, consider the RHS of Eqn. (2.7) at the critical angle, where $\theta_1 = \theta_a$ and $\theta_2 = \theta_r = \theta_a - CAH$. At this point, RHS of Eqn. (2.7) can be written as:

$$\frac{\cos(x)}{cos(x - C)} = f(C, x) \tag{A.5}$$

where $C = CAH - \psi_c$ and $x = \theta_a - \frac{\psi_c}{2}$. It is easy to show that both $\frac{\partial f}{\partial C}$ and $\frac{\partial f}{\partial x}$ are negative in the range of $\theta_a < (\frac{\pi}{2} - \frac{\psi}{2})$. Considering the assumption that $\psi_{c,A} = \psi_{c,B}$ and $\theta_{a,A} > \theta_{a,B}$, in Eqn. (A.5) $C_B = C_A$ and $x_A > x_B$. Because both $\frac{\partial f}{\partial C}$ and $\frac{\partial f}{\partial x}$ are negative, $f(C_B, x_B) > f(C_A, x_A)$, which is in contradiction with Inequality (A.4). So the assumption that $\psi_{c,A} = \psi_{c,B}$ cannot be true. Similarly, if $\psi_{c,A} < \psi_{c,B}$ was assumed, Inequality (A.4) still holds. At the same time $C_B < C_A$ and $x_B < x_A$, which leads to $f(C_B, x_B) > f(C_A, x_A)$, again contradicting (A.4). Assuming $\psi_{c,A} > \psi_{c,B}$ would lead to no contradiction, which proves that increasing θ_a increases ψ_c.

Following the same line of reasoning, we now consider two surfaces A and B with the same θ_a, but surface A's CAH is larger than that of surface B ($CAH_A > CAH_B$). First assume the critical angles in case A is smaller than case B ($\psi_{c,A} < \psi_{c,B}$). Since the initial sessile drop CA is equal to θ_a, as $\theta_{a,A} = \theta_{a,B}$ the top surface touches the sessile droplet on both surfaces at the same H_{ini}. So, if $\psi_{c,A} < \psi_{c,B}$, then $l_{o,A} > l_{o,B}$, i.e., the bridge between surfaces B forms closer to the cusp. We assume that deviations in l_b is negligible as CAH is changing (which is reasonable based on experimental and simulation data, data not shown), thus $l_{b,B} \approx l_{b,A}$, which leads to inequality

(A.4). Using the assumption that $\psi_{c,A} < \psi_{c,B}$ and $CAH_A > CAH_B$, in inequality (A.5) $C_A > C_B$ and $x_A > x_B$. Since both $\frac{\partial f}{\partial C}$ and $\frac{\partial f}{\partial x}$ are negative, one has $f(C_B, x_B) > f(C_A, x_A)$, which contradicts Inequality (A.4). Thus, the assumption that $\psi_{c,A} < \psi_{c,B}$ cannot be valid. Similarly, if $\psi_{c,A} = \psi_{c,B}$ was assumed, $l_{o,B} = l_{o,A}$ and $l_{b,B} = l_{b,A}$ leading to $f(C_B, x_B) = f(C_A, x_A)$. On the other hand, $C_A > C_B$ and $x_A = x_B$, which leads to $f(C_B, x_B) > f(C_A, x_A)$, again in contradiction with $f(C_B, x_B) = f(C_A, x_A)$. Only assuming $\psi_{c,A} > \psi_{c,B}$ does not lead to any contradiction, which verifies that the increase in CAH increases ψ_c.

A.9: Effect of θ_{ini} on ψ_c

As shown in Eqns. (A.2) and Eqn. (A.3), the value of θ_{ini} affects the distance of the bridge from the cusp of the surfaces (L), and the vertical distance between the surfaces (H_o). When θ_{ini} decreases, both H_o and L decrease, which makes the bridge more confined between the surfaces. Such confinement affects the principal radii of the curvature of the bridge (R and R_t), and also the length of the contact lines. This means that θ_{ini} can change the balance between the adhesion and pressure forces in the global force balance (i.e. Eqn. (2.3) in the main text), and therefore, it can affect the value of ψ_c.

We will use Eqn. (2.3) to discuss the effect of θ_{ini} on ψ_c. For this goal, the three terms on the LHS of Eqn. (2.3) (all normalized by $\gamma\sqrt[3]{V}$) were calculated numerically using Surface Evolver for three systems, where θ_a, CAH and ψ were fixed at 75°, 30° and 5°, respectively; and θ_{ini} was assigned three values: θ_a, $(\theta_a + \theta_r)/2$, and θ_r. The values of the force components are shown in Figure A.11, along with inset images (that are to scale) of the stable liquid bridges at different θ_{ini}.

As shown in Figure A.11, as θ_{ini} decreases, F_P^* starts to decrease from a positive value, passes through zero and eventually becomes negative. At the same time, $|F_n^*|$ also increases as θ_{ini} decreases, so that $|F_P^* + F_n^*|$ increases. This implies that the needed F_L^* $(= -F_P^* - F_n^*)$ to balance the global force is larger when θ_{ini} is smaller. The larger F_L^* is accommodated by a larger difference between the CAs on the two sides of the bridge (see $\Delta\theta$ in Figure A.11). Therefore, for a system with smaller θ_{ini}, the maximum $\Delta\theta$ $(= CAH)$, generating F_{Lmax}^*, occurs at a smaller ψ compared to a system with larger θ_{ini}, which ultimately decreases the value of the ψ_c. This was confirmed by calculating ψ_c for the systems using Surface Evolver; respectively, the values of ψ_c are 15°, 11.7°, and 9.7°, when θ_{ini} are equal to θ_a, $(\theta_a + \theta_r)/2$, and θ_r.

The effect of θ_{ini} on F_P^* can be explained by looking at how the mean curvature, M, changes with θ_{ini}. When θ_{ini} decreases, due to larger confinement of the bridge between the surfaces (see the inset images), $|R|$ becomes smaller, and R_t becomes larger. Because R is negative while R_t is positive, $M = \left(\frac{1}{R} + \frac{1}{R_t}\right)^{-1}$ changes from positive to negative and continues to decrease afterwards, which in return decreases F_P^* (see Eqn. (2.3) in the main text). On the other hand, the bridge with larger confinement between the surfaces (at a smaller θ_{ini}), will experience an increase in the length of the contact lines. Since F_n^* is integrated over the length of the contact lines, its magnitude increases as θ_{ini} decreases.

In driving the empirical function given in Eqn. (2.10), systems are assumed to have $\theta_{ini} \approx \theta_a$; therefore, Eqn. (2.10) is only applicable when $\theta_{ini} \approx \theta_a$. For $\theta_{ini} < \theta_a$, Eqn. (2.10) provides an upper bound for ψ_c. The same method of derivation for Eqn. (2.10) can be used to find the empirical function suitable for systems with different θ_{ini}.

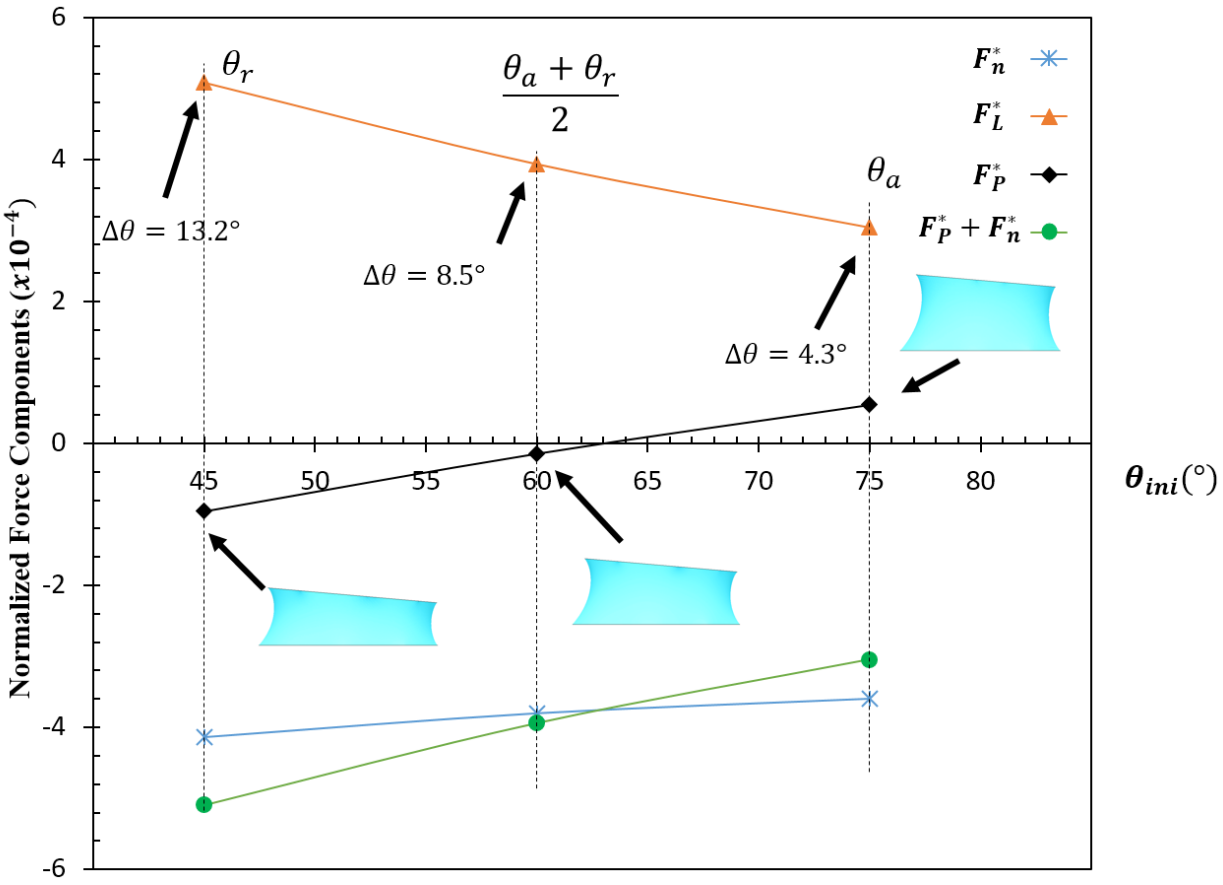

Figure A.11 The normalized force components in Eqn. (2.3) for different θ_{ini} while θ_a, CAH and ψ were fixed at 75°, 30° and 5°, respectively. $\psi = 5°$ is less than the critical angle in all cases, so all bridges are stable. Simulated shapes of the bridge are included to illustrate the change in curvatures. Inset images of the bridges are to scale (having the same volume). The value of $\Delta\theta$ was averaged on top and bottom surfaces. Lines are to guide the eyes.

B: Supporting Information for Chapter Three

B.1: Equivalency of tweezer-like systems to systems with fixed ψ

Figures B.1a and B.1b show schematics of the systems studied in Refs. 7, 8, and 16 (System A), and the system in this study (System B), respectively. In System A, l_o and l_b are, respectively, the distance of the rightmost contact point on the bottom surface from the cusp of the surfaces, and the width of the contact line on the bottom surface. ψ is initially at $\psi = \psi_{ini}$, then the top surface is rotated around surfaces' cusp (for $\Delta\psi$) to compress or stretch the bridge.

System A can be considered to be equivalent to System B, if three conditions are met: First, the amount of compressing and stretching of the bridge should be approximately uniform across the liquid interface i.e., if $(l_o + l_b)\Delta\psi \approx l_o\Delta\psi$. Second, the directions of compressing and stretching should be nearly normal to the bottom surface. And third, $\Delta\psi$ should be sufficiently small for the change in ψ to be negligible. If these three conditions are met, System A can be considered to be equivalent to System B with $\psi \equiv \psi_{ini}$ and $\Delta h^* \equiv l_o^*\Delta\psi$.

The first condition can be met, if $l_o \gg l_b$. The second condition can be satisfied, if ψ_{ini} is small (on the order of a few degrees), at which it is reasonable to assume that the directions of compressing and stretching are approximately normal to the bottom surface. And the third condition can be satisfied, if $\Delta\psi$ is sufficiently small such that $|(\Delta X_n^*)_{\psi=\psi_{ini}} - (\Delta X_n^*)_{\psi=\psi_{ini}-\Delta\psi}| < \epsilon$, where $(\Delta X_n^*)_{\psi=\psi_{ini}}$ and $(\Delta X_n^*)_{\psi=\psi_{ini}-\Delta\psi}$ are, respectively, ΔX_n^* of systems with ψ <u>fixed</u> at $\psi = \psi_{ini}$ and $\psi = \psi_{ini} - \Delta\psi$, and ϵ is an acceptable tolerance.

In all results given in Figures 3.4-3.10 (for ΔX_1^*) of the main text:

- $l_o/l_b > 10$, hence, the first condition can be satisfied.
- $\psi \leq 4°$, satisfying the second condition.

- $\Delta\psi$ satisfies the third condition with $\epsilon \leq 0.05$ for systems with $\theta_a = 60°$, and with $\epsilon \leq 0.02$ for all other systems. In both cases ϵ is reasonably small.

Consequently, the conclusions given in the main text can be applicable for systems similar to System A.

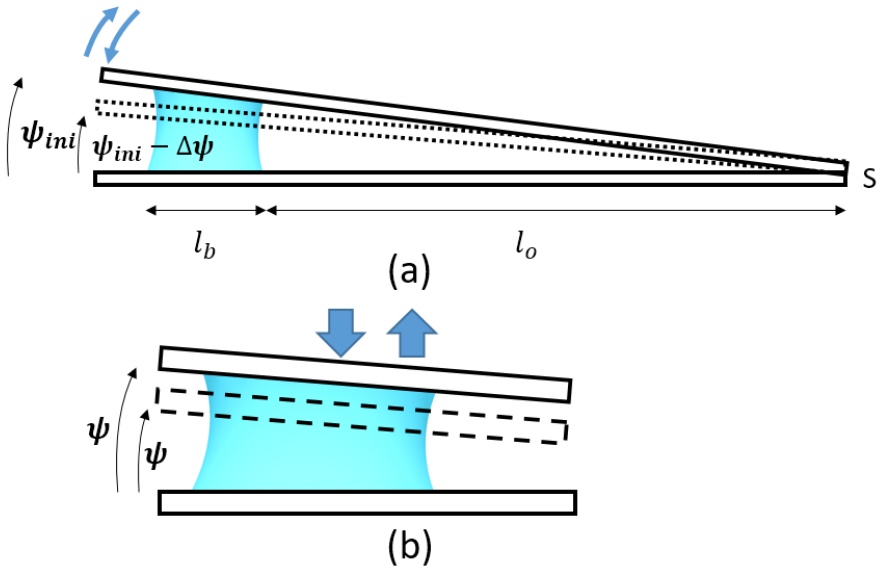

Figure B.1 a) Schematic of the system studied in refs. 7, 8 and 16. The compressing and stretching of the bridge was provided by varying ψ around S. b) The compressing and stretching of the bridge studied here was provided by direct vertical motion of the top surface, while ψ remained fixed.

B.2: Table of parameters used in simulations

In Table B.1, the parameters used in Surface Evolver simulations are given. All possible combination of parameters in each row were simulated. In total, 155 simulations were performed.

Table B.1 Values of parameters used in Surface Evolver simulations. All possible combination of parameters in each row were simulated.

$\theta_a(°)$	$CAH(°)$	$\psi(°)$	Δh^*
60-80-90	10, 20, 30	1,2, 3, 4	0.08, 0.16, 0.23, 0.31
80.1	19.6	2, 3	0.16, 0.31
80.1	19.6	4	0.16
81.2	12.1	2, 3	0.16, 0.31
81.2	12.1	4	0.16
60	20	0.5	0.16

B.3: Comparison between depinning of contact lines on top and bottom surfaces

In Figure B.2, the values of θ_{1b} and θ_{1t} for the system in Figure 3.4 are shown during compressing stage. It can be seen that, before the start of compression, θ_{1b} is smaller than θ_{1t}, and during the compression θ_{1t} reaches θ_a earlier than θ_{1b}. As a result, the contact line depins earlier on the top surface compared to the bottom surface.

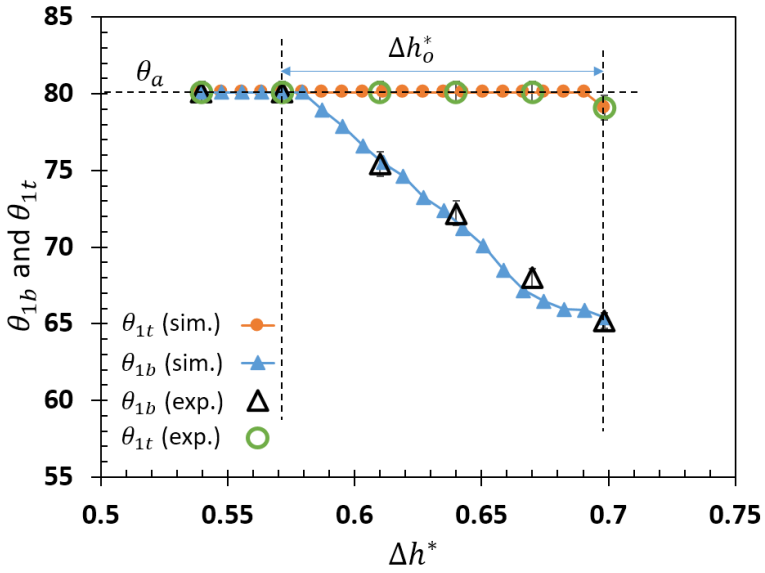

Figure B.2 Values of θ_{1b} and θ_{1t} during compression for the system in Figure 3.4. Lines are to guide the eyes.

B.4: Understanding the effect of CAH on the pinning period at the beginning of stretching stage

Figure B.3 shows the distribution of CAs at the beginning of stretching stage for the systems in Figure 3.6a (of the main text). It can be seen that. with larger CAH, the CAs lie farther from the receding angle, which increases the difficulty of depinning in the stretching stage and hence the pinning period increases.

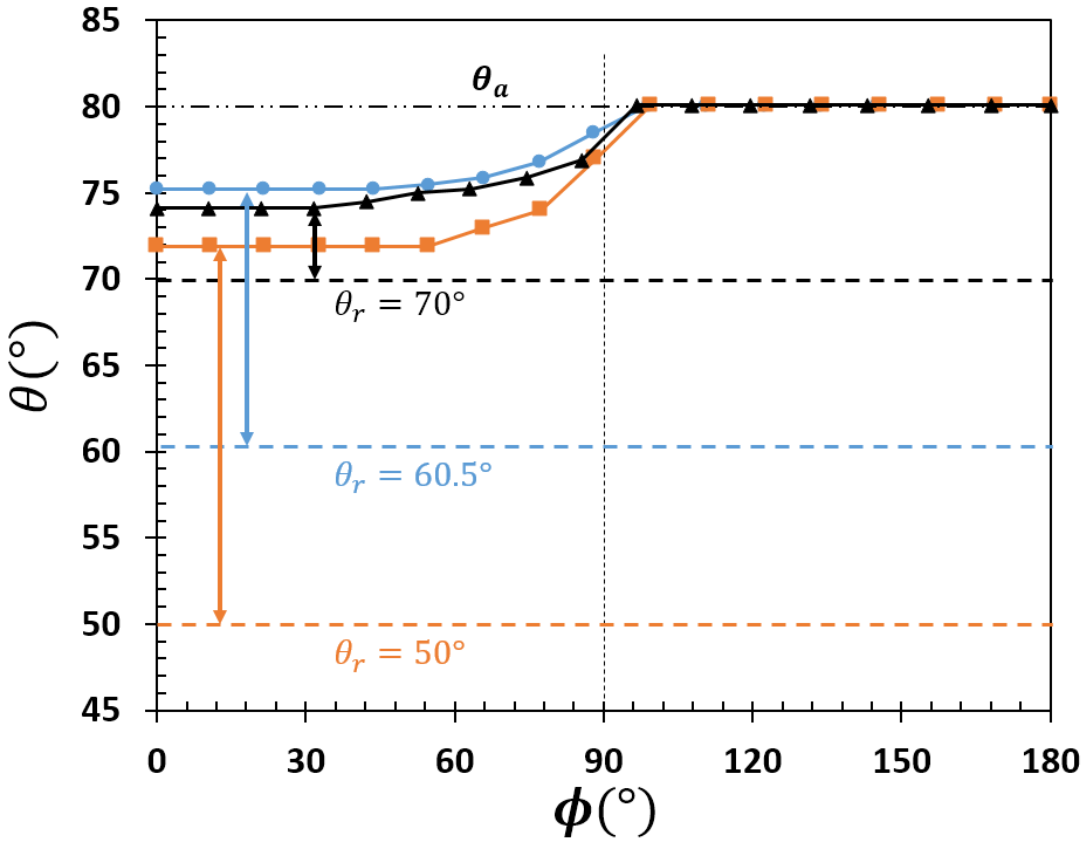

Figure B.3 The value of CAs along the contact line (versus ϕ) for the system in in Figure 3.6, prior to the beginning of stretching stage. Lines are to guide the eyes.

B.5: Understanding the effect of ψ on the pinning period at the beginning of stretching stage

Figure B.4 shows the distribution of CAs at the beginning of stretching stage for systems in Figure 3.8a (of the main text). It can be observed that increasing ψ reduces the gap between θ_r and the CAs on the wide side of the bridge. The smaller gap reduces the pinning period at the beginning of stretching stage.

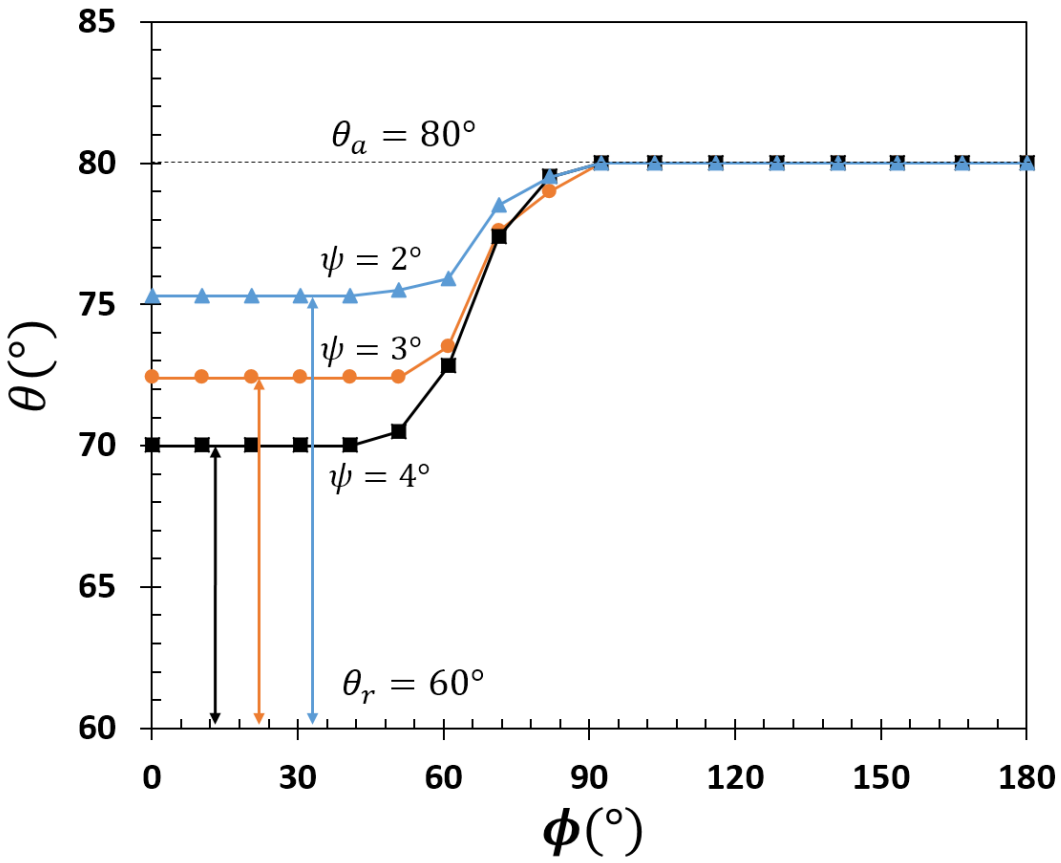

Figure B.4 The value of CAs along the contact line (versus ϕ) for the systems in Figure 3.8, prior to the beginning of stretching stage. Lines are to guide the eyes.

B.6: Section S6: Interdependent effects of parameters on ΔX_1^*

The interdependence relationship among ΔX_1^*, θ_a, CAH, and ψ can be observed from Figures B.5a and B.5b. In Figure B.5a, ΔX_1^* is plotted against θ_a for different values of ψ, where all the systems have $CAH = 20°$ and $\Delta h^* = 0.16$. It can be observed that the influence of ψ on ΔX_1^* is larger (larger separation between the three curves) when θ_a is smaller. As discussed earlier, increase in ψ mainly affected ΔX_1^* through the reduction in Δh_o^*. The systems with smaller θ_a have smaller ψ_c (see Eqn. (3.2)), hence, based on Eqn. (3.1), a constant increase in ψ, would cause a larger relative reduction in Δh_o^* when θ_a is smaller. Therefore, ΔX_1^* is more influenced by ψ when θ_a is smaller. A similar interdependent influence from ψ and CAH on ΔX_1^* can be observed from Figure B.5b, where the systems have the same $\theta_a = 80°$ but different CAH. Likewise, the effect of ψ on ΔX_1^* is larger at smaller values of CAH. This can also be explained by recognizing that systems with smaller CAH have smaller ψ_c (see Eqn. (3.2)). Though, there is a larger separation of the three curves in Figure B.5a compared to Figure B.5b (to aid the comparison, Figures have similar scales). Because ψ_c is more sensitive to the changes in θ_a than CAH (see Eqn. (3.2)), in Figure B.5a, the influence of ψ on ΔX_1^* is reduced more significantly when θ_a is increased, compared to Figure B.5b where CAH is increased. Such complex interdependent effect of the parameters on the horizontal movement of the bridge was unknown prior to this study.

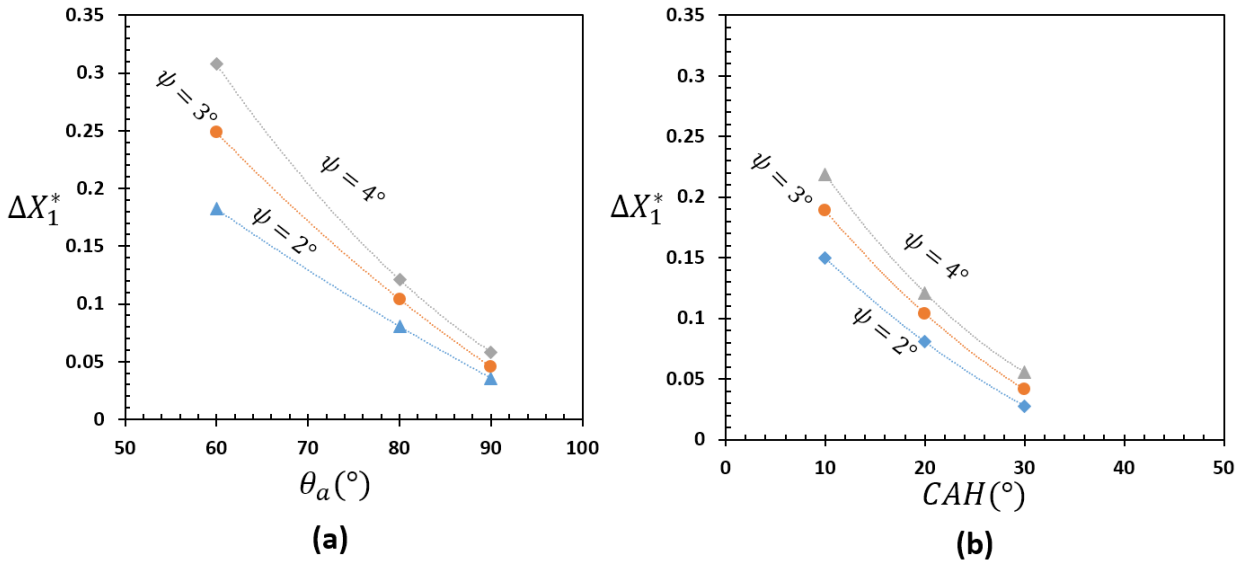

Figure B.5 a) ΔX_1^* versus θ_a for different values of ψ. All systems have common $CAH = 20°$ and $\Delta h^* = 0.16$. b) ΔX_1^* versus CAH for different values of ψ. All systems have common $\theta_a = 80°$ and $\Delta h^* = 0.16$. Lines are to guide the eyes.

As it can be seen, the parameters ψ, θ_a, and CAH influence ΔX_1^* in a complex manner. Therefore, it is difficult to find a simple equation in closed-form to predict ΔX_1^*. Multiple regression analysis was conduct based on our simulation data, until it was found that an equation in the form of Eqn. (B.1) fits very well to our data (data falls within error bars of the experimental data).

$$\Delta X_1^* = 0.0048 CAH^{2.97} \left[\frac{\Delta h^{*0.37}}{(\psi_c - \psi)^{0.17}} \right]^{CAH^{0.58}} \tag{B.1}$$

In Eqn. (B.1), all the angles are in degrees. A comparison between ΔX_1^* from the simulations and experimental data, and ones calculated from Eqn. (B.1) is given in Figure B.6. It can be seen that Equation (3.1) is capable of predicting ΔX_1^* with a good agreement. Similar to the fitting of Eqn.

(B.1), the experimental data was not included in the fitting, hence, they could be used independently to test the viability of Eqn. (B.1).

From Eqn. (B.1), it is clear that ΔX_1^* is significantly influenced by CAH, as it appears twice in Eqn. (B.1), once explicitly, and once implicitly through ψ_c. One can also interpret the term inside the brackets as the representative of the ratio between Δh^* and Δh_o^*. Such complicated form of Eqn. (B.1) shows the complex interdependency of the parameters.

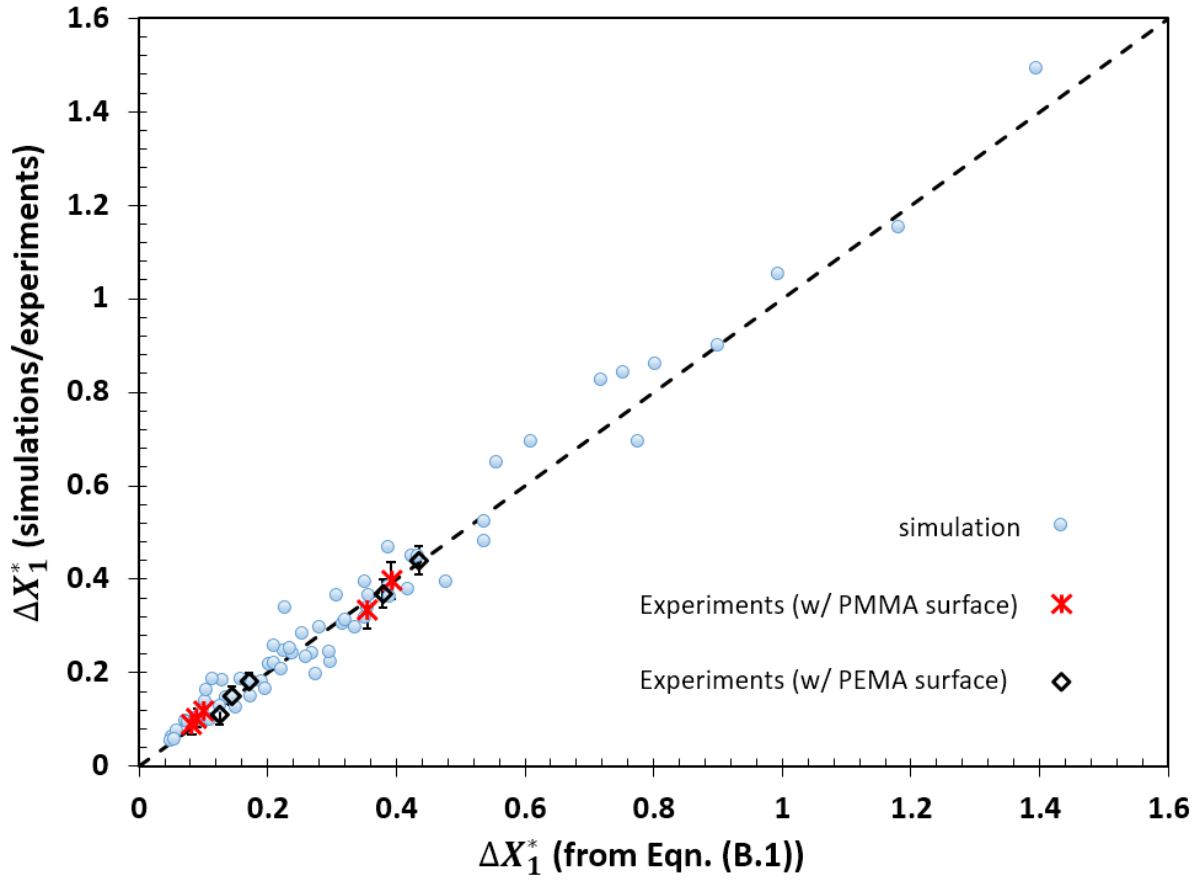

Figure B.6 Comparison between ΔX_1^* calculated from Eqn. (B.1) (horizontal axis) and the corresponding experimental and simulation data (vertical axis). The black dash-line is the 45° line.

C: Surface Evolver Code used in Chapter Two and Chapter Three

C.1: Surface Evolver code used in Chapter Two

To understand how the simulations were done, one needs to be familiar with the fundamentals of Surface Evolver (SE) coding language first i.e. refer to Refs. 22 and 23. Also, Ref. 27 should be studied to comprehend the implementation of CAH in SE.

We also thank Dr. White (corresponding author of Ref. 27) for his guidelines in implementing CAH in SE.

An example of the code used in Chapter Two is replicated below alongside with comments. In this example, surfaces have $\theta_a = 60°$ and $CAH = 30°$.

```
1  parameter s_angle = 2 // slope in y direction of top surface
2  PARAMETER height = 0.75e-3 /* separation of the surfaces
   measured from x=y=0 */
3  PARAMETER adv_up = 60      /* Advancing angle of the top
   surface in degrees */
4  PARAMETER rec_up = 30 /* Receding angle of the top surface in
   degrees */
5  PARAMETER adv_b = 60 /*Advancing angle of the bottom surface
   in degrees */
6  PARAMETER rec_b = 30 /* Receding angle of the bottom surface
   in degrees*/
7  parameter top_angle_ini = 60 /* initial angle between the
   liquid and the top surface, degrees*/
```

```
8  parameter bottom_angle_ini = 30 /* initial angle between the
   liquid and the bottom surface, degrees*/
9  PARAMETER y_angle_up = 45 //young CA of the top surface
10 PARAMETER y_angle_b =45 //young CA of the bottom surface
11 PARAMETER volu=2e-9 //liquid volume
12 #define usize ((volu)^(1/3)) /* usize and usize are two
   different length dimensions to provide larger initial contact
   area on the top surface than the bottom surface i.e.
   usize>ysize. Using other lengths does not matter as long as
   usize>ysize */
13 #define ysize (volu^(1/3)/3)
14 #define slope tan(s_angle*pi/180) //defining slope base on
   s_angle
15 gravity_constant 0 // zero gravity
16 // Contact surface tensions
17 #define UPPERT (-cos(top_angle_ini*pi/180)) /* virtual tension
   of facet on the top surface*/
18 #define LOWERT (-cos(bottom_angle_ini*pi/180)) /* virtual
   tension of facet on the bottom surface*/
19 constraint 1   /* the bottom surface */
20 formula: z = 0
21 energy:  // energy of the content (for contact angle)
22 e1: -(LOWERT*y)
23 e2: 0
```

```
24 e3: 0
25 constraint 2   /* the top surface */
26 formula: z = height + slope*y   //slope term
27 energy:  // for contact angle
28 e1: -(UPPERT*y)*sqrt(1+slope^2)  // hypotenuse length
29 e2: 0
30 e3: 0
31 content:
32 c1: 0
33 c2: -z*x // using y term so strips are at constant height
34 c3: 0
   //Various element attributes are defined below.
   //CA storage
35 define vertex attribute angle real
36 define vertex attribute yadh_b real
37 define vertex attribute yadh_up real
38 define vertex attribute zadh_b real
39 define vertex attribute zadh_up real
40 define vertex attribute yp_b real
41 define vertex attribute yp_up real
   //position storage
42 define  vertex attribute oldx real[3]
43 define  vertex attribute oldx2 real[3]
   // some attribute for tweaks
```

```
44 define vertex attribute vcl_up integer
45 define edge attribute ecl_up integer
46 define facet attribute fcl_up integer
47 define vertex attribute vcl_b integer
48 define edge attribute ecl_b integer
49 define facet attribute fcl_b integer
50 define vertex attribute vcl integer
51 define edge attribute ecl integer
   /*Elements are defined below such that the initial contact
   area on the top surface is larger than the bottom surface (by
   using usize and ysize */
52 vertices
53 1  0.0  0.0  0.0   constraint 1
54 2  usize 0.0  0.0   constraint 1
55 2  usize usize 0.0   constraint 1
56 3  0.0  usize 0.0   constraint 1
57 5  ysize 0 height constraint 2  /* top surface */
58 6  2*ysize 0 height constraint 2
59 7  2*ysize ysize height+ysize*slope    constraint 2
60 8  ysize  ysize height+ysize*slope   constraint 2
61 edges  /* connecting edges */
62 1    1 2    constraint 1 /* 4 edges on bottom surfaces */
63 2    2 3    constraint 1
64 3    3 4    constraint 1
```

```
4    4 1    constraint 1
5    5 6    constraint 2 /* top surface */
6    6 7    constraint 2
7    7 8    constraint 2
8    8 5    constraint 2
9    1 5
10   2 6
11   3 7
12   4 8
faces  /* given by oriented edge loop */
1  10 -5  -9 color lightblue
2  11 -6 -10 color lightblue
3  12 -7 -11 color lightblue
4   9 -8 -12 color lightblue
bodies  /* one body, defined by its oriented faces */
1   1 2 3 4    volume volu /*attributing the volume to the
  body*/
Read
  /*"initcl" identifies the triple lines for SE, and turn their
  colors to red. */
initcl:=
{
printf "no error yet"; //for debugging purposes
set vertex.vcl_up 0;
```

```
86 set edge.ecl_up 0;
87 set vertex.vcl 0;
88 set edge.ecl 0;
89 set facet.fcl_up 1;
90 set vertex.vcl_b 0;
91 set edge.ecl_b 0;
92 set facet.fcl_b 1;
93 foreach vertex vv do if on_constraint 1 then
94 {
95 set vv.vcl_b 1;
96 set vv.vcl 1;
97 };
98 foreach vertex vv do if on_constraint 2 then
99 {
100  set vv.vcl_up 1;
101  set vv.vcl 1;
102  };
103  foreach edge ee do if on_constraint 1 then
104  {
105  set ee.ecl_b 1;
106  set ee.ecl 1;
107  };
108  foreach edge ee do if on_constraint 2 then
109  {
```

```
110  set ee.ecl_up 1;
111  set ee.ecl 1;
112  };
113  set edges color red where ecl_up == 1;
114  set edges color red where ecl_b == 1;
115  //set facets color blue where fclup == 0;
116  //set facets color blue where fclb == 0;
117  }
   /* plotup function identifies contact angles and contact
   widths visible from two perpendicular views (similar to the
   views from the two cameras in the experiments) and export them
   in excel files */
118  plotup := {
119  radiusmaxup1:=0;
120  radiusmaxup2:=0;
121  radiusmaxb1:=0;
122  radiusmaxb2:=0;
123  counter1:=0;
124  counter2:=0;
125  id1:=0;
126  id2:=0;
127  id3:=0;
128  id4:=0;
129  id5:=0;
```

```
130  id6:=0;
131  id7:=0;
132  id8:=0;
133  maxx2:=-10000;
134  maxyy2:=-10000;
135  minxx2:=100000;
136  minyy2:=10000;
137  maxx1:=-10000;
138  maxyy1:=-10000;
139  minxx1:=100000;
140  minyy1:=10000;
141  zo1:=0;
142  zo2:=0;
143  zo3:=0;
144  zo4:=0;
145  zo5:=0;
146  zo6:=0;
147  zo7:=0;
148  zo8:=0;
149  foreach vertex vv do if on_constraint 2 then
150  {
151  if (vv.y<minyy2) then {
152  minyy2:=vv.y;
153  id1:=vv.id;
```

```
154  zo1:=vv.z;}
155  };
156  foreach vertex vv do if on_constraint 2 then
157  {
158  if (vv.y>maxyy2) then {
159  maxyy2:=vv.y;
160  id3:=vv.id;
161  zo3:=vv.z;}
162  } ;
163  foreach vertex vv do if on_constraint 2 then
164  {
165  if (vv.x<minxx2) then {
166  minxx2:=vv.x;
167  id2:=vv.id;
168  zo2:=vv.z;}
169  } ;
170  foreach vertex vv do if on_constraint 2 then
171  {
172  if (vv.x>maxx2) then {
173  maxx2:=vv.x;
174  id4:=vv.id;
175  zo4:=vv.z;}
176  } ;
177  foreach vertex vv do if on_constraint 1 then
```

```
178  {
179  if (vv.y<minyy1) then {
180  minyy1:=vv.y;
181  id5:=vv.id;
182  zo5:=vv.z;}
183  };
184  foreach vertex vv do if on_constraint 1 then
185  {
186  if (vv.y>maxyy1) then {
187  maxyy1:=vv.y;
188  id7:=vv.id;
189  zo7:=vv.z;}
190  } ;
191  foreach vertex vv do if on_constraint 1 then
192  {
193  if (vv.x<minxx1) then {
194  minxx1:=vv.x;
195  id6:=vv.id;
196  zo6:=vv.z;}
197  } ;
198  foreach vertex vv do if on_constraint 1 then
199  {
200  if (vv.x>maxx1) then {
201  maxx1:=vv.x;
```

```
202  id8:=vv.id;
203  zo8:=vv.z;}
204  } ;
205  printf "%f  %f  %f  %f  %f  %f  %f  %f  %f  %f  %f  %f
  %f\n",height,zo1,zo3,minyy2-maxyy2,minyy1-
  maxyy1,minyy2,maxyy2,minyy1,maxyy1,vertex[id1].angle,vertex[id
  3].angle,vertex[id5].angle,vertex[id7].angle>>"frontcam.xls";
206  printf "%f  %f  %f  %f  %f\n",height,maxx2-
  minxx2,(vertex[id2].angle+vertex[id4].angle)/2,maxx1-
  minxx1,(vertex[id6].angle+vertex[id8].angle)/2>>"sidecam.xls";
207  }
  /* “plotcl” function provides the contact lines shapes and
  their distribution of contact angles. Then it will save the
  data in excel files. */
208  plotcl:=
209  {
210  foreach vertex vv do if on_constraint 1 then {
211  printf "%f  %f  %f\n",vv.x,vv.y,vv.angle>>"xb.xls"; /*for
  bottom surface */
212  };
213  foreach vertex vv do if on_constraint 2 then {
214  printf "%f  %f  %f\n",vv.x,vv.y,vv.angle>>"xup.xls"; /*for
  top surface */
215  };
```

```
216  }
   /* “cah” function implements CAH in Evolver. “cah” function
   will be used instead of the default “g” function of SE to
   evolve the surface */
217  cah:=
218  {
219  //store old positions of contact points (vertices)
220  set vertex oldx[1] x;
221  set vertex oldx[2] y;
222  set vertex oldx[3] z;
   /* calculating max and min advancing and receding friction
   forces */

223  f_max_adv_up:=(cos(y_angle_up*pi/180)-cos(adv_up*pi/180));
224  f_max_rec_up:=-(cos(y_angle_up*pi/180)-cos(rec_up*pi/180));
225  delta_f_up:=-(cos(adv_up*pi/180)-cos(rec_up*pi/180));
226  f_max_adv_b:=(cos(y_angle_b*pi/180)-cos(adv_b*pi/180));
227  f_max_rec_b:=-(cos(y_angle_b*pi/180)-cos(rec_b*pi/180));
228  delta_f_b:=-(cos(adv_b*pi/180)-cos(rec_b*pi/180));
229  g; //virtual move
230  if scale>0 then {
231  foreach vertex vv do if on_constraint 2 then
232  {
```

```
   /*only consider vertices on the contact line (constraint 1,
   top surface) */
   // Test if the vertex is in an advancing or receding situation
233  product_up:=((vv.__velocity[1])*vv.vertexnormal[1]+(vv.__ve
   locity[2])*vv.vertexnormal[2]+(vv.__velocity[3])*vv.vertexnorm
   al[3]);
234  if (product_up<0) then {
235  f_up:=f_max_rec_up; //we are in a receding situation
236  final_angle_up:=rec_up;
237  product_up:=sqrt((vv.__velocity[1])^2+(vv.__velocity[2])^2+
   (vv.__velocity[3])^2);
238  } else {
239  f_up:=f_max_adv_up; //we are in an advancing situation
240  final_angle_up:=adv_up;
241  product_up:=sqrt((vv.__velocity[1])^2+(vv.__velocity[2])^2+
   (vv.__velocity[3])^2);
242  };
243  displacement_up:=abs(product_up);  //vertex virtual
   displacement
244  length0_up:=0;
245  foreach vv.edge ee do if on_constraint 2 then {
246  length0_up:=length0_up+ee.length;   // dl (i.e.
   differential contact line length)
247  };
```

```
248  force_per_length_up:=2*displacement_up/length0_up;
   /*measure force per unit length from vertex virtual
   displacement*/
249  if (force_per_length_up<f_up) then { /*maximum friction
   force is larger than measured force: the vertex remains
   fixed*/
250  vv.x:=vv.oldx[1];
251  vv.y:=vv.oldx[2];
252  vv.z:=vv.oldx[3];
253  angle_of_up:=acos(-
   2*product_up/length0_up+cos(y_angle_up*pi/180))*180/pi; /*new
   contact angle value is assigned to the vertex*/
254  } else {   /*maximum friction force is smaller than
   measured force: the vertex is displaced accordingly */
255  vv.x:=vv.oldx[1]+(vv.x-vv.oldx[1])*(force_per_length_up-
   f_up)/force_per_length_up;
256  vv.y:=vv.oldx[2]+(vv.y-vv.oldx[2])*(force_per_length_up-
   f_up)/force_per_length_up;
257  vv.z:=vv.oldx[3]+(vv.z-vv.oldx[3])*(force_per_length_up-
   f_up)/force_per_length_up;
258  angle_of_up:=final_angle_up;
259  };
260  vv.angle:=angle_of_up;
261  };
```

```
262  };
263  foreach vertex vv do if on_constraint 1 then
264  {
   /*only consider vertices on the contact line (constraint 2,
   bottom surface)*/
   // Test if vertex is in an advancing or receding situation
265  product_b:=((vv.__velocity[1])*vv.vertexnormal[1]+(vv.__vel
   ocity[2])*vv.vertexnormal[2]+(vv.__velocity[3])*vv.vertexnorma
   l[3]);
266  if (product_b<0) then {
267  f_b:=f_max_rec_b; //we are in a receding situation
268  final_angle_b:=rec_b;
269  product_b:=-
   sqrt((vv.__velocity[1])^2+(vv.__velocity[2])^2+(vv.__velocity[
   3])^2);
270  } else {
271  f_b:=f_max_adv_b; //we are in an advancing situation
272  final_angle_b:=adv_b;
273  product_b:=sqrt((vv.__velocity[1])^2+(vv.__velocity[2])^2+(
   vv.__velocity[3])^2);
274  };
275  displacement_b:=abs(product_b);  //vertex virtual
   displacement
276  length0_b:=0;
```

```
277  foreach vv.edge ee do if on_constraint 1 then {
278  length0_b:=length0_b+ee.length;   // dl (differential
  contact line length)
279  };
280  force_per_length_b:=2*displacement_b/length0_b;  /*measure
  force per unit length from vertex virtual displacement*/
281  if (force_per_length_b<f_b) then { /*maximum friction force
  is larger than measured force: the vertex remains fixed*/
282  vv.x:=vv.oldx[1];
283  vv.y:=vv.oldx[2];
284  vv.z:=vv.oldx[3];
285  angle_of_b:=acos(-
  2*product_b/length0_b+cos(y_angle_b*pi/180))*180/pi; /*new
  contact angle value is calculated */
286  } else {   /* maximum friction force is smaller than
  measured force: the vertex is displaced accordingly */
287  vv.x:=vv.oldx[1]+(vv.x-vv.oldx[1])*(force_per_length_b-
  f_b)/force_per_length_b;
288  vv.y:=vv.oldx[2]+(vv.y-vv.oldx[2])*(force_per_length_b-
  f_b)/force_per_length_b;
289  vv.z:=vv.oldx[3]+(vv.z-vv.oldx[3])*(force_per_length_b-
  f_b)/force_per_length_b;
290  angle_of_b:=final_angle_b;
291  };
```

```
292  vv.angle:=angle_of_b;
293  };
294  };
/* “cav” function do the default vertex averaging (V) Evolver
function by considering CAH. If the normal “V” function was
used, then the contact lines would move during vertex averaging.
*/
  cav:=
295  {
296  //store old positions of contact points (vertices)
297  set vertex oldx[1] x;
298  set vertex oldx[2] y;
299  set vertex oldx[3] z;
  /* calculating max and min advancing and receding friction
  forces */

300  f_max_adv_up:=(cos(y_angle_up*pi/180)-cos(adv_up*pi/180));
301  f_max_rec_up:=-(cos(y_angle_up*pi/180)-cos(rec_up*pi/180));
302  delta_f_up:=-(cos(adv_up*pi/180)-cos(rec_up*pi/180));
303  f_max_adv_b:=(cos(y_angle_b*pi/180)-cos(adv_b*pi/180));
304  f_max_rec_b:=-(cos(y_angle_b*pi/180)-cos(rec_b*pi/180));
305  delta_f_b:=-(cos(adv_b*pi/180)-cos(rec_b*pi/180));
306  V; //virtual vertex averaging
```

```
307  if scale>0 then {
308  foreach vertex vv do if on_constraint 2 then
309  {
   /*only consider vertices on the contact line (constraint 1,
   top surface) */
   // Test if the vertex is in an advancing or receding situation
310  product_up:=((vv.__velocity[1])*vv.vertexnormal[1]+(vv.__ve
   locity[2])*vv.vertexnormal[2]+(vv.__velocity[3])*vv.vertexnorm
   al[3]);
311  if (product_up<0) then {
312  f_up:=f_max_rec_up; //we are in a receding situation
313  final_angle_up:=rec_up;
314  product_up:=sqrt((vv.__velocity[1])^2+(vv.__velocity[2])^2+
   (vv.__velocity[3])^2);
315  } else {
316  f_up:=f_max_adv_up; //we are in an advancing situation
317  final_angle_up:=adv_up;
318  product_up:=sqrt((vv.__velocity[1])^2+(vv.__velocity[2])^2+
   (vv.__velocity[3])^2);
319  };
320  displacement_up:=abs(product_up);  //vertex virtual
   displacement
321  length0_up:=0;
322  foreach vv.edge ee do if on_constraint 2 then {
```

```
length0_up:=length0_up+ee.length;   // dl (i.e.
  differential contact line length)
};
force_per_length_up:=2*displacement_up/length0_up;
  /*measure force per unit length from vertex virtual
  displacement*/
if (force_per_length_up<f_up) then { /*maximum friction
  force is larger than measured force: the vertex remains
  fixed*/
vv.x:=vv.oldx[1];
vv.y:=vv.oldx[2];
vv.z:=vv.oldx[3];
angle_of_up:=acos(-
  2*product_up/length0_up+cos(y_angle_up*pi/180))*180/pi; /*new
  contact angle value is assigned to the vertex*/
} else {   /*maximum friction force is smaller than
  measured force: the vertex is displaced accordingly */
vv.x:=vv.oldx[1]+(vv.x-vv.oldx[1])*(force_per_length_up-
  f_up)/force_per_length_up;
vv.y:=vv.oldx[2]+(vv.y-vv.oldx[2])*(force_per_length_up-
  f_up)/force_per_length_up;
vv.z:=vv.oldx[3]+(vv.z-vv.oldx[3])*(force_per_length_up-
  f_up)/force_per_length_up;
angle_of_up:=final_angle_up;
```

```
336  };
337  vv.angle:=angle_of_up;
338  };
339  };
340  foreach vertex vv do if on_constraint 1 then
341  {
  /*only consider vertices on the contact line (constraint 2,
  bottom surface)*/
  // Test if vertex is in an advancing or receding situation
342  product_b:=((vv.__velocity[1])*vv.vertexnormal[1]+(vv.__vel
  ocity[2])*vv.vertexnormal[2]+(vv.__velocity[3])*vv.vertexnorma
  l[3]);
343  if (product_b<0) then {
344  f_b:=f_max_rec_b; //we are in a receding situation
345  final_angle_b:=rec_b;
346  product_b:=-
  sqrt((vv.__velocity[1])^2+(vv.__velocity[2])^2+(vv.__velocity[
  3])^2);
347  } else {
348  f_b:=f_max_adv_b; //we are in an advancing situation
349  final_angle_b:=adv_b;
350  product_b:=sqrt((vv.__velocity[1])^2+(vv.__velocity[2])^2+(
  vv.__velocity[3])^2);
351  };
```

```
352  displacement_b:=abs(product_b);  //vertex virtual
  displacement
353  length0_b:=0;
354  foreach vv.edge ee do if on_constraint 1 then {
355  length0_b:=length0_b+ee.length;   // dl (differential
  contact line length)
356  };
357  force_per_length_b:=2*displacement_b/length0_b;  /*measure
  force per unit length from vertex virtual displacement*/
358  if (force_per_length_b<f_b) then { /*maximum friction force
  is larger than measured force: the vertex remains fixed*/
359  vv.x:=vv.oldx[1];
360  vv.y:=vv.oldx[2];
361  vv.z:=vv.oldx[3];
362  angle_of_b:=acos(-
  2*product_b/length0_b+cos(y_angle_b*pi/180))*180/pi; /*new
  contact angle value is calculated */
363  } else {   /* maximum friction force is smaller than
  measured force: the vertex is displaced accordingly */
364  vv.x:=vv.oldx[1]+(vv.x-vv.oldx[1])*(force_per_length_b-
  f_b)/force_per_length_b;
365  vv.y:=vv.oldx[2]+(vv.y-vv.oldx[2])*(force_per_length_b-
  f_b)/force_per_length_b;
```

```
366  vv.z:=vv.oldx[3]+(vv.z-vv.oldx[3])*(force_per_length_b-
   f_b)/force_per_length_b;
367  angle_of_b:=final_angle_b;
368  };
369  vv.angle:=angle_of_b;
370  };
371  };
   /* alongside with checking the stability of the bridge with
   convergence of the Evolver solution, "stability" function was
   implemented which checks whether the bridge is artificially
   "moving" towards the cusp or not (i.e. definition of an
   unstable bridge), or, it is remaining stable. */

372  stability:= {
373  radiusmaxup1:=0;
374  radiusmaxup2:=0;
375  radiusmaxb1:=0;
376  radiusmaxb2:=0;
377  counter1:=0;
378  counter2:=0;
379  id1:=0;
380  id2:=0;
381  id3:=0;
382  id4:=0;
```

```
383  id5:=0;
384  id6:=0;
385  id7:=0;
386  id8:=0;
387  maxx2:=-10000;
388  maxyy2:=-10000;
389  minxx2:=100000;
390  minyy2:=10000;
391  maxx1:=-10000;
392  maxyy1:=-10000;
393  minxx1:=100000;
394  minyy1:=10000;
395  zo1:=0;
396  zo2:=0;
397  zo3:=0;
398  zo4:=0;
399  zo5:=0;
400  zo6:=0;
401  zo7:=0;
402  zo8:=0;
   /* the leftmost and rightmost contact points of the bridge on
   both surfaces were found below */
403  foreach vertex vv do if on_constraint 2 then
404  {
```

```
405  if (vv.y<minyy2) then {
406  minyy2:=vv.y;
407  id1:=vv.id;
408  zo1:=vv.z;}
409  };
410  foreach vertex vv do if on_constraint 2 then
411  {
412  if (vv.y>maxyy2) then {
413  maxyy2:=vv.y;
414  id3:=vv.id;
415  zo3:=vv.z;}
416  } ;
417  foreach vertex vv do if on_constraint 2 then
418  {
419  if (vv.x<minxx2) then {
420  minxx2:=vv.x;
421  id2:=vv.id;
422  zo2:=vv.z;}
423  } ;
424  foreach vertex vv do if on_constraint 2 then
425  {
426  if (vv.x>maxx2) then {
427  maxx2:=vv.x;
428  id4:=vv.id;
```

```
429  zo4:=vv.z;}
430  } ;
431  foreach vertex vv do if on_constraint 1 then
432  {
433  if (vv.y<minyy1) then {
434  minyy1:=vv.y;
435  id5:=vv.id;
436  zo5:=vv.z;}
437  };
438  foreach vertex vv do if on_constraint 1 then
439  {
440  if (vv.y>maxyy1) then {
441  maxyy1:=vv.y;
442  id7:=vv.id;
443  zo7:=vv.z;}
444  } ;
445  foreach vertex vv do if on_constraint 1 then
446  {
447  if (vv.x<minxx1) then {
448  minxx1:=vv.x;
449  id6:=vv.id;
450  zo6:=vv.z;}
451  } ;
452  foreach vertex vv do if on_constraint 1 then
```

```
453  {
454  if (vv.x>maxx1) then {
455  maxx1:=vv.x;
456  id8:=vv.id;
457  zo8:=vv.z;}
458  } ;
459  cah 100; // evolving the surface using cah
460  if (maxyy2>vertex[id3].y) &&
   (minyy2>vertex[id1].y)&&(maxyy1>vertex[id7].y) &&
   (minyy1>vertex[id5].y)
461  then { print "*********unstable*********\n"} /* if the
   bridge is moving, then “unstable” will be printed */
462  }
   /* curvature generates coordinates of vertices on rightmost
   and leftmost menisci of the bridge. These coordinates can be
   used to calculate the in-plane curvature of the bridge (R) */
463  Curvature:=
464  {
465  id1:=0;
466  id2:=0;
467  id3:=0;
468  id4:=0;
469  id5:=0;
470  id6:=0;
```

```
471  id7:=0;
472  id8:=0;
473  maxx2:=-10000;
474  maxyy2:=-10000;
475  minxx2:=100000;
476  minyy2:=10000;
477  maxx1:=-10000;
478  maxyy1:=-10000;
479  minxx1:=100000;
480  minyy1:=10000;
481  vvzr:=0;
482  vvzl:=0;
483  tempidl:=0;
484  tempidr:=0;
485  nnn1:=0;
486  nnn2:=0;
/* finding the leftmost and rightmost contact points */
487  foreach vertex vv do if on_constraint 2 then
488  {
489  if (vv.y<minyy2) then {
490  minyy2:=vv.y;
491  id1:=vv.id;
492  zo1:=vv.z;}
```

```
493  };
494  foreach vertex vv do if on_constraint 2 then
495  {
496  if (vv.y>maxyy2) then {
497  maxyy2:=vv.y;
498  id3:=vv.id;
499  }
500  } ;
501  foreach vertex vv do if on_constraint 1 then
502  {
503  if (vv.y<minyy1) then {
504  minyy1:=vv.y;
505  id5:=vv.id;
506  }
507  };
508  foreach vertex vv do if on_constraint 1 then
509  {
510  if (vv.y>maxyy1) then {
511  maxyy1:=vv.y;
512  id7:=vv.id;
513  }
514  } ;
515  tempidr:=id7;
516  tempidl:=id5;
```

```
/* finding the vertices on the rightmost and leftmost menisci.
Here, we use the length of the vertices edge as a measure of the
distance between the vertices to make sure that we are only
choosing vertices that are on the rightmost and leftmost
menisci. */

517  foreach vertex vv do if ((abs(vv.x-
   vertex[id7].x)<=(vv.edge[1].length/2)) &&
   (vv.y>((vertex[id5].y+vertex[id7].y)/2)))then {
518  printf "%f  %f
   %f\n",vv.z,vv.y,body[1].pressure>>"curvbigside.xls";
519  vvzr:=vv.z;
520  tempidr:=vv.id;
521  };
522  foreach vertex vv do if ((abs(vv.x-
   vertex[id5].x)<=abs(vv.edge[1].length/2)) &&
   (vv.y<((vertex[id5].y+vertex[id7].y)/2)))then {
523  printf "%f  %f\n",vv.y,vv.z>>"curvsmallside.xls";
524  vvzl:=vv.z;
525  tempidl:=vv.id;
526  };
527  }

/* “adhy” calculates both normal and lateral adhesion forces */

adhy:={
```

```
528  numvex1:=0;
529  numvex2:=0;
530  lengthadh_b:=0;
531  lengthadh_up:=0;
532  lengthofeach_b:=0;
533  alp_b:=0;
534  alp_up:=0;
535  tot_adhy_b:=0;
536  tot_adhy_up:=0;
537  tot_adhz_b:=0;
538  tot_adhz_up:=0;
539  tot_yp_b:=0;
540  tot_yp_b:=0;
541  foreach vertex vv do if on_constraint 1 then {
542  foreach vv.edge ee do if on_constraint 1 then {
543  lengthadh_b:=lengthadh_b+ee.length;   /* dl (differential
   contact line length) */
544  };
545  lengthadh_b:=lengthadh_b/2; /* since each vertex has two
   edges shared with two other vertices, dl is divided by two. */
   /* calculating the normal and lateral adhesion force of each
   vertex on the bottom surface */
```

```
546  alp_b:=asin(abs(vv.vertexnormal[3])/(sqrt((vv.vertexnormal[
   1])^2+(vv.vertexnormal[2])^2+(vv.vertexnormal[3])^2))); \*
   equivalent to α angle in the paper. */
547  vv.yadh_b:=(vv.vertexnormal[2]/cos(alp_b))*(lengthadh_b)*(c
   os(vv.angle*pi/180))*cos(s_angle*pi/360); //lateral adhesion
   force of each vertex
548  vv.zadh_b:=sin(s_angle*pi/360)*sin(vv.angle*pi/180)*(length
   adh_b); //normal adhesion force of each vertex
549  lengthadh_b:=0;
550  printf "%f     %f     %f
   %f\n",vv.x,vv.y,vv.yadh_b*72.8,vv.angle>>"yadh_b.xls";
   /*extracting adhesion force components in lateral and normal
   directions of each contact point on the bottom surface in an
   excel file. */
551  };
   /*integrating adhesion force components on each surface to
   find the total adhesion force value in normal and lateral
   directions*/
552  foreach vertex vv do if on_constraint 1 then {
553  tot_adhy_b:=tot_adhy_b+vv.yadh_b; /*calculating the total
   lateral adhesion force (for water) on the bottom surface*/

554  tot_adhz_b:=tot_adhz_b+vv.zadh_b; /*calculating the total
   normal adhesion force (for water) on the bottom surface*/
```

```
555  };
/* similarly, the normal and lateral adhesion forces were
calculated on the top surface (see below) */
556  foreach vertex vv do if on_constraint 2 then {
557  foreach vv.edge ee do if on_constraint 2 then {
558  lengthadh_up:=lengthadh_up+ee.length;   /* dl (differential
  contact line length)*/
559  };
560  lengthadh_up:=lengthadh_up/2;
561  alp_up:=asin(abs(-
  tan(s_angle*pi/180)*vv.vertexnormal[2]+vv.vertexnormal[3]))/(s
  qrt(((tan(s_angle*pi/180))^2+1)*sqrt((vv.vertexnormal[1])^2+(v
  v.vertexnormal[2])^2+(vv.vertexnormal[3])^2)));
562  vv.yadh_up:=(vv.vertexnormal[2]/cos(alp_up))*(lengthadh_up)
  *(cos(vv.angle*pi/180))*cos(s_angle*pi/360);
563  vv.zadh_up:=sin(s_angle*pi/360)*sin(vv.angle*pi/180)*(lengt
  hadh_up);
564  lengthadh_up:=0;
565  //  printf "%f     %f     %f
  %f\n",vv.x,vv.y,vv.yadh_up*72.8,vv.angle>>"yadh_up.xls";
566  };
567  foreach vertex vv do if on_constraint 2 then {
568  tot_adhy_up:=tot_adhy_up+vv.yadh_up;
```

```
569  tot_adhz_up:=tot_adhz_up+vv.zadh_up;
570  };
571  print 72.8*(tot_adhy_up+tot_adhy_b); /*printing the total
   normal adhesion force on both surfaces (for water). */
572  print -72.8*(tot_adhz_up+tot_adhz_b); /*printing the total
   lateral adhesion force on both surfaces (for water). */
573
574  printf "%f       %f         %f
   %f\n",height,72.8*(tot_adhy_up+tot_adhy_b),(-
   72.8)*(tot_adhz_up+tot_adhz_b),-
   (72.8*(tot_adhy_up+tot_adhy_b))-((-
   72.8)*(tot_adhz_up+tot_adhz_b))>>"adhesion.xls"; /*extracting
   the adhesion force values to an excel file */
575  };
576  plotever:={ /*extract adhesion forces and contact angles
   values to excel files */
577  plotup;
578  adhy;}
```

*/ note that the total pressure force was found using “Interface Area” and “pressure” functions of SE-FIT software. Then, using Eqn. (2.3), we double checked the value of the total pressure force based on the lateral and normal adhesion forces i.e. F_P=-F_n-F_l. Hence, F_P was found in two independent ways. This made us confident that the code is working correctly. */

C.2: Surface Evolver code for Chapter Three

For Chapter Three, an SE code similar to the one given in section C.1 was used. In addition to the code given in section C.1, several parameters and functions were added to SE to simulate the compressing and stretching of the bridge. These additions are given below:

Line numbering continues from the code in section C.1:

```
579  parameter incrim = 0.01e-3 // increments of changing height
580  parameter criteria=0.00001e-6 /*criterion for convergence
  in each evolving step */
581  parameter deltah = 0.2e-3 // equivalent to Δh
582  parameter cycle:=5 // number of cycles
583  heightup:={height:=height+incrim}  /*increasing height of
  the top surface*/
584  heightdown:={height:=height-incrim} /*decreasing height of
  the top surface*/
  /* "heightup" and "heightdown" functions increase/decrease the
  height of the top surface in a direction normal to the top
  surface. However, in the experiments, the height was
  increased/decreased in a direction normal to the bottom
  surface. Therefore, after applying "heightup" or "heightdown"
  functions, the position of the top surface was corrected to
  have a change in the height normal to the bottom surface using
  "fixitup" or "fixitdown" functions, respectively. */

585  fixitdown:=
586  {
587  foreach vertex vv do if on_constraint 2 then
588  {
589  vv.y:=vv.y-incrim*cos(s_angle*pi/180)*sin(s_angle*pi/180);
590  vv.z:=vv.z-incrim*(sin(s_angle*pi/180))^2;
```

```
591  };
592  }
593  fixitup:=
594  {
595  foreach vertex vv do if on_constraint 2 then
596  {
597  vv.y:=vv.y+incrim*cos(s_angle*pi/180)*sin(s_angle*pi/180);
598  vv.z:=vv.z+incrim*(sin(s_angle*pi/180))^2;
599  };
600  }
601  moveitup:= {heightup;fixitup} /* This function applies
  heightup and fixitup functions after each other*/
602  moveitdown:= {heightdown;fixitdown} /* This function
  applies “heightdown” and “fixitdown” functions after each
  other*/
603  gogoup:={ /* this function do all the works for stretching
  the bridge: it increases the height of the top surface,
  evolves the surface, checks the convergence, evolves the
  surface again if needed, and it stores the data (contact
  angle, contact widths, etc.) after convergence.  */
604  energyaval:=total_energy;   /*initial energy of the
  bridge*/
605  moveitup; /*stretching the bridge*/
606  cav 3;
607  cah 200; //evolving the surface
608  recalc; //recalculating the energy to check convergence
609  while (abs(total_energy-energyaval)>criteria) do
  {energyaval:=total_energy; cah 100; recalc;}; /* checking
  convergence based on the criterion*/
610  plotever; //plotting data }
611  gogodown:={ /*similar to “gogoup” this time for compressing
  the bridge*/
```

```
612  energyaval:=total_energy;
613  moveitdown;
614  cav 3;
615  cah 200;
616  recalc;
617  while (abs(total_energy-energyaval)>criteria) do
  {energyaval:=total_energy; cah 100; recalc;};
618  plotever; }
  /* to reduce the computing time, "refinedge" was implemented.
  This function only refines the facets close to the vertices on
  the top and bottom surfaces (around the triple lines). Such
  refinement reduced the required time to finish a simulation at
  least by half, without affecting the output. */
619  refinedge:= {
620  foreach facet ff do {
621  {       if ((ff.vertex[1] on_constraint 1) || (ff.vertex[2]
  on_constraint 1) || (ff.vertex[3] on_constraint 1)) then
  refine ff; ;
622  }
623  };
624  foreach facet ff do {
625  {       if ((ff.vertex[1] on_constraint 2) || (ff.vertex[2]
  on_constraint 2) || (ff.vertex[3] on_constraint 2)) then
  refine ff; ;
626  }
627  }
628  }
629  initial2r:={ /*initial configuration of the bridge with two
  regular refinements and two refinements near the triple lines
  */
```

```
630  r; cah 10; cav 10; cah 100 ; cav 10; cah 500; r; cav 100;
  cah 1500; refinedge 2; cav 10; cah 200; u; cav 10; cah 1000;
  plotever;}
631  initial3r:={ /*initial configuration of the bridge with
  three regular refinements and two refinements near the triple
  lines */
632  r; cah 10; cav 10; cah 100; r ; cav 10; cah 500; r; cav
  100; cah 1500;refinedge 2; cav 10; cah 200;u; cav 10; cah
  1000; plotever;}
633  DoaTestDeltah:=
634  {
635  for ( inx:=0 ; inx<cycle ; inx++) /* compressing and
  stretching the bridge for Δh. Compressing and stretching is
  repeated for the number of cycles given*/
636  {
637  gogodown    deltah/incrim; gogoup    deltah/incrim;};
638  }
```

D: More Details on the Experimental Process

D.1: Details on the Leveling Platform and Tilting the Top Surface

An image of the leveling platform and the tilting stage (disassembled from the setup) is given in Figure D.1. The tilting stage was able to tilt the top surface with $0.2°$ increments (up to $22°$) and the leveling platform ensured that the top surface is completely level when $\psi = 0°$, hence it would only be tilted in one direction when $\psi > 0$. The leveling platform uses two adjustment screws to eliminate any unevenness of the tilting stage (see Figure D.1).

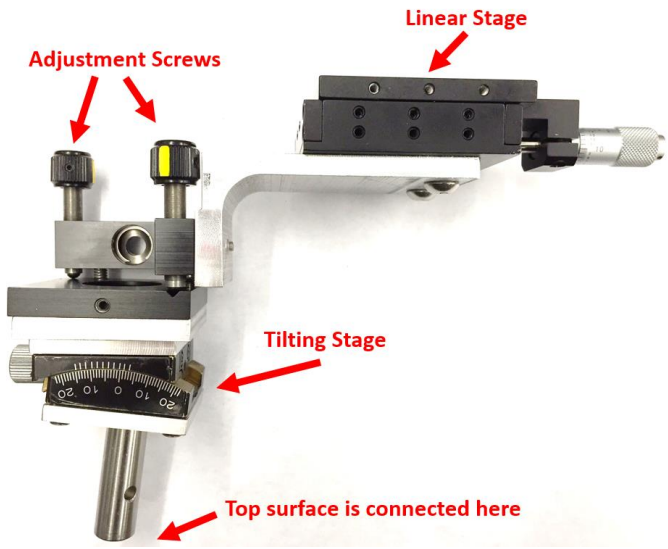

Figure D.1 An image of leveling platform (disassembled from the setup) and the tilting stage which allowed tilting the top surface only in one direction.

In Figure D.2, the leveling platform and the tilting stage connected to the actuator is shown. A circular bubble level was used to indicate whether the tilting stage is level or not; the two adjustment screws were used until the bubble rested in the center.

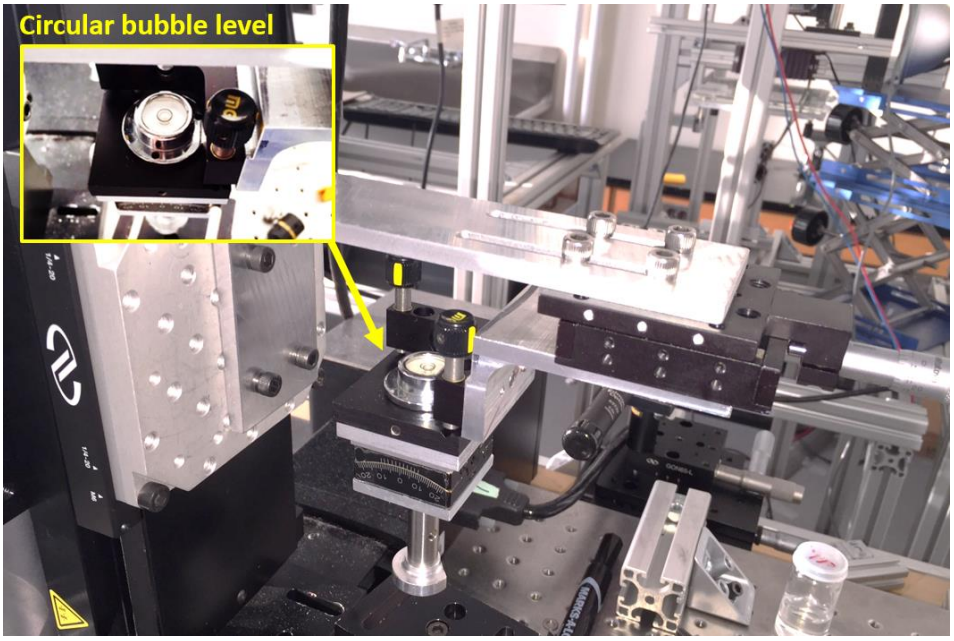

Figure D.2 Circular bubble level was used to ensure the levelness of the tilting stage.

D.2: Details on attaching the top surface to the stage

To attach the top surface to the top stage, a thin double-sided tape was used (see Figure D.3). Tape was placed evenly on the back of the surface as to not disrupt the balance.

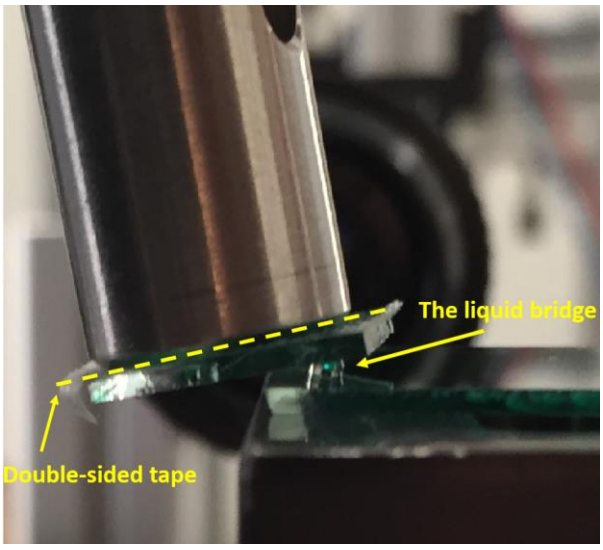

Figure D.3 Thin double-sided tape was used to connect to top surface to the tilting stage.

D.3: Details on Aligning the Cameras

Due to the nontrivial shape of the bridge, it was necessary to ensure that the side view camera was exactly facing the ψ angle, and the front view camera was perpendicular to the ψ angle. Only then we could be ensured of the angle of view of the image when comparing the shape and the contact angles of bridge obtained from the experiments with the corresponding views of the simulations.

The camera alignment was done as follows: A circular ring was placed on the bottom surface stage in front of the camera. The ring was aligned with the stage such that it was orthogonal to the desired camera's optical path (see Figure D.4). Therefore, if the circular ring was elliptical shaped in the eye of the camera (i.e. $d_1 \neq d_2$ in Figure D.4), it meant that the camera was not aligned properly. If the ring was seen as a circle by the camera (i.e. $d_1 = d_2$ in Figure D.4), it implied that the camera was aligned correctly. The same procedure was used for both cameras.

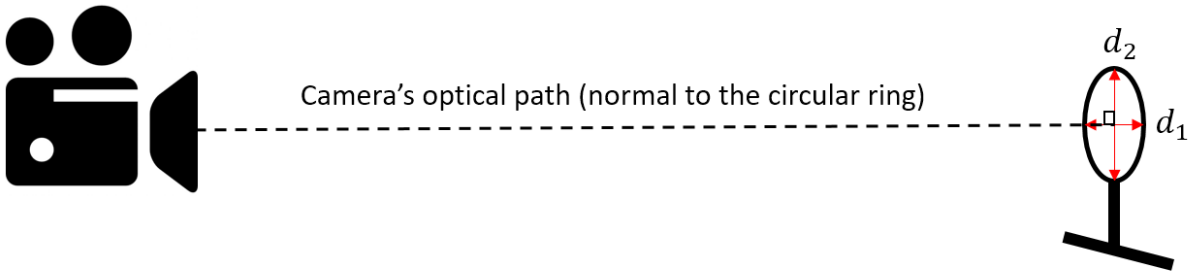

Figure D.4 Schematics of the procedure used to align the cameras.

D.4: Measurements

All the measurements (e.g. contact angles, contact widths, contact point position, etc.) were done manually using ImageJ software. The cameras were calibrated using pixel-to-millimeter grid. The resolution of the measurements (i.e. the size of one pixel) was approximately $0.005mm$.